Noncollinear Magnetism in Mn_2RhSn Heusler Compound

Dissertation

zur Erlangung des Grades

"Doktor der Naturwissenschaften"

am Fachbereich Physik

der Johannes Gutenberg-Universität Mainz

vorgelegt von

Olga Meshcheriakova

geboren in Lviv, Ukraine

Mainz, 2014

Dekan: Univ.-Prof. Dr. Reinhard Höpfner

1. Berichterstatter:
2. Berichterstatter:

Tag der mündlichen Prüfung:

Die vorliegende Arbeit wurde in der Zeit von November 2010 bis Mai 2014 am Institut für Physik, Institut für Anorganische und Analytische Chemie im Fachbereich Chemie, Pharmazie und Geowissenschaften der Johannes Gutenberg-Universität, Mainz sowie am Max-Planck-Institut für Chemische Physik fester Stoffe, Dresdsen unter der Leitung von Frau Prof. Dr. Claudia Felser angefertigt.

Mainz, September 2014

Hiermit versichere ich, dass ich die vorliegende Dissertation selbstständig verfasst und keine anderen als die angegebenen Hilfsmittel benutzt habe. Alle der Literatur entnommenen Stellen sind als solche gekennzeichnet.

Mainz, September 2014

Стасу и Веро

Zusammenfassung

Heusler Verbindungen bezeichnen eine der vielfälltigsten Stoffklassen in der Festkörperchemie. In ihnen befinden sich Systeme mit verschiedenen grundlegenden sowie exotischen physikalischen Eigenschaften. Die Besonderheit der Heusler Verbindungen besteht jedoch in der Anpassungsfähigkeit dieser Eigenschaften. Somit bieten sie Lösungen auf explizite Probleme in den Ingenieurswissenschaften. Diese Arbeit befasst sich mit dem nicht-kollinearen Magnetismus in den nicht-zentrosymmetrischen ferrimagnetischen manganreichen Heusler Verbindungen. Basierend auf den erhaltenen experimentellen Daten und theoretischen Berechnungen stellen wir das System Mn_2YZ als vielversprechenden Kandidaten für die Bildung eines Skyrmionen-Gitters vor. Die Arbeit konzentriert sich auf polikristalline $\mathrm{Mn_2RhSn}$ Proben, welche als Prototyp dienen. Sie kristallisieren in einer tetragonalen nicht-zentrosymmetrischen Struktur (No. 119, $I\bar{4}m2$), welches den anisotropischen Dzyaloshinskii-Moriya Austausch ermöglicht. Zusätzliche kurz-reichwertige Modulationen, verursacht durch den konkurrierende Heisenberg Austausch zwischen nächsten und übernächsten Schichten, werden bei Temperaturen über 80 K unterdrückt. Dies erlaubt die Ausbildung von langreichweitigen Modulationen in der idealen ferrimagnetischen Struktur innerhalb der kristallographischen ab-Fläche und bevorzugt somit die Bildungen eines Skyrmionen-Gitters in einen Termperaturbereich von $(80 \leq T \leq 270)$ K. Die Untersuchungen an $\mathrm{Mn_2RhSn}$ wurden auf ein breites Spektrum an Zusammensetzungen erweitert und diese zusätzlich als Dünnfilme hergestellt.

Abstract

Heusler compounds is a large class of materials, which exhibits diverse fundamental phenomena, together with the possibility of their specific tailoring for various engineering demands. Present work discusses the magnetic noncollinearity in the family of noncentrosymmetric ferrimagnetic Mn_2-based Heusler compounds. Based on the obtained experimental and theoretical results, Mn_2YZ Heusler family is suspected to provide promising candidates for the formation of the skyrmion lattice. The work is focused on Mn_2RhSn bulk polycrystalline sample, which serves as a prototype. It crystallizes in the tetragonal noncentrosymmetric structure (No. 119, $I\bar{4}m2$), which enables the anisotropic Dzyaloshinskii-Moriya (DM) exchange coupling. Additional short-range modulation, induced by the competing nearest and next-nearest inter-planes Heisenberg exchange, is suppressed above the 80 K. This allows to develop the long-range modulations in the ideal ferrimagnetic structure within the ab crystallographic planes, and thus, favors to the occurrence of the skyrmion lattice within the temperature range of $(80 \leq T \leq 270)$ K. The studies of Mn_2RhSn were expanded to the broad composition range and continued on thin film samples.

List of publications

1. O. Meshcheriakova, A. Köhler, S. Ouardi, Y. Kondo, T. Kubota, S. Chandra, J. Karel, C.V. Barbosa, R. Stinshoff, R. Sahoo, S. Ueda, E. Ikenaga, S. Mizukami, S. Chadov, D. Ebke, G.H. Fecher and C. Felser. **Structural, electronic, and magnetic properties of perpendicularly magnetised Mn_2RhSn thin films**. Submitted to J. Phys. D: Appl. Phys. (2014).
2. O. Meshcheriakova, S. Chadov, A.K. Nayak, U.K. Rößler, J. Kübler, G. André, A.A. Tsirlin, J. Kiss, S. Hausdorf, A. Kalache, W. Schnelle, M. Nicklas and C. Felser. **Large noncollinearity and spin-reorientation in the novel Mn_2RhSn Heusler magnet**. Phys. Rev. Lett. **113**, 087203 (2014).
3. V. Alijani, O. Meshcheriakova, J. Winterlik, G. Kreiner, G.H. Fecher and C. Felser. **Increasing Curie temperature in tetragonal Mn_2RhSn Heusler compound through substitution of Rh by Co and Mn by Rh**. J. Appl. Phys. **113**, 063904 (2013).
4. J. Winterlik, G.H. Fecher, B. Balke, T. Graf, V. Alijani, V. Ksenofontov, C.A. Jenkins, O. Meshcheriakova, C. Felser, G. Liu, S. Ueda, K. Kobayashi, T. Nakamura, and M. Wójcik. **Electronic, magnetic, and structural properties of the ferrimagnet Mn_2CoSn**. Phys. Rev. B. **83**, 174448 (2011).

Contents

Preface

Non-collinearity has always been one of the most non-trivial aspects in magnetism both from the fundamental and technological prospectives. Many metallic compounds, oxides or single elements exhibit a non-collinear ground state like helical, conical or spin spirals. At certain conditions, non-collinearity may occur in systems, which are initially ferro- (ferri-) or antiferromagnetic, e.g., in the form of a domain wall. Some materials show a variety of commensurate-incommensurate magnetic transitions when under the influence of external magnetic field or temperature.

Having a complex hierarchy of various long- and short-range interactions, magnetic solid provides the richest playground for all possible spin arrangements. In the simplified view, the strong Heisenberg exchange between the nearest atoms leads to the parallel (when positive) or antiparallel (if negative) spin configuration. A superimpose of two or more antiferromagnetic interactions results in a geometric spin frustration. The competing exchanges are often observed in various disordered magnetic systems like spin-glasses or substitutional alloys. In addition, a strong homogeneous linear coupling can be perturbed by anisotropic Dzyaloshinskii-Moriya (DM) interaction establishing a long-range modulated magnetic structure. On a short scale, the spin direction can be also defined by a magnetic anisotropy or a dipolar interaction.

In this sense, Manganese-based compounds are especially attractive as they often form complex non-collinear orderings like helices, cones, antiferromagnetic triangles, spin spirals or skyrmions. Depending on temperature, the elementary manganese exists in four allotropic modifications: α-, β-, γ- and δ-Mn. Due to the competing attempts to simultaneously maximize the magnetic moment and to shorten the interatomic distances, the α-Mn is known to exhibit a non-collinear antiferromagnetic phase below 95 K; this antiferromagnetic frustration becomes even stronger in the β-Mn.

Various types of magnetic structure can be comprehensively analyzed by the neutron scattering. For example, helimagnetism has been first suggested to interpret the neutron diffraction data of MnO_2 in 1959 and then has been also reported in many rare-earth (RE) metals and RE-based compounds (a helifan in Ho, a cycloid in Er, a tilted helix in Ho-Tm or Ho-Er alloys and multiple modulations in Nd). Helical magnetic order is a ground state of some materials showing a skyrmion phase (MnSi, FeCoSi, FeGe). A magnetic cone can appear due to the competition of the commensurate collinear and the incommensurate cycloidal order (Mn-$CoWO_4$), electric polarization in multiferroic magnets ($Ba_2Mg_2Fe_{12}O_{22}$), etc. Triangular antiferromagnetism typically appears due to the magnetic frustration in a stacked triangle lattice (Mn_3Rh or Mn_3Pt). Some are not fully compensated showing a weak ferromagnetism, e. g. due to the magnetocrystalline anisotropy in the Mn_3Sn case. Often, triangular antiferromagnets show multiple transitions through tetracritical points on the phase diagrams. The skyrmion state can be induced in the systems having no inversion symmetry and a certain ratio of the DM and Heisenberg exchange by the variation of external field and temperature.

In addition to the bulk phenomena, inhomogeneous magnetic interactions become even stronger in layered systems due to the broken interface symmetry. Whereas bulk helimagnets require a special temperature-field regime to stabilize the skyrmion phase, interfaces can form it as a ground state. Recently, skyrmions have attracted a large scientific and technological interest as of their potential for the future data storage devices. Using a spin-polarized current, they can be created or destroyed; also they can be moved at significantly low current densities than the domain walls.

Heusler compounds are a big class of materials with a broad scope of possibilities. They exhibit a large variety of fundamental physical phenomena as well as can be flexibly tailored for a specific industrial application. Counting more than 1500 members, Heusler compounds offer a tunability in the lattice parameter, magnetic moment, Curie temperature, tetragonal distortion, spin polarization and a spin-orbit coupling. All these characteristics are vitally important for spintronic applications. Recently emerged Mn_2-based Heusler family is especially attractive due to the presence of two ferrimagnetically aligned Mn sublattices, which result in a small net magnetization and an additional possibility of a separate sublattice manipulation, which can be implemented in an all-optical switching. Despite of the rich physical phenomena, there are only very few examples of non-collinear magnetism in Heusler compounds.

Within the scope of this thesis, the non-trivial magnetic properties of the novel Mn_2-based Heusler compounds are discussed. The materials, studied herein, crystallize in the structure with no inversion symmetry, which allows for the DM interactions. Since this inhomogeneous couplings are responsible for the establishment of non-collinearity, they should be boosted by the spin-orbit coupling (SOC). Thus, heavy metals Rh and Sn are used as Y and Z elements.

First, bulk samples of Mn_2RhSn were successfully obtained: the synthesis procedure was thoroughly optimized in order to have a high-quality homogeneous single-phase material. Structural parameters of a tetragonal cell were refined from the X-ray powder scattering at the room temperature and then were analyzed on a broad scale. While increasing the temperature up to 600° C, a linear decrease of the c/a ratio is observed, which finally results in a more symmetric cubic structure. Contrary, at the low temperatures $T <$RT, the c-parameter evolves rather non-linearly, which is assigned to a complex magnetic behavior of the material. Temperature-dependent magnetization as well as the ground state magnetic structure were comprehensively analyzed based on various measurement techniques, *ab-initio* calculations and micromagnetic simulations. Depending on the field and temperature, a spin-reorientation transition was observed, which is realized by the gradual change of the canting angle between two magnetic sublattices. Having non-centrosymmetric crystal structure, intensified relativistic effects due to the heavy transition metal element, and an easy-to-control magnetization reorientation, the samples appeared attractive for the skyrmion research, therefore growth of thin films became an essential task. A decent part of this work is dedicated to the optimization of the Mn_2RhSn thin film fabrication.

Showing an epitaxial growth, thin films allowed for experimental assessments within a unit cell limit, which is practically impossible in the bulk policrystalline samples. Spin-reorientation transition was well-observed using the ferromagnetic resonance technique; since the measurement implies microwave irradiation, needs a predefined sample's shape and is sensitive to the easy/hard magnetization direction, thin film samples perfectly match. Additionally, thin films finally made the magnetotransport measurement possible: contrary to the bulk samples, voids and cracks there are improbable. It is also known from the literature, that if present, skyrmion phase exists in thinner samples within a broader field-temperature window.

Thin films opened new measurement possibilities to study the Mn_2RhSn Heusler compound. Also, some material's parameters were improved, e. g. Curie temperature T_C was increased from 270 K to 300 K. However, for the industrial applications, the T_C has to be further optimized. Since Cobalt-based compounds exhibit the highest T_Cs and the properties of Heusler compounds can be explained by the number of valence electrons, it has been decided to try a gradual substitution of Rh by Co as these elements belong to the same period of the Mendeleev's table. Indeed, the T_C (as well as magnetic moment m) linearly depends on the Co content in the bulk $Mn_2Rh_{1-x}Co_xSn$ series, which was successfully synthesized with the step of $x = 0.1$.

Alternatively to the application of external heat, a tetragonal-to-cubic structural transition is induced by the chemical substitution: a cubic structure was observed at the 60 at.% of the Co concentration.

Most of the Heusler systems are cubic. In order to make use of the magnetocrystalline anisotropy, needed for industrial applications, one has to look for the tetragonally distorted Heusler systems, which are rather rare. Quite often their search is based on the first-principle calculations, that can indicate electronic instability in the way of a strong peak of DOS at the Fermi energy ϵ_F. The main magnetic interactions in Mn_2RhSn are realized between Mn atoms, while Rh and Sn do not exhibit magnetism. The presence of Co changes the picture of magnetic interactions as an additional moment is now introduced. Thus, for the skyrmion research, pure compounds with only two Mn sublattices are preferred, which stimulates the discussion of phase stability and micromagnetic analysis.

Heusler compounds are rather sensitive to the chemical and structural ordering. Possible disorder scenarios as well as the phase stability are separately investigated by synthesizing slightly off-stoichiometric samples $Mn_{2\pm\delta}Rh_{1\pm\delta}Sn$. It is demonstrated, that the phase is very sensitive to the 2:1:1 composition - a minor excess of Rh (about 15 at.%) kills the tetragonal distortion and leads to the cubic structure, while its deficiency (about 10 at.%) results in a decomposition into tetragonal Mn_2RhSn and hexagonal $Mn_{3-x}Rh_xSn$ phases.

At present, the amount of compounds showing a skyrmion state is rather limited, therefore, an expansion of the materials base is inevitable. Having more than 1500 members and a flexible tuning of physical parameters, Heusler compounds are perfect candidates to realize almost any engineering task and thus are reviewed with an outlook for the industrial applications.

The results of this work open a new prospective for the Heusler compounds in the fundamental and technological aspects. The ground-state magnetic canting is not only observed but also explained from the first principles. The temperature-field driven spin-reorientation transition allows for the easy manipulation of the magnetization direction. Based on the micromagnetic simulations, a skyrmion state is predicted for the Mn_2RhSn, which provides one more dimension for the application of Heusler compounds.

1 Introduction

This chapter gives a theoretical background of the phenomena, which are discussed within the present thesis. First, the main types of magnetic interactions are introduced in order to write a Hamiltonian. Then, an establishment of magnetic modulations is described, which is a result of competing interactions - either classical Heisenberg exchanges J or perturbations caused by the DM coupling. The mechanism of magnetic phase transitions with respect to magnetization as an order parameter is represented by the Ginzburg-Landau functional. In particular, magnetic modulations and phase transitions are considered for the non-centrosymmetric crystal structures with two antiparallel magnetic sublattices. Since the materials driven into the skyrmion state have a great potential for the new generation memory technology, the preconditions for such phase are given.

1.1 Interactions in a bulk magnetic solid

Magnetism in 3d transition metals is a question of whether electrons carrying magnetic moment are localized or shared between different atoms in a solid. The model of localized electrons maps them in a real space, while the opposite approach of itinerant electrons allocates them in a reciprocal space. To get an adequate picture, one combines both extreme approaches [1].

The simplest magnetic structure can be described as a collinear (parallel) arrangement of spins. At the absence of external magnetic field, a ferromagnet possesses a spontaneous magnetization as the local moments are directed along one preferred direction. An antiferromagnetism establishes in case of two mutually compensating antiparallel sublattices. Partially similar, ferrimagnetism appears when the antiparallel sublattices occupy crystallographically different sites resulting in different magnetization values of each sublattice.

A certain type of structure establishes due to the fact, that separate magnetic moments arrange according to the internally and externally acting forces. The strongest internal interaction, the so-called classical Heisenberg exchange [2, 3] is a homogeneous coupling of two localized spins $\mathbf{m}_i$ and $\mathbf{m}_j$ (1.1). The strength and type of the Heisenberg exchange is defined by exchange constant J: $J > 0$ results in a parallel (ferromagnetic) spin alignment, $J < 0$ means an antiparallel (antiferro-, ferrimagnetic) spin alignment. This type of interaction also contains the superexchange or Ruderman-Kittel-Kasuya-Yosida (RKKY) interaction [4, 5, 6, 7, 8, 9], crystal field splitting [10] and domain dynamics [11, 12].

$$E_{\mathrm{ex}} = -\frac{1}{2}\sum_{ij} J_{ij}\mathbf{m}_i\mathbf{m}_j \tag{1.1}$$

The interaction between two different spins also includes a dipolar coupling (1.2) since the interacting moments experience the fields of each other. Contrary to the short-range classical exchange, the dipolar coupling establishes a long-range order and is responsible for the magnetic domains formation. The strength of a generated dipolar coupling varies significantly with the inter-dipolar distance r_{ij}^3.

$$E_{\mathrm{di}} = \sum_{ij}\frac{1}{r_{ij}^3}\left[\mathbf{m}_i\mathbf{m}_j - \left(\mathbf{m}_i\mathbf{e}_i\right)\left(\mathbf{m}_j\mathbf{e}_j\right)\right] \tag{1.2}$$

Here $\mathbf{e}_{ij}$ is a unit vector along a line joining two centers of the dipoles.

Some antiferromagnetic systems can also exhibit spontaneous magnetization. This effect does not relate to any ferromagnetic impurities, but to a crystal symmetry. Systems, which are noncentrosymmetric, exhibit a small magnetic component, a so-called staggered magnetization, which is slightly deviated from the principal symmetry axis. The weak ferromagnetism [13, 14] was phenomenologically described by Dzyaloshinskii [15, 16] and later has been extended to a microscopic scale by Moriya [17] using spin-orbit coupling (SOC) and the Anderson's theory of superexchange. The antisymmetric Dzyaloshinskii-Moriya (DM) interaction is written as a vector cross-product and therefore favors non-collinear spin arrangement.

$$E_{\mathrm{DM}} = \sum_{ij}\mathbf{D}_{ij}\mathbf{m}_i \times \mathbf{m}_j \tag{1.3}$$

Another interaction of a relativistic origin, magneto-crystalline anisotropy (MCA), describes coupling of magnetic moments to the crystal lattice.

$$E_{\mathrm{an}} = \sum_i K_i \left(\mathbf{m}_i \mathbf{e}_i\right)^2, \tag{1.4}$$

where K_i is a symmetric second-order tensor of energy density. The sign of K_i defines the easy orientation of the magnetization with respect to the crystallographic directions. As discussed already in classical literature [18], anisotropy constants K_i of a ferromagnetic material are temperature dependent and at a certain point can change a sign. Thus a symmetry of magnetic structure changes. A ferromagnet can have three main phases (1.6): a state of an easy axis, an angular state and a state of an easy plane (see Fig. 1.1). Introducing θ angle as an order parameter, an anisotropy energy (1.5) of a hexagonal crystal can be written as follows:

$$E_{\mathrm{an}} = K_1 \sin^2\theta + K_2 \sin^4\theta, \tag{1.5}$$

where θ is an angle between a magnetization vector and a crystallographic c-axis.

$$\begin{array}{lll} \text{[a]}\ \theta = 0 \text{ or } \pi, & & (K_1 > 0) \\ \text{[b]}\ \sin\theta = \pm\sqrt{-\dfrac{K_1}{2K_2}}, & & (-2K_2 < K_1 < 0) \\ \text{[c]}\ \theta = \dfrac{\pi}{2}, & & (K_1 < -2K_2) \end{array} \tag{1.6}$$

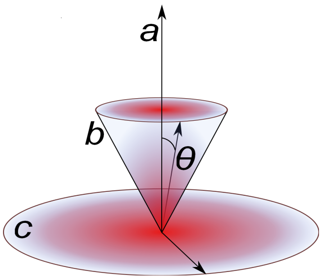

Figure 1.1: Three phases of a hexagonal ferromagnet: (a) easy axis, (b) angular state, (c) easy plane.

Magnetization direction can change between these three states depending on the sign of K_2. If $K_2 > 0$, then the [a]-[b] and [c]-[b] temperature-driven transitions are of a second order according to the condition:

$$K_1(T_1) = 0, \quad K_1(T_2) + 2K_2(T_2) = 0, \tag{1.7}$$

where T_i is a transition temperature. In case when $K_2 < 0$ the [b] phase is unstable, thus the easy-axis phase directly changes to the easy-plane phase. This first-order transition occurs at certain temperature T_0; the thermodynamic potentials of both phases become equal:

$$K_1(T_0) + K_2(T_0) = 0 \tag{1.8}$$

All aforementioned energy terms considered only internal interactions. When under the influence of external magnetic field, the system gains an additional Zeeman energy term:

$$E_\mathrm{Z} = \mathbf{H} \sum_i \mathbf{m}_i \tag{1.9}$$

Therefore, one can now write a complete Hamiltonian considering all energy contributions:

$$\begin{split}\mathcal{H} = -\frac{1}{2} \sum_{ij} J_{ij} \mathbf{m}_i \mathbf{m}_j + \sum_{ij} \frac{1}{r_{ij}^3} \left[\mathbf{m}_i \mathbf{m}_j - \left(\mathbf{m}_i \mathbf{e}_i \right) \left(\mathbf{m}_j \mathbf{e}_j \right) \right] + \\ + \sum_{ij} \mathbf{D}_{ij} \mathbf{m}_i \times \mathbf{m}_j + \sum_i K_i \left(\mathbf{m}_i \mathbf{e}_i \right)^2 + \mathbf{H} \sum_i \mathbf{m}_i\end{split} \tag{1.10}$$

Certainly, the aforementioned terms contribute unequally to the total magnetic energy. Depending on the ratio between them, a certain magnetic structure establishes: either homogeneous collinear or non-trivial with various modulations. The mechanism of magnetic modulations is described in the following section.

1.2 Modulated magnetic structures

A simple ferro-, ferri-, or antiferromagnetic structure can be modulated, which establishes a commensurate or incommensurate magnetic order. Commensurate modulations typically result from competing exchange (1.1) interactions: e.g., a triangular antiferromagnetic lattice [19, 20, 21, 22, 23], Kagomé lattice [24, 25, 26, 27, 28], canted magnetism [29, 30, 31, 32, 33, 34] or a spin ice [35, 36, 37, 38, 39]. To tolerate two antiparallel couplings with the nearest neighbors, magnetic moment has to deviate from its crystallographically favorable direction and often experiences a geometric frustration.

Inhomogeneous magnetic DM interactions (1.3), which are typically a few percent

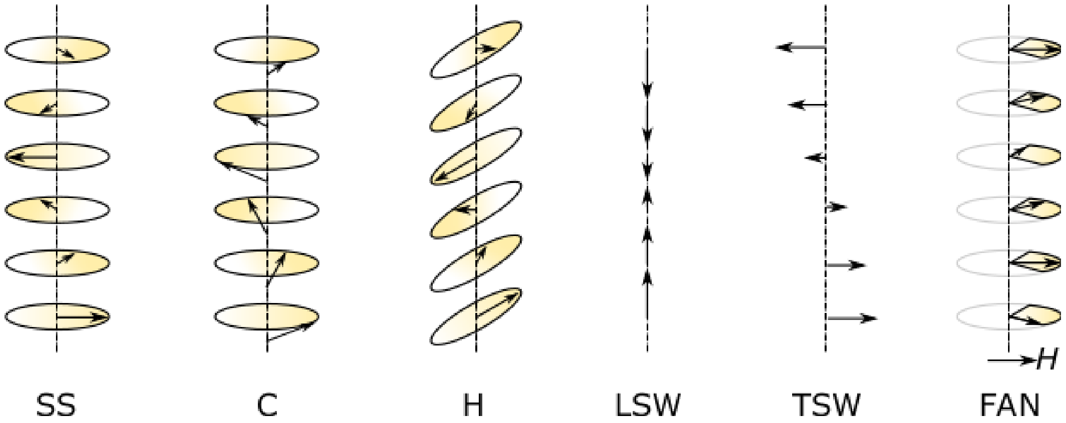

Figure 1.2: Typical modulated magnetic structures: spin spiral, conical, helical, longitudinal spin wave, transverse spin wave and fan, from [41].

of the J amplitude, can lead to the incommensurate magnetic modulations of a long periodicity. The simplest example can be represented by a spin spiral, which is a longitudinal or a transverse spin wave. The spin spiral is characterized by the vector $\mathbf{S}$ pointing perpendicularly to the spin rotation plane. The $\mathbf{S}$ can be non-collinear with the propagation of modulation resulting in a helical magnetic order. Helimagnetism can vary in forms as circular (first discovered in (Au_2Mn [40]) or elliptical; also it can be inclined with respect to the propagation direction. Schematically, helimagnetic order is represented as parallel planes: spins are collinear within each plane but tilted by a fixed angle between the adjacent planes [41]. A competition of helical and collinear structures can lead to the conical magnetic order [42]; alternatively some helimagnets can be driven into the conical state with the change of temperature and magnetic field [43]. Magnetic field can be also applied to induce a fan-type structure (see Fig. 1.2)

Inhomogeneous magnetic states are observed not only in highly-ordered magnetic crystals but also in locally disordered systems, e.g., when magnetic centers are randomly distributed in a non-magnetic lattice. A very minor concentration (a few at.%) of Mn in Mn-Cu alloy creates a complex magnetic map of mixed interactions. Mn atoms couple indirectly one with each other through the conduction electrons of non-magnetic Cu (the RKKY exchange). This interaction oscillates in sign and creates randomly distributed ferro- or antiferromagnetic spin arrangements resulting in a magnetic frustration. Such frustration is a superposition of many possible solutions. Though a system possesses no long-range regularity, the freezing of spins occurs at a well defined temperature. The spin glass behavior shows up in time-dependent magnetic measurements. For example, a zero-field-cooled (ZFC) magnetization curve as a function of temperature shifts up and reaches the field-cooled (FC) curve if a sample is first cooled and then left in field for several hours. Additionally, susceptibility measurements show a frequency- and field-dependent behavior of a transition peak [44, 45, 46]. A spin-glass behavior is rather difficult to control due to the large variety of local energy minima, which the system can occupy. Instead, we shall concentrate on magnetically ordered crystals, which allow for long- and short-range modulations. Being perturbed from a collinear spin arrangement, the system has to contain inhomogeneous DM terms. They are allowed to establish in systems with no inversion symmetry; additional degree of magnetization manipulation is realized by the presence of two antiparallel magnetic sublattices. The detailed description is given in the following subsection.

1.2.1 Non-centrosymmetric antiferromagnets

In noncentrosymmetric systems, the DM coupling (1.3) leads to and stabilizes the long-range magnetic modulations with the fixed sense of rotation [47, 48].

The relativistic DM interaction can be separated in a homogeneous and inhomogeneous part. Depending on these contributions, two-sublattice antiferromagnets can be classified in four types [49]. Collinear antiferromagnets, such as $CuCl_2{\cdot}2H_2O$, MnF_2, Cr_2O_3 and $GdAlO_3$ [50, 51] are the systems with both terms equal zero, meaning that there is no reason for modulations. Antiferromagnets with a weak ferromagnetism result from a hidden collinear arrangement of a staggered magnetization. Here only the homogeneous DM interaction is present; materials include $MnCO_3$ [13, 52], orthoferrites [53], manganites [54, 55] and hematites [15, 17, 56, 57, 58, 29]. The third type is the class of chiral helimagnets; long-range modulations appear only because of inhomogeneous DM interaction and are stabilized by the Lifshitz invariants [59, 41]. Typically such magnetic ordering forms in the cubic and other non-centrosymmetric structures. The last, fourth type, counts those antiferromagnets, where both homogeneous and inhomogeneous DM interactions are present establishing chiral helimagnetism and weak ferromagnetism simultaneously.

The materials discussed in this work are tetragonal non-centrosymmetric ferrimagnets of the D_{2d} symmetry class. It has been theoretically predicted [49] that magnetic crystals of this symmetry type exhibit modulations within the basal plane and are not expected along the crystallographic z-axis. The chiral modulations can appear within a certain window of parameters due to the competition between homogeneous interactions, inhomogeneous interactions and the magnetocrystalline anisotropy. The ratio between these energy terms can be tuned by varying the external conditions, e.g., magnetic field or/and temperature, thus inducing a magnetic phase transition.

1.2.2 Mechanism of phase transitions

A magnetic phase transition is phenomenologically described by considering magnetization vector(-s) as an order parameter. In a two-sublattice non-centrosymmetric system, which already possesses a certain anisotropy, the order parameter is two-component and distributes inhomogeneously in space. The periodicity of modulations is sensitive to the change of the effective magnetic anisotropy; by varying the external conditions, one can try to control them. E.g., the increase of anisotropy leads to the formation of regions with a constant commensurate phase separated by domain walls or solitons. When the anisotropy is further increased (e. g., by lowering the temperature), the it outweighs the inhomogeneous DM interactions and establishes a fully commensurate magnetic structure.

The free energy of such a system is described by the Ginzburg-Landau functional (for details see [41]):

$$\Phi = \int dz \left[r\,(\eta\xi) + u\,(\eta\xi)^2 + w\,(\eta^n + \xi^n) + V_{\mathrm{inh}}(z) \right] , \tag{1.11}$$

which contains the phenomenological parameters of the Landau theory of phase transitions: $u > 0$, $r \sim (T - T_{\mathrm{C}})$, magnetic anisotropy w and the inhomogeneous term $V_{\mathrm{inh}}(z)$ containing the spatial derivatives of the order parameter described through the Lifshitz invariants [18]:

$$\eta \frac{d\xi}{dz} - \xi \frac{d\eta}{dz} \,. \tag{1.12}$$

In other words, the spacial derivatives of magnetization vector(s) are defined as (for details see [49, 47])

$$M_i \frac{\partial M_j}{\partial x} - M_j \frac{\partial M_i}{\partial x} \,. \tag{1.13}$$

Some modulated magnetic structures prohibit Lifshitz invariants due to the symmetry reasons. In such systems, the temperature dependence of the modulation propagation vector is rather weak, which leads to the first-order (jump-like) transition into the commensurate phase.

In weak magnetic fields, the spin spiral is only slightly distorted. Increasing the field, one observes a fan-type magnetic structure (see Fig. 1.2). When the critical field value is reached, the fan structure collapses leading to the homogeneous spin structure along the external magnetic field.

The change of the external conditions like temperature, field or pressure can induce magnetic phase transitions: an antiferro-ferromagnetic transition [60], gradual spin reorientation in an antiferromagnet [61, 62, 63] commensurate-incommensurate magnetic phase transition [64]. Canted, conforming or a mixed magnetic structure are also thickness-dependent [65, 66]. A phenomenological description of the first- and second-order spin reorientation transitions has been well-developed by Hornet and Varma [67] and experimentally proven by Antonini and Paroli on $ErFeO_3$ [68] in 1984. Earlier works, refer to the observed spin transition processes in Mn_2Cr-based compounds [69]. Though unexpected [41], it has been recently discovered [49], that noncentrosymmetric magnetic crystals like tetragonal antiferromagnets $Ba_2CuGe_2O_7$ [70, 71, 72] and $K_2V_3O_8$ [73] can show both weak ferromagnetism along one direction and chiral modulations along another one. Moreover, under certain temperature-field conditions, a combination of a weak ferromagnetism with incommensurate structures can form magnetic vortices or skyrmions.

Experimentally, magnetic transitions can be observed on powder samples by neutron scattering technique [74, 75, 76, 21, 58, 22, 77, 78], Mößbauer [79, 61, 57] or nuclear magnetic resonance [43]. Theoretically, the transitions are explained by the phenomenological Landau theory using the Ginzburg-Landau functional for the inhomogeneous distribution of the order parameters [41, 80]. The responsible physical mechanisms are rather complex: systems which exhibit a localization of magnetic moments (like insulators or semiconductors) experience a competition of the nearest and the next-nearest neighbors. The electronic configuration at the Fermi surface can be modified by the external magnetic field leading to the magnetic transitions in the rare earth element (REE) based compounds. Some systems, e. g. CeSb, can exist in six different magnetic configurations in a temperature window from 8 to 16 K even in zero magnetic field. When applied, the field leads to the creation of new phases. Such magnetic evolution is explained by the strong inhomogeneous interactions: the inter-plane coupling is much weaker compared to the in-plane coupling and therefore can be easily perturbed by temperature or field [41].

Localized chiral structures in non-centrosymmetric uniaxial antiferromagnets

The areas between homogeneous regions with antiparallel staggered magnetization in weak ferro- (antiferro-) magnets form a domain wall, which corresponds to a spin spiral. Depending on the crystal symmetry, the non-centrosymmetric antiferromagnets favor a Bloch wall formation or a Néel wall (see Fig. 1.3). Though spin spirals have a fixed sense of rotation and the appearance of modulations with the opposite winding is highly unstable, the domain walls of both rotational orientations can equally arise in the antiferromagnet. In such systems, the reason for the domain wall creation is of the kinetic origin as the domains nucleate during the magnetization reorientation transitions. The processes of transitions into the ordered states are independent on the domain wall energies.

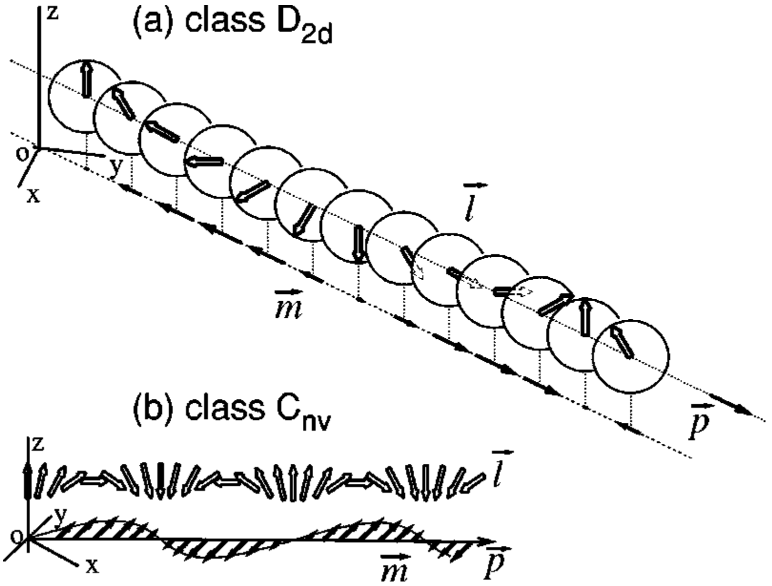

Figure 1.3: Basic modulated structures for different symmetry types: helicoid and cycloid, from [49].

In the zero magnetic field or below the spin-flop transition and applied along the z-axis, the magnetic free energy is invariant to rotation around the z-axis; the staggered magnetization is axially symmetric in the basal plane and uniform along the z-axis. This magnetic configuration corresponds to the topological excitations, which is stabilized by the inhomogeneous DM interactions [81] (see Fig. 1.4). Depending on the applied field, the vortices may exist in two phases. The localized vortices (see

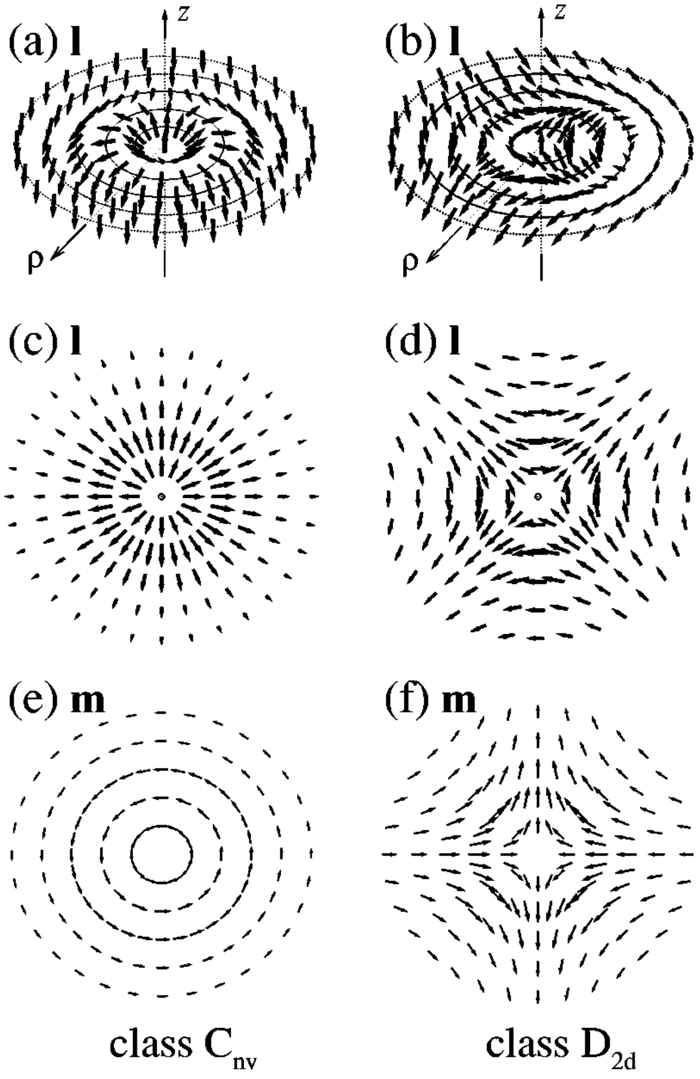

Figure 1.4: Vortex structure for antiferromagnets with different symmetry types, (a) and (b) distribution of staggered vector, (c)-(f) projections of the staggered vector and oscillating total magnetization in the basal plane, from [49].

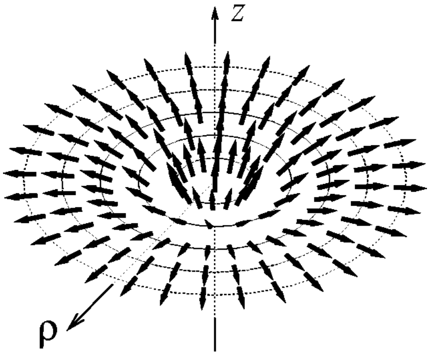

Figure 1.5: Delocalized vortex in the spin-flop phase, distribution of the staggered magnetization vector, from [49].

Fig. 1.4) establish in the fields below the spin-flop transition, while in the spin-flop phase they delocalize (see Fig. 1.5). When the magnetic field is slightly deviated from the z-axis, the axial symmetry of the system is disturbed and the delocalized vortex [81] develops various elongated shapes. Such nonsingular linear defect structures are topological structures, which are unstable in centrosymmetric magnetic crystals due to the influence of internal anisotropic interactions or applied field; they can be stabilized by the Lifshitz invariants (see 1.2.1) and therefore non-centrosymmetric crystal structure is required.

Skyrmion phase in different materials

The problem to describe countable particles in continuous fields [82] was solved by T. Skyrme who specified them as certain localized states [83]. Later this model has found a broad application range from microscopic to a cosmological scale [84, 85, 86, 87]; in the context of magnetism they were introduced as ”skyrmions” by Bogdanov [81]. Though some systems require special external conditions - magnetic field, temperature or rapid growth of topological defects [88, 89, 90] - to be driven into the skyrmion phase, others can form a spontaneous skyrmion lattice as a ground state [91].

First, the magnetic skyrmion phase has been experimentally observed in a chiral itinerant single-crystalline magnet MnSi [77]. Using a small-angle neutron scattering, a six-fold symmetry pattern has been observed in a reciprocal space independent from the sample’s orientation in the external field. In this material, the skyrmion phase appears in the vicinity of a conical-paramagnetic phase transition within a temperature range of 27-29 K and external field of roughly 0.1-0.25 T.

Another helimagnet, FeGe [79], was examined in a direct space using the transmission electron microscopy in a Lorenz mode (Lorenz-TEM) [92]. It has been also shown, that initially tiny area on the field-temperature phase diagram can be several times enlarged by the increasing shape anisotropy while thinning the sample from 75 nm down to 15 nm [93].

Formation of a skyrmion lattice is an interesting fundamental problem, whereas an ability to manipulate a single skyrmion becomes an exciting industrial hunt. Due to the interface symmetry breaking, a spontaneous skyrmion lattice was observed not in a bulk but on a Fe-monolayer deposited on Ir using the spin-polarized scanning tunneling microscopy (SP-STM) [94]. Recently, a creation and annihilation of a single skyrmion by the spin-polarized current has been reported [95].

All the aforementioned discoveries ignite a scientific thirst for new functional magnetic phases in new materials. Presently, the amount of compounds showing a skyrmion state is very limited, therefore, an expansion of the materials base is vital. Counting more than 1500 members, Heusler compounds offer a flexibility of the lattice parameter, magnetic moment, Curie temperature, magnetic anisotropy, spin polarization and a spin-orbit coupling. All these characteristics are vitally important for industrial applications. Recently emerged Mn_2-based Heusler family is especially attractive due to the presence of two ferrimagnetically aligned Mn sublattices, which result in a small net magnetization and an additional possibility of a separate sublattice manipulation. Some of them crystallize in the non-centrosymmetric structure and therefore exhibit DM interactions. The inhomogeneous part of the DM interactions can be amplified by relativistic effects such as spin-orbit coupling, which is provided by the heavy constituting elements. Heusler compounds are suitable candidates to realize almost any engineering task, including the formation of a skyrmion phase.

1.3 Technological advances and history of Heusler compounds

Heusler alloys are named after their discoverer, a German miner and a chemist Dr. Friedrich Heusler, who found that some of Mn-based compounds become ferromagnetic despite that none of the constituting elements exhibits ferromagnetism [96].

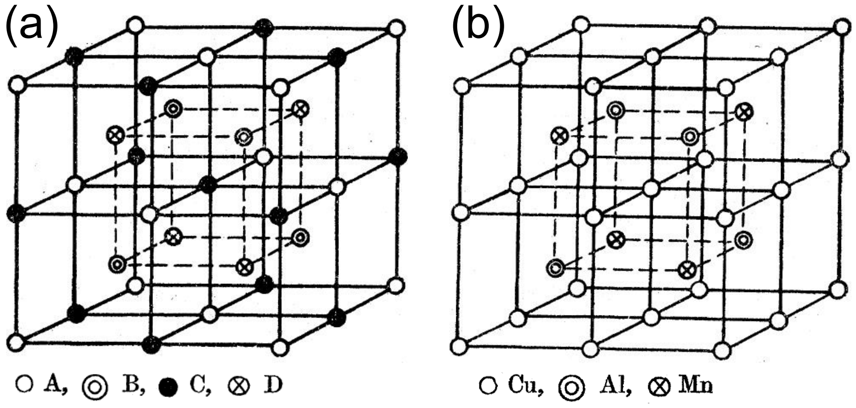

Figure 1.6: (a) Crystal structure of a Heusler alloy, (b) crystal structure of a quenched alloy that exhibited magnetic response, from [97].

This has lead to a new research direction in magnetism of Manganese alloys. By adding different elements to the manganese-copper premelt - such as zinc, arsenic, antimony, bismuth or boron - it was possible to increase the magnetization, especially if the amounts of elements were proportional to their atomic weight.

The structure of the Cu_2MnAl was discussed about 30 years later by Bradley and co-workers [97], who reported a body-centered cubic lattice with a face-centered superlattice (see Fig. 1.6). Quenching of a sample led to a better magnetic response; additionally, the quenched samples exhibited slightly different site occupancies in the crystal lattice. Later, magnetic and mechanical behavior was studied under the influence of different annealing regimes.

A new era of Heusler compounds started in 1983 with the prediction of half-metallic properties [100] in this class of materials by Kübler [101] and De Groot [102]: referring to the spin-resolved density of electronic states (DOS), see Fig. 1.7 [98, 99], one finds a sizable energy band gap in the minority states (half-metallicity). Half-metallic cubic Heusler compounds follow the so-called Slater-Pauling (SP) [103, 104] behavior, which stipulates that the total magnetic moment of $3d$ elements and their binaries can be estimated by the mean number of valence electrons per atom: one added valence electron occupies majority-spin band of the system and thus the total magnetic moment increases by 1 μ_B.

A high spin polarization, which is simply the relative difference between spin-up and spin-down conducting electrons, is one of the crucial requirements for the modern spintronics technology, which is nowadays substantially focused on a Heusler family.

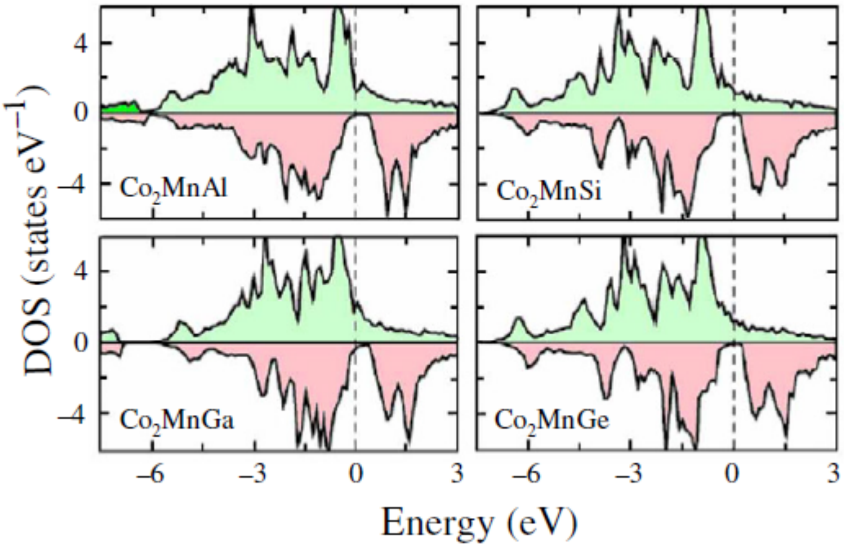

Figure 1.7: Spin-resolved density of states of Co$_2$MnZ (Z=Al, Si, Ge and Si), from [98, 99]. Positive (green) and negative (red) areas correspond to the majority (up) and minority (down) spin-channels, respectively.

Twenty years after the prediction of half-metallicity, the Co$_2$Cr$_{0.6}$Fe$_{0.4}$Al compound has been implemented into a magnetic junction, showing 19% of a tunneling magnetoresistance (TMR) effect at the room temperature [105]. The highest achieved room temperature TMR ratio using Heusler electrodes (Co$_2$MnSi/MgO/Co$_2$MnSi) is 354% [106]

Due to simple crystal structure, the physical features can be often estimated prior to experimental attempts. By means of *ab-initio* calculations Kübler and co-workers have shown that the Curie temperature T_C and the magnetization of some half-metallic ferromagnetic Co$_2$-based Heusler compounds depend the amount of the valence electrons [107]. The highest ever T_C = 1120 K and magnetic moment of 6 μ_B were reported for the Co$_2$FeSi half-metallic ferromagnet [108].

These significant developments have opened new technological horizons for the magnetic random access memory (MRAM) technology and the spin-transfer torque (STT) [109, 110] applications, for which the Mn$_2$- group became especially suitable. It has been found that a prototypical ferrimagnet Mn$_3$Ga (Mn$_2$MnGa) [111] possesses necessary ingredients for the STT, such as 88% of theoretically calculated spin polarization [111], a low magnetic moment, a high T_C and a large energy product of the magnetic hysteresis. The structure exhibits about 30% of a tetragonal distortion, which leads to a large MCA and a robust thermal stability of magnetization, necessary for the ultra-high density magnetic storage devices. It has been shown, that the chemical doping works as an advanced functional tool on this system. First, a partial substitution of Mn by Co allows for a reduction of the total magnetization [112]. Second, the spin-transport characteristics can be improved by a constructive disorder [113].

Heusler compounds are stable in a cubic structure; tetragonal distortion is an attempt of the system to compensate for the instability, which appears at the Fermi energy. As a result, tetragonally strained compounds do not form an energy gap in the minority spin channel. Nevertheless, the spin transport properties can be efficiently manipulated in each channel separately [113].

To demonstrate their industrial applicability, the bulk properties of the Mn_3Ga-related compounds were enhanced in thin film samples [114, 115, 116]. Nowadays, the Mn_2-based Heusler family is a hot topic and is being extensively developed.

2 Giant non-collinearity and a spin-reorientation transition in bulk Mn_2RhSn tetragonal Heusler magnet

Non-collinear magnets provide essential ingredients for the next generation memory technology. It is a new prospect for the Heusler materials, already well-known due to the diverse range of other fundamental characteristics. Here the combined experimental/theoretical study of novel non-collinear tetragonal Mn_2RhSn Heusler material is discussed, which exhibits unusually strong canting of its magnetic sublattices. It undergoes a spin-reorientation transition, induced by a temperature change and suppressed by an external magnetic field. Due to the presence of Dzyaloshinskii-Moriya exchange and magnetic anisotropy, Mn_2RhSn is suggested to be a promising candidate for realizing the skyrmion state in the Heusler family.

2.1 Preface

The art of controlling magnetic degrees of freedom has led to a broad range of applications that make up the rapidly developing field of spintronics. Up to now, most of the exploited compounds have been so-called collinear magnets, i.e. materials in which the magnetization is formed by local magnetic moments aligned parallel or antiparallel to one another. Yet, the possibility of influencing their mutual orientation opens new horizons for the field of spintronics. Non-collinear magnets can be widely applied in current-induced spin-dynamics [117], magnetic tunnel junctions [118], molecular spintronics [119], spin-torque transfer by small switching currents [120] and anomalous exchange bias [121]. Impressive improvement of the critical current density by five orders of magnitude [78, 122, 123] is offered by non-collinear magnets driven into the skyrmion phase [124, 77, 125, 78, 126, 122, 127, 123, 128]. While such exotic magnetic arrangements are sensitive to external conditions (magnetic field and temperature), an expansion of the related material base is important for their stabilization.

Flexible tuning of the magnetic properties can ultimately be realized in multi-component systems of several magnetic sublattices with competing types of interactions such as magneto-crystalline anisotropy, dipole-dipole and Dzyaloshinsky-Moriya (DM) interactions [129, 17]. Heusler compounds, of which there are over 1500 members, provide a rich variety of parameters for almost any material engineering task (e.g. half-metallic ferromagnetism [101, 100], exchange bias [130], topological insulators [131], spin-gapless semiconductivity [132], spin-resolved electron localization [113] and superconductivity [133]). Furthermore, the majority of Mn_2YZ (Y – transition metal, Z – main-group atom) systems are non-centrosymmetric; this together with the magneto-crystalline anisotropy induced by intrinsic tetragonal distortion makes such systems attractive for skyrmion research.

First, the unusual ground-state magnetic canting will be discussed, which is observed in Mn_2RhSn together with the subsequent temperature-induced spin-reorientation into the collinear ferrimagnetic mode. Further, a detailed micromagnetic analysis will be given, which suggests this collinear regime to provide perfect conditions for the skyrmion formation, in agreement with the earlier theoretical studies [81, 124, 49].

2.2 Sample preparation and precharacterization

In order to prepare a high-quality sample, a special care has been taken on the Mn purity. The element can have 5 different oxidation states: +2, +3, +4, +6 and +7, each being a corresponding color: pale pink, red, black, green or purple. To eliminate any presence of oxides, the following procedure was performed. Mn chips were sealed in evacuated quartz ampules with relatively large internal volume and heated at 1000°C overnight. Clean Mn surface shined with bright silver color.

Arc-melting is a quick technique for sample preparation. Also, it prevents them from contamination as no crucible is involved. A lower part of a sample, which lies on the water-cooled copper heart never melts completely and copper does not react with the sample. Polycrystalline bulk samples were repeatedly arcmelted from stoichiometric amounts of high-purity commercially available elements ($> 99.99\%$) in an Ar atmosphere and Ti getter. An overall mass loss is less than 0.5 wt.%.

To achieve a desired stoichiometry and reduce the evaporation of Mn, a two-step process was used: first, premelts of Rh-Sn were prepared to reduce the melting point of refractory Rh-element. According to phase diagram (see Fig. 2.1), these elements react well with each other and form a stable phase. For the second run, a

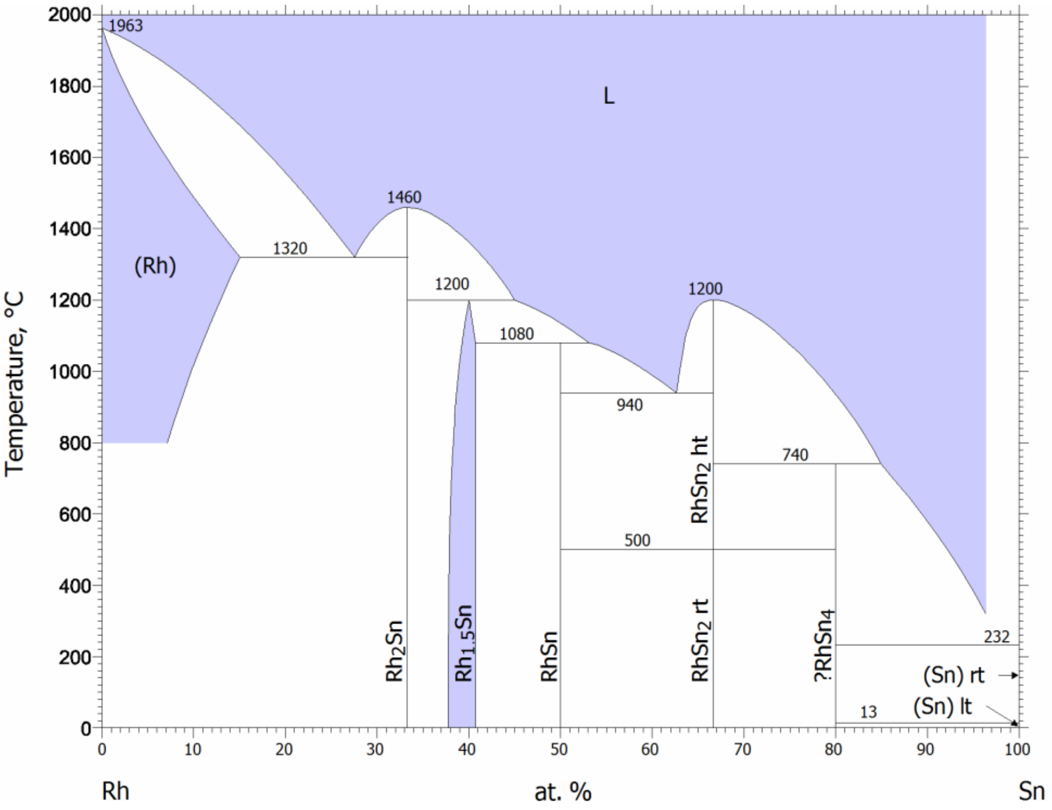

Figure 2.1: Phase diagram of Rh-Sn binary, 1:1 ratio forms a stable phase, from [134]

corresponding amount of Mn was placed below the Rh-Sn premelts. Thus, Mn was slowly absorbed by the molten Rh-Sn phase. To ensure homogeneity, the samples were melted 3 times on each side with increasing arc power.

Later the ingots were wrapped in Tantalum foil and sealed in evacuated silica tubes. Annealing lasted 1 week at 800°C. Samples were slow-cooled and pre-characterized. Prior to structural and element-specific analysis, all samples were investigated by optical microscopy in a bright light (see Fig. 2.3), polarized light and differential interference contrast regimes. This is a fast technique, that covers large areas of a sample. In the bright field observations any flat feature that is perpendicular to the incident light appears to be white. Imaging in a polarized light revealed an additional contrast in a way of perpendicular stripes, which suggested a possible tetragonal crystal structure.

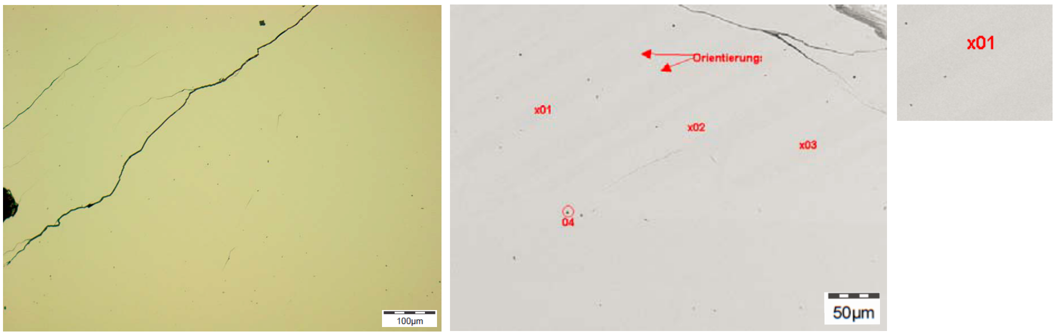

Figure 2.3: Optical and SEM image of the homogeneous Mn$_2$RhSn phase; composition analysis was performed at the areas marked. The Mn$_2$RhSn stoichiometry is constant across the whole sample; a minor impurity of Mn$_{3.5}$RhSn is present at around 1 at.% and does not bias the presented results.

Spot	Mn (at.%)	Rh (at.%)	Sn (at.%)
1)	49.73	25.55	24.71
2)	48.79	25.73	25.48
3)	47.84	26.23	25.93

Table 2.1: EDX analysis of the Mn$_2$RhSn sample taken from the areas indicated in Fig. 2.3. The composition is well reproduced across the whole observed area.

For the energy-dispersive X-ray (EDX) spectroscopy / scanning electron microscopy (SEM, see Fig. 2.3) a well-polished surface was required to eliminate topological distortions. In addition, an electron penetration depth is in a μm range. For this reason the samples were embedded in epoxy resin blocks and a smooth surface was prepared. Metallographic analysis revealed that the sample is a single-phase material with a homogeneous composition distribution. The composition was characterized by the EDX spectroscopy at the precision of $\leq$0.5 at.%., values are summarized in Tab. 2.1 and are in a good agreement with the intended values.

2.3 Crystal structure analysis

In this chapter the crystallographic parameters of Mn_2RhSn are discussed. First, the room-temperature X-ray powder pattern is analyzed, then the temperature-dependent evolution is studied.

2.3.1 Inverse tetragonal Heusler symmetry

Heusler compounds can be divided in two distinct types: X_2YZ, a full-Heusler and XYZ, a half-Heusler structure with a main group element and two transition metal elements. By taking 4 interpenetrating fcc sublattices and filling the octahedral sites, a half-Heusler structure is obtained. For getting the full-Heusler structure, the tetrahedral sites should be added. Both full- and half-Heusler structures are initially cubic, they belong to $Fm\overline{3}m$ (space group no. 225) and $F\overline{4}3m$ (space group no. 216) [135].

For certain crystallographic reasons, atoms of the X element can occupy different lattice sites. Contrary to the regular full-Heusler compound having X in equal (1/4, 1/4, 1/4), Y in (1/2, 1/2, 1/2) and Z in (0, 0, 0) Wyckoff positions, an inverse compound [136, 137] has its X element sitting in two different places. Here X is in (1/2, 1/2, 1/2) and (3/4, 3/4, 3/4), Y in (1/4, 1/4, 1/4) and Z in (0, 0, 0) respectively. The reason for such an inversion is in higher electronegativity of Y element or its atomic size in comparison to the X element. Mn_2- as well some Fe_2-based compounds are the most known examples [138, 139, 140, 141, 142, 143].

The majority of Heusler compounds are stable in the cubic phase. Some, however, are susceptible to the tetragonal distortion. The discussion about the tetragonal strain around the transition metal cation has started in fifties; various scenarios were considered - ordering of the chemical bonds or crystal field splitting, see [144, 145, 146, 147, 148]. Back in thirties, Jahn and Teller [149] suggested that the orbital degeneracy in polyatomic molecules can be healed by the nuclear displacement of the ligands. This is accompanied by the splitting of the degenerate state into two energy levels - therefore, the displacement is a function of the orbital splitting and vice versa. Later, the Jahn-Teller mechanism was translated to the crystal solids: perovskite type manganites, transition metal oxides or spinels [146, 148] - systems with localized electronic states. In case of metallic Heusler compounds, where electrons are rather itinerant and experience collective phenomena, such an approach cannot be straightforwardly applied. Electronic states are severely intermixed and can simultaneously belong to several atoms of the unit cell. Here, the

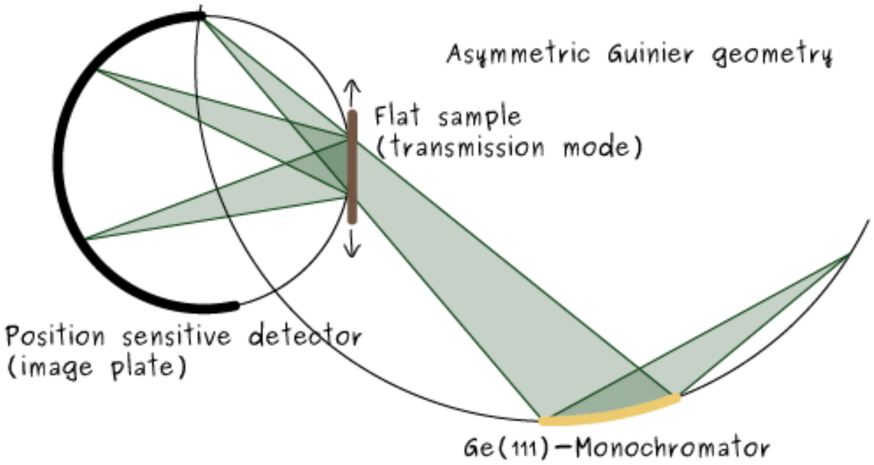

Figure 2.4: Image plate Guinier camera Huber G670. From [150]

origin of the tetragonal distortion lies in the instability peak on the ϵ_F in the cubic phase. To relax from the instable state, the structure elongates ($c/a > 1$) or flattens ($c/a < 1$) along the c-axis. The distortion results in the regular or inverse tetragonal structure. In the regular $I4/mmm$ (space group no. 139) structure, constituting elements occupy the following Wyckoff sites: X is in $4d$ (0, 1/2, 1/4), Y and Z are in $2b$ (0, 0, 1/2) and $2a$ (0, 0, 0) respectively. Whereas, the inverse structure $I\bar{4}m2$ (space group no. 119) is represented by X in $2b$ (0, 0, 1/2) and $2c$ (0, 1/2, 1/4) sites, Y and Z locate in $2d$ (0, 1/2, 3/4) and $2a$ (0, 0, 0) respectively.

The room temperature powder X-ray diffraction pattern was obtained in asymmetric Guinier transmission geometry (Image plate Guinier camera Huber G670, Cu K_α radiation, see Fig. 2.4) with LaB_6 added as an internal standard. This setup is advantageous for the routine sample analysis, can handle air-sensitive compounds, require relatively short time for one measurement (1.5 - 3 hours) as well as the small sample quantity. To improve the peak-width and eliminate the powder size distribution, each sample has been preliminary sieved through 40 μm mesh. However, a certain peak asymmetry was still noticeable at low 2θ angles, therefore a high-resolution synchrotron data were necessary. The obtained powder XRD patterns were refined by the Rietveld method with the help of FullProf [151] software. The treatment was done in 10 steps: optimization of scale, peak shape, zero shift, background modeling, lattice constants, thermal expansion parameter, overall temperature factor, half-width parameters (U, V, W), peak asymmetry and a ratio of Lorentian-to-Gaussian peak profile.

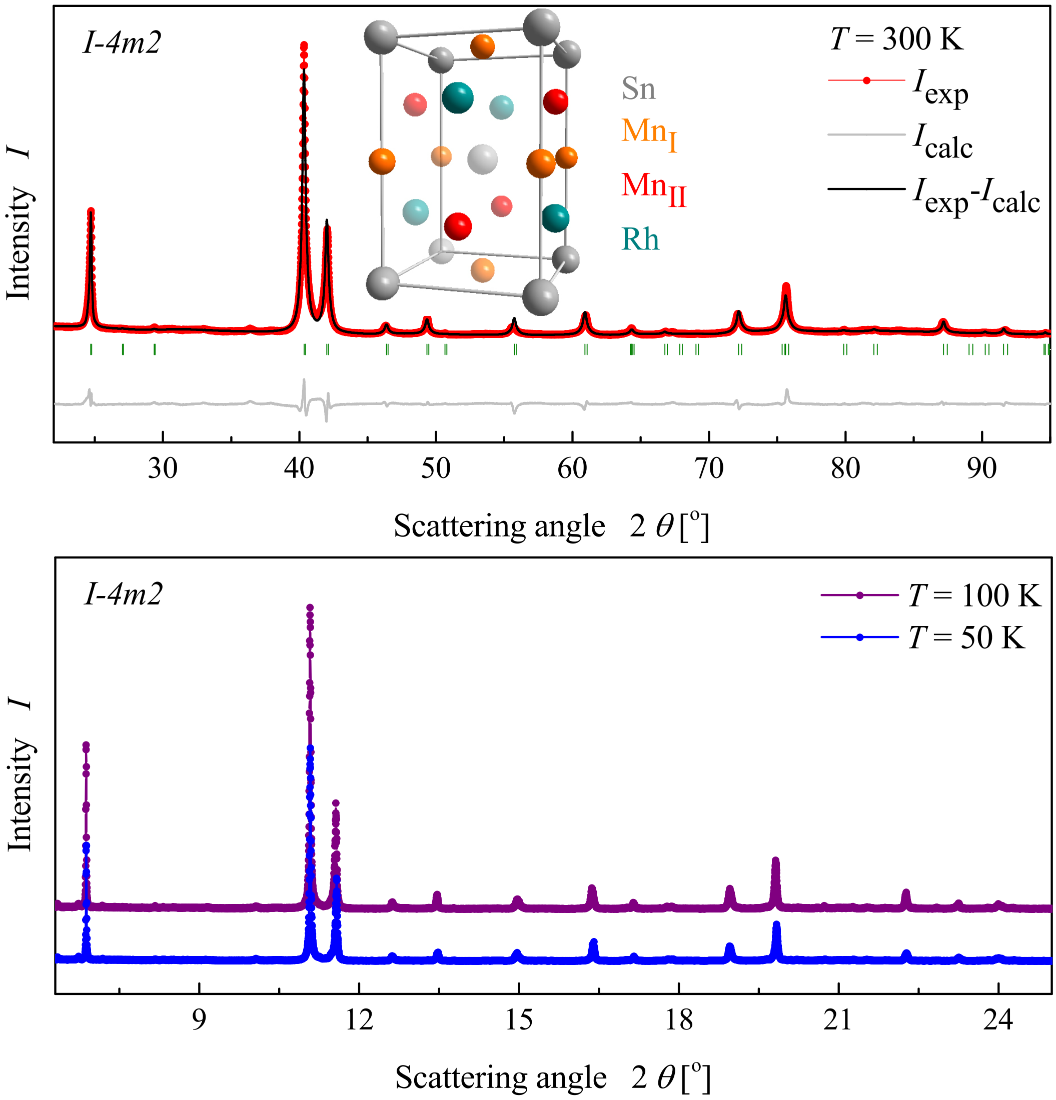

Figure 2.5: Powder X-ray patterns obtained at room temperature (top) and 50 and 100 K (bottom). The colored and black lines correspond to the observed and calculated intensities, respectively. Incident light wavelengths of λ = 1.5405 Å and 0.43046 Å were used for the room- and low-temperature measurements, respectively. The high-resolution XRD data are consistent with the $I\bar{4}m2$ symmetry and confirm the tetragonal crystal structure at low temperatures.

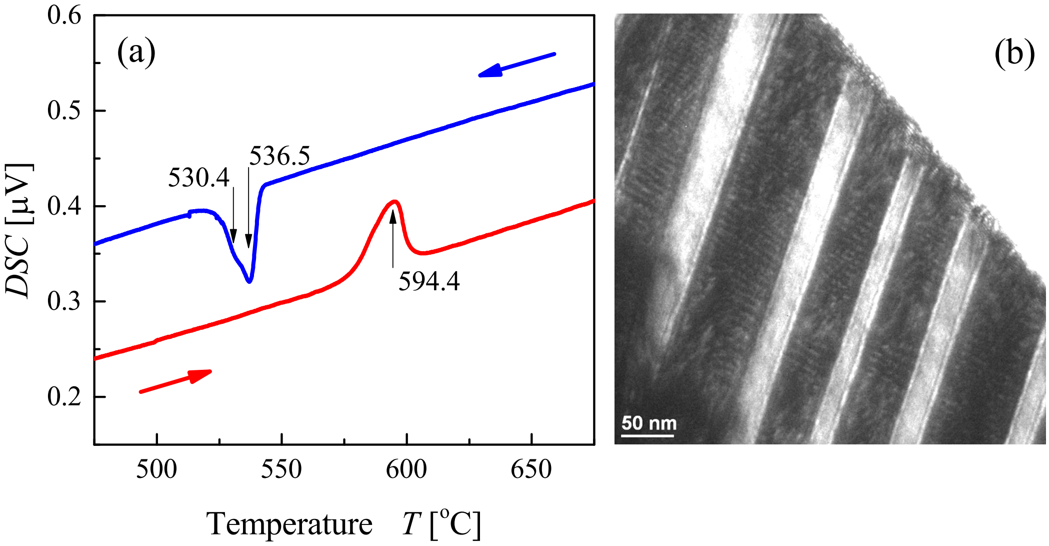

Figure 2.6: High-temperature cubic phase of Mn_2RhSn. (a) Differential scanning calorimetry data show a reversible transition peak. (b) Twinned structure forms as a result of tetragonal transition.

The refined XRD pattern reveals that the Mn_2RhSn crystallizes in the inverse tetragonal Heusler cell (so-called $I\bar{4}m2$, 119 symmetry type), see Fig. 2.5. The obtained lattice parameters are $a = 4.298$ Å and $c = 6.593$ Å with the corresponding tetragonal distortion $a/\sqrt{2}c$ of 8%.

The structural parameters were tested at lower temperatures (see Fig. 2.5) using a high-resolution X-ray diffraction at ESRF, Grenoble with the incoming beam wavelength of $\lambda = 0.43046$ Å. Powder samples were sealed in 0.3 mm glass capillaries in a glovebox under the Argon atmosphere. During the measurement, a capillary rotated at a constant speed in order to collect a sufficiently statistical signal. The high-resolution synchrotron experiments proved the suggested crystal parameters.

2.3.2 High-temperature cubic phase

To examine the temperature stability of the inverse tetragonal Heusler structure, the differential scanning calorimetry (DSC) was performed from the RT up to 1500°C. The powder sample of ~ 50 mg was encapsulated in the Al_2O_3 crucible and heated under the Argon atmosphere.

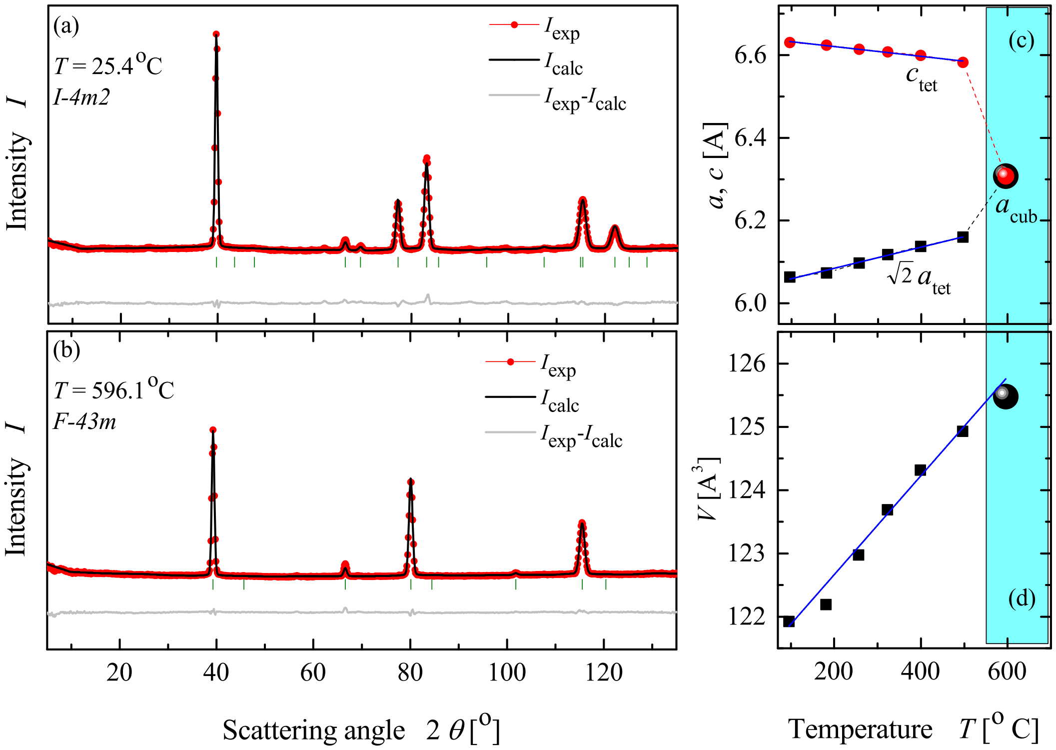

Figure 2.7: High-temperature structure analysis of the Mn_2RhSn by the neutron powder scattering. The wavelength of incoming neutrons is $\lambda = 2.448$ Å. (a) Refined pattern of the room-temperature ($T = 25.4°$ C) tetragonal structure, $I\bar{4}m2$, 119 symmetry type. (b) Refined pattern of the high-temperature ($T = 596.1°$ C) cubic structure, $F\bar{4}3m$, 216 symmetry type. (c) Evolution of the lattice parameters with the temperature up to the transition point. (d) Temperature-dependent behavior of the unit cell volume. Green ticks show the positions of Bragg reflexes on the (a) and (b). Blue line corresponds to the linear fit on the (c) and (d).

Fig. 2.6, (a) reveals the reversible structural transition. While heated, the system undergoes an exothermal process and the opposite, endothermal, during cooling. To clarify the symmetry change, temperature-dependent elastic neutron scattering was performed from the room temperature (RT) to the temperature above the transition and back (see Fig. 2.7). The measurements were done at the E6 focusing powder diffractometer (Helmholtz-Zentrum Berlin, Germany). The applied wavelength was $\lambda = 2.448$ Å. The refined RT-pattern confirms the $I\bar{4}m2$ (group no. 119) structure.

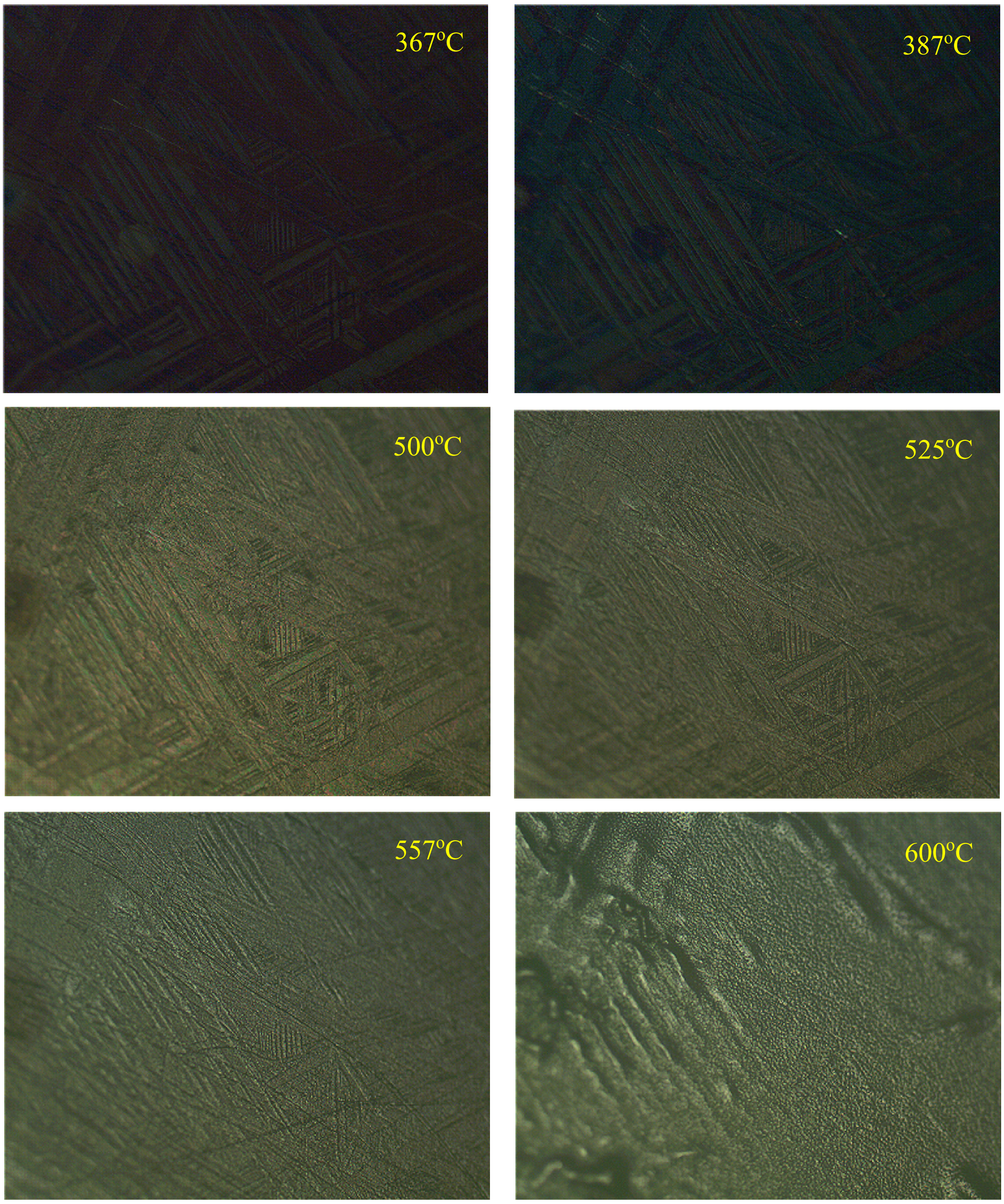

Figure 2.8: Optical microscopy under the polarized light - twinned structure is present up to the 557°C, which corresponds to the tetragonal phase of Mn_2RhSn. The twinned texture gradually fades with heating; in the cubic phase only the sample's topography is observed (600°C).

By increasing the temperature, the a and c parameters gradually change with a linear dependence (see Fig. 2.7, (c)). Interestingly, the a parameter grows nearly twice faster than the c parameter drops: the corresponding slopes are 2.541×10^{-4} Å/K and -1.177×10^{-4} Å/K respectively. Consequently, the volume change also follows a linear dependence, both below and above the transition temperature (see Fig. 2.7, (d)), with the slope of 782×10^{-4} Å/K and no visible discontinuity up to the formation of the $F\bar{4}3m$ structure (space group no. 216). Since the transition is accompanied by a certain temperature hysteresis (about 60° C), it is assigned to the first-order. While cooled, a sample undergoes a two-step process: the endothermal peak shows not an asymmetry (as observed while heating) but rather a distinct shoulder or even contains an additional small peak at the lower temperature side. This feature can be attributed to the complex formation of twins. A detailed analysis of the transmission electron microscopy (TEM) image (Fig. 2.6, (b)), reveals a peculiar hierarchy of twins in a tetragonal phase: the structure contains twins of about 50 nm, which, in turn are composed of $\sim$ 10 nm sub-twins.

The twined texture was also observed from the RT up to 600°C using the optical microscopy under the polarized light (see Fig. 2.8). The twins are clearly resolved in the tetragonal phase of Mn_2RhSn and vanish at the temperatures above the tetragonal-to-cubic phase transition.

Taking the experimentally determined structural parameters at the RT, both cubic and tetragonal phases were examined in terms of the spin-resolved density of electronic states. Allowing no volume variation of the unit cell, it was proved that the cubic phase is not stable at the room temperature due to the sharp feature at the ϵ_{F}. The peak originates from the spin-down d-states of the tetrahedrally coordinated Mn_{II} atom. Due to the crystal field effects, the degenerated t_{2g} orbital tends to split into two more favorable energy levels: upper xy and lower xz, yz. Such a splitting is accompanied by the nuclear displacement and a tetragonal strain along the c-axis. The in-plane xy orbital will be higher in energy due to the reduction of the distances to the in-plane ligands, whereas the xz and yz orbitals will reduce their energy with respect to the t_{2g} level of the cubic state. The ϵ_{F} is sensitive to the volume change: while increasing the volume, the ϵ_{F} moves down towards to valence band and leaves the instability above - cubic phase becomes robust.

Having the detailed analysis of the crystal structure, the reader can now focus on the magnetic behavior of the material.

2.4 Evolution of magnetic structure

Temperature dependent magnetization measurements have been performed at constant field sweeps ranging from 0.1 to 5 T using Quantum Design MPMS XL superconducting quantum interference device (SQUID) magnetometer in the zero-field-cooled (ZFC) and field-cooled (FC) regimes. Total magnetization was obtained from the hysteresis loops at 1.8 K. Ac-susceptibility measurements were done in a Quantum Design physical properties measurement system (PPMS) at the lowest possible DC-field of 50 Oe and frequencies ranging from 33 to 9997 Hz. Heat capacity measurements were carried out using a bulk policrystalline piece of about 50 mg from the RT down to 2 K.

The temperature-dependent magnetization shows rather non-trivial behavior (see Fig. 2.9, (a)). While cooling down from the RT, two transitions are revealed: a field-independent transition at about 270 K and a field-sensitive transition between 100 and 50 K. Initially, the field-independent establishment of a ferrimagnetic order from a paramagnetic state will be discussed.

2.4.1 Paramagnetic - ferrimagnetic transition

The magnetization (see Fig. 2.9, (a)), ac-susceptibility (see Fig. 2.9, (b)) and heat capacity measurements (see Fig. 2.9, (c) and (d)) show the formation of a magnetic order (T_C) at about 270 K. This is a second-order transition, which is mapped by the *lambda*-anomaly (see Fig. 2.9, (c)). Subtracting the baseline and using the graphical entropy-conserving equal-areas approximation, the ”jump” of specific heat ΔC_P and the transition temperature T_C were obtained as 12 J/mol K and 264 K respectively. The values contain a certain deviation due to the asymmetry in the peak shape, though the T_C is in a good agreement with the results of magnetization measurements (270 K); thus the bulk origin of the observed effect can be confirmed. The energy of magnetic ordering is defined as an integrated area under the peak (baseline subtracted): 453 J/mol.

The unit cell of Mn_2RhSn contains four atoms per unit cell; according to the empirical Dulong-Petit law, given in Eq. (3.3), the phonon heat capacity should be saturated at about 100 J/(mol K). Additional contributions are provided by the electron and magnon scattering described by the second and the third terms in Eq. (3.14). While the electron part is present within the whole temperature range, the magnon contribution starts to play role from 50 K on (Fig. 2.9, (c) and (d)) and is responsible for the magnetic ordering transition at $T_C = 270$ K. Below this

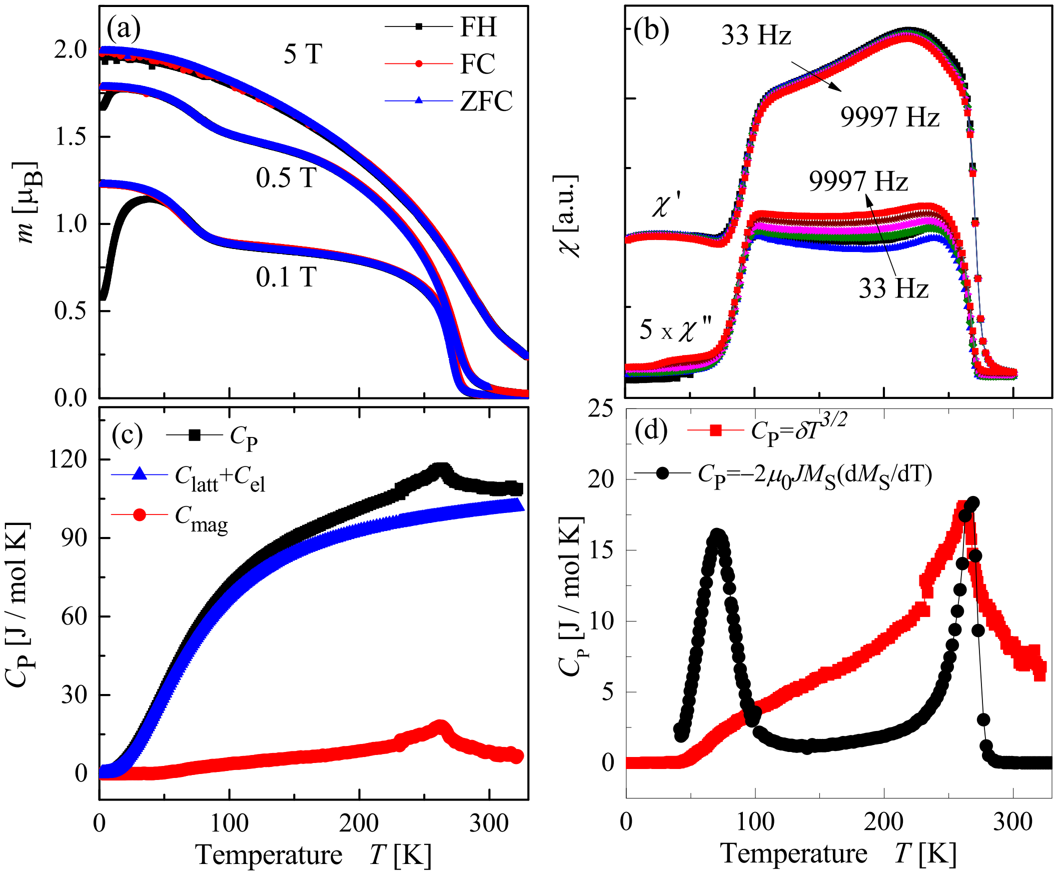

Figure 2.9: (a) Zero-field cooled (ZFC), field-cooled (FC) and field-heated (FH) magnetization as a function of the temperature measured at different induction fields of 0.1, 0.5, and 5 T; two transitions are observed - at 270 K and in the range of 100–50 K. (b) Real (χ') and imaginary (χ'') parts of the ac-susceptibility are frequency-independent and show confirm the transitions by two pronounced steps: at 270 K and at about 80 K. (c) Zero-field heat capacity: phonon, electron and magnon contributions. (d) Magnetic contributions to the heat capacity: extracted from the total heat capacity and reconstructed from the magnetization measurement.

temperature, the compound forms a ferrimagnetic structure, which will be discussed below.

Magnetic heat capacity can be derived from the total heat capacity (for more details see Section 3.5) as well as can be reconstructed from the temperature-dependent magnetization measurement [152] (see Fig. 2.9 (d)). In both cases, the paramagnetic transition at about 270 K is well reproduced.

Applying the mean-field approximation, one can obtain the Curie constant as

$$\chi = \frac{C}{T - T_\mathrm{C}} = \frac{N\mu_0\mu_\mathrm{eff}^2}{3k_\mathrm{B}}\,, \tag{2.1}$$

the T_C is defined as $T_\mathrm{C} = \alpha C$. Here α is the Weiss mean-field (molecular field) constant. The high-temperature dc-susceptibility measurements in the external field of 1 T reveal the effective magnetic moment $\mu_\mathrm{eff} = g\sqrt{S(S+1)} = 2.824\sqrt{\chi T} = 5.59\ \mu_\mathrm{B}$, which is close to the effective spin $S = 5/2$ per formula unit. The magnetic component of the specific heat corresponds to the total exchange self energy of the material per formula unit as $C_\mathrm{m} = \partial w_\mathrm{ex}/\partial T$, which gives an estimate for the mean field constant α and exchange interaction J:

$$C_\mathrm{m} = -2\mu_0\alpha M_\mathrm{S}\frac{\partial M_\mathrm{S}}{\partial T} \tag{2.2}$$

and

$$J = \frac{\mu_0 N\alpha m^2}{zS^2}\,, \tag{2.3}$$

where $z = 8$ corresponds to the number of the nearest neighbors and $S = 5/2$ is the total spin per atom. A rough estimate of the J from T_C, low-temperature saturation magnetization and the scaled specific heat gives a values between 3.4 and 9.9 meV per atom.

At lower temperatures, 50 K$\leq T \leq$100 K, the magnetization gives rise to a pronounced peak while the magnon heat capacity shows only a broad shoulder. Such discrepancy attracts a special attention to this temperature region.

2.4.2 Onset of non-collinear magnetic structure: spin-reorientation transition

The temperature-dependent magnetization (Fig. 2.9, (a)) shows a step between 100 K and 50 K, which has a field-dependent origin: it is more pronounced in

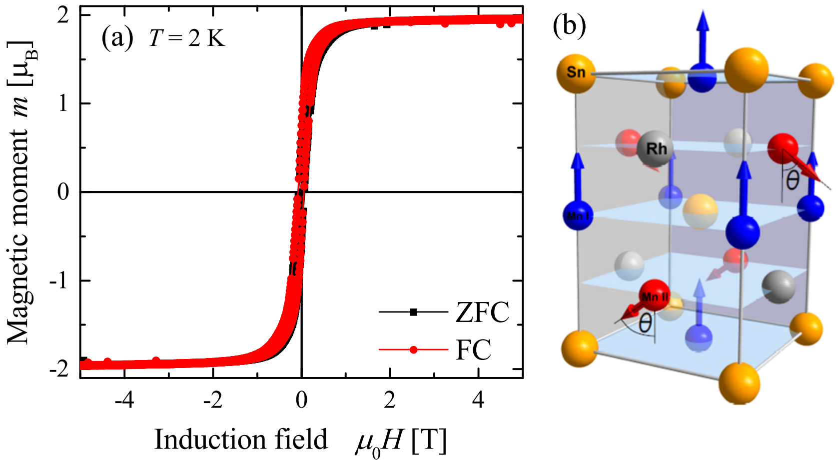

Figure 2.10: (a) Zero-field cooled (ZFC) and field-cooled (FC) magnetic hysteresis loop of Mn_2RhSn. (b) Magnetic structure of Mn_2RhSn is represented by two antiparallel Mn sublattices, where the Mn_{II}-sublattice is deviated from the z-axis by a canting angle θ.

weaker fields (but larger than the coercive field $\mu_0 B > H_C$) of 0.1 T, reduces by an increased field of 0.5 T and smears in strong fields ~5 T, where the magnetic structure is fully saturated and no spin-texture can exist. The transition is even stronger pronounced on the ac-susceptibility data (Fig. 2.9, (b)). Independent from the frequency, a sharp jump is observed around 80 K. The ac-susceptibility experiments support the presence of the magnetic transition, suggest a long-range magnetic order of the material and exclude the spin-glass behavior: there is no evident shift of the transition temperature with the frequency. Naturally, the magnetic transition in a Heusler compound implicates a simultaneous investigation of the crystal structure due to the possible magneto-structural phenomena [153, 154]. The high-resolution synchrotron X-ray analysis showed however no change of the crystal symmetry above or below the transition (see Fig. 2.5).

The temperature-dependent evolution of the magnetic structure can be comprehensively analyzed by the neutron scattering experiments. Both magnetic and nuclear structure have been studied by polarized elastic neutron scattering in zero field at the Laboratorie Léon Brillouin (LLB), CEA France. Two-axis diffractometer equipped with a vertical focusing pyrolytic graphite monochromator and a cold neutron guide was used for the measurement. The sample was encapsulated in a vanadium crucible and its environment was was kept constant within the whole temperature range from 1.8 to 299 K. The wavelength of incoming neutrons was 2.422 Å. Similar to the the XRD procedure, the powder has been sieved. The recorded patterns were processed according to the Rietveld method using FullProf [151] software. First, a nuclear phase was optimized at 299 K, which is above the magnetic ordering temperature of 270 K; the obtained parameters were later used for the refinement of magnetic phase. The background was modeled by interpolation between selected points. The peak shape profile was described by the pseudo-Voigt function with a refined ratio between Gaussian and Lorentzian contributions. The magnetic scattering form factors were used different for Mn_{I} and Mn_{II} as of different oxidation states: 3+ and 2+ respectively.

The paramagnetic room temperature measurement contains only the crystal structure information. Instead, the diffraction pattern recorded at 1.8 K represents both structural and magnetic signal (see Fig. 2.11). The latter can be well analyzed due to its 65% contribution to the overall intensity. Here, the magnetic phase mainly resides in the (101), (002) and (110) reflexes. Since the the Bragg and magnetic peaks coincide by their positions, first, the room temperature pattern was thoroughly refined to fix some of the crystal parameters and avoid influencing on the magnetic interpretation. An additional intensity contains only that magnetic component, which is perpendicular to the scattering vector k. Therefore, neutrons reflected from the (101), (002) and (110) crystal planes give an estimate how the magnetic moment evolves within the corresponding planes.

Magnetic structure of Mn_2RhSn is represented by two Mn sublattices: Mn_{I} at $2b$ $(0, 1/2, 0)$ and Mn_{II} at $2d$ $(0, 1/2, 3/4)$ Wyckoff sites. As typical for the Mn_2-based Heusler family, the Mn_2RhSn is expected to show a ferrimagnetic alignment of its sublattices, which is indeed observed from 270 K down to 80 K. An antiparallel orientation of the sublattices is also suggested by the saturation magnetization (see Fig. 2.10) of 1.97 μ_{B} at 2 K (Mn_{I} moment by itself can vary from 3 μ_{B} to 4.5 μ_{B} depending on an environment; the ferromagnetic arrangement would result ≥ 3 μ_{B}). At the temperature below 80 K, an in-plane magnetism starts to rapidly evolve (see Fig. 2.11, (right inset)). This is associated with the deviation of the Mn_{II} moment from its crystallographic z axis, while the moment of Mn_{I} is strongly localized and stays firmly aligned along the z direction. Development of the in-plane magnetism is accompanied by the simultaneous suppression of the z-component of Mn_{I} down to nearly 1 μ_{B}, while the z-component of Mn_{I} evolves rather insignificantly. The in-plane magnetism is realized by the gradual spin reorientation of the Mn_{II} sublattice. It is not only the mutual orientation of the site-specific moments that changes but their absolute values also change (Fig. 2.12, (c)). As the tempera-

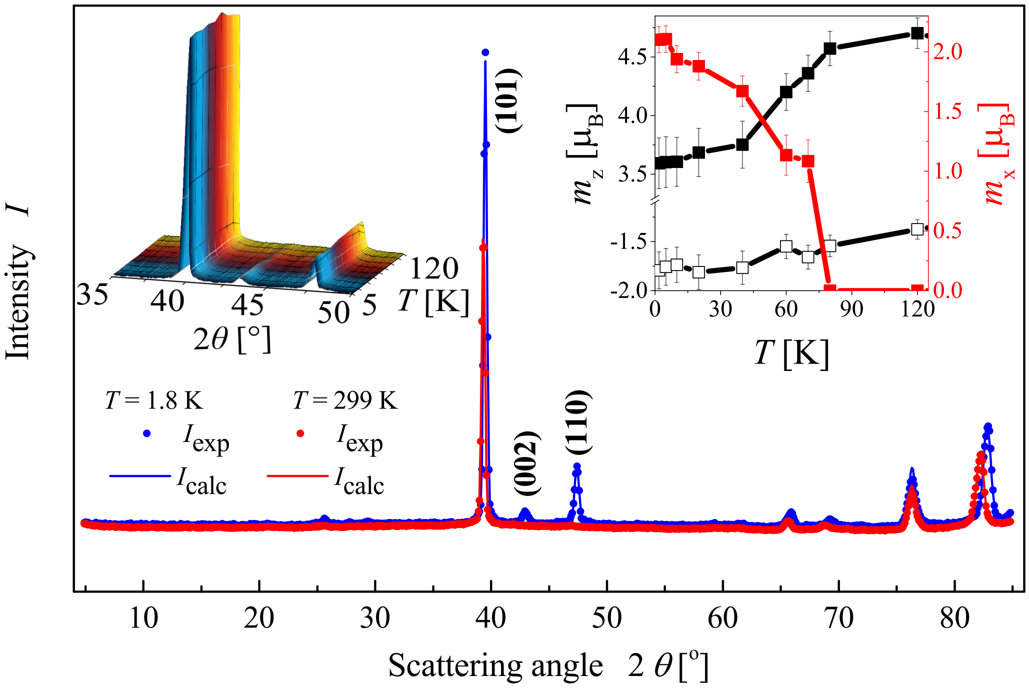

Figure 2.11: Elastic powder neutron scattering patterns obtained at 299 K (red) and 1.8 K (blue) using the wavelength of $\lambda = 2.422$ Å. No external magnetic field was applied. Main magnetic intensity is added to the (101), (002) and (110) peaks. Left inset: temperature-dependent neutron spectra, at the temperatures below 80 K the (002) peak gradually increases. Right inset: development of the in-plane magnetism (produced by $\mathrm{Mn_{II}}$ xy-component, closed red marks) suppresses the z-component of $\mathrm{Mn_I}$ (closed black marks), while the z-component of $\mathrm{Mn_I}$ evolves rather insignificantly (open black marks).

ture decreases, the $\mathrm{Mn_{II}}$ moments become larger and suppress the $\mathrm{Mn_I}$ from 4.5 to 3.5 μ_B. This occurs gradually, and the slope of the zero-field heat capacity curve changes (Fig. 2.12, (e)); the spin-wave term is sufficiently weak in comparison to the electronic and phonon contributions that no sharp anomaly is visible. However, the onset of the FiM phase is characterized by the explicit step-like increase in the ac-susceptibility signal (Fig. 2.12, (b)). Measured values of χ' and χ'' were found to be independent on frequency, suggesting a high magnetic homogeneity. The evolution of the magnetism with temperature is echoed by the crystal structure (Fig. 2.12, (f)). Although the a-parameter decreases monotonically, the change in c-parameter is non-linear and resembles the ac-susceptibility behavior; the anomaly is observed around the T_C and gradual non-linear curvature depicts the gradual spin reorientation between 100 and 50 K. The c-parameter is more sensitive to the magnetic changes than the a-parameter, due to the fact that tetragonal distortion itself is a result of certain magnetic/electronic instabilities. In the following we will discuss the ground state magnetic structure.

2.4.3 Ground state magnetism: experiment and theory

Neutron scattering pattern, obtained at the lowest possible temperature of $T = 1.8$ K, reveals a canted ferrimagnetic structure with $\theta = (59 \pm 5)^\circ$ and the moments of 3.59 μ_B and 3.47 μ_B on $\mathrm{Mn_I}$ and $\mathrm{Mn_{II}}$ respectively. Such magnetic arrangement correlates with the hysteresis loop obtained at the same temperature, which reveals the total magnetic moment of 1.97 μ_B (see Fig. 2.10, (a)). It is important to stress, that the θ is an identical polar angle here, while the azimuthal angle ϕ is free to change from 0 to 2π.

The magnetic order of $\mathrm{Mn_2RhSn}$ was found from the first-principles calculations using the spin-polarized relativistic Korringa–Kohn–Rostoker (SPR-KKR) Green's function method [155] within a local density approximation [156]. The experimentally obtained lattice parameters were used; a self-consistent determination of local moments including their amplitudes, directions and periodicity was allowed.

In a non-relativistic case, the magnetic non-collinearity is a result of the competition between antiparallel and parallel exchange interactions (or between several types of antiparallel interactions). Such a situation is often encountered in $\mathrm{Mn_2YZ}$ compounds, but not all of them exhibit non-collinearity. In general, these materials crystallize in the non-centrosymmetric $I\bar{4}m2$ structure with two non-equivalent Wyckoff positions occupied by Mn atoms: $\mathrm{Mn_I}$ at $2b$ (0, 1/2, 0) and $\mathrm{Mn_{II}}$ at $2d$ (0, 1/2, 3/4). Z and Y elements occupy the $2a$ (0, 0, 0) and $2c$ (0, 1/2, 1/4) positions,

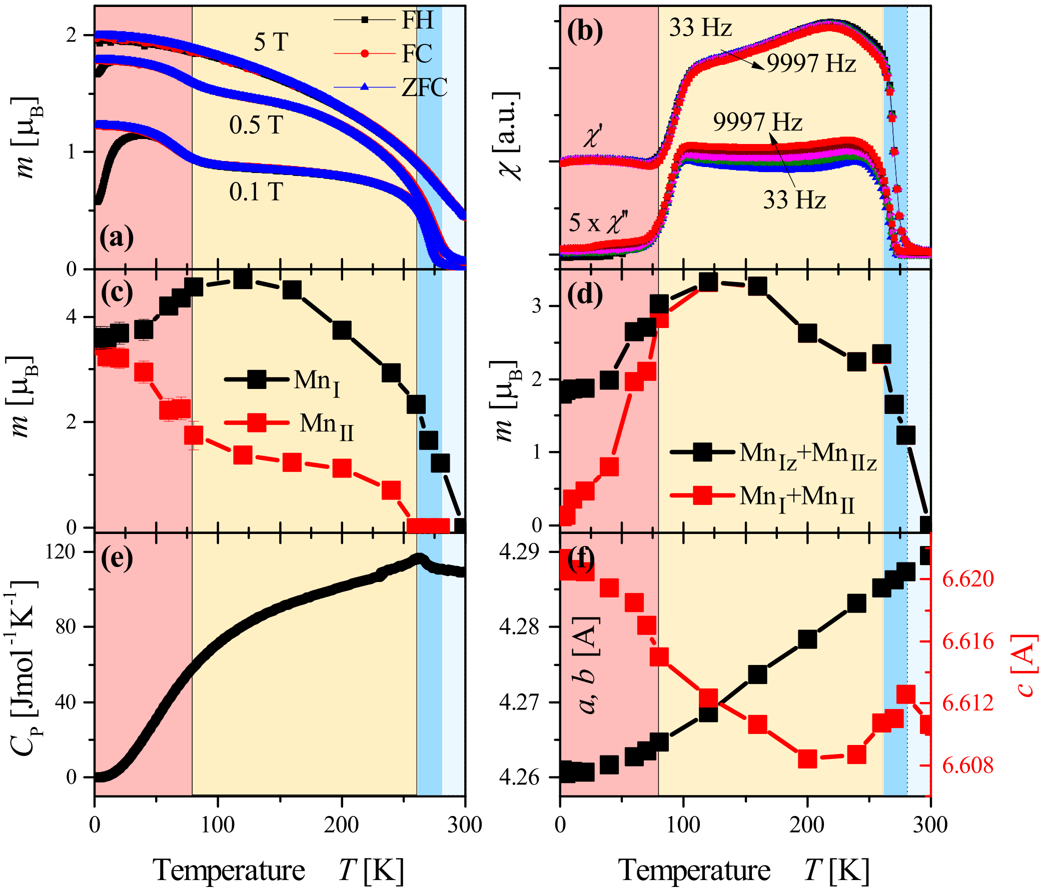

Figure 2.12: (a) Evolution of the magnetic structure with the temperature. Canted (red), collinear ferrimagnetic (yellow) and disordered (blue) magnetic states of $\mathrm{Mn_2RhSn}$. (a) Zero-field-cooled (ZFC), field-cooled (FC) and field-heated (FH) magnetization as a function of the temperature measured at induction fields of 0.1, 0.5, and 5 T. (b) Real (χ') and imaginary (χ'') ac-susceptibility components are frequency independent and show a pronounced step at the onset of the FiM phase. (c) The increase of the canting angle occurs because of the simultaneous re-alignment of the $\mathrm{Mn_{II}}$ moment and an increase in its absolute value. This, in turn, suppresses the $\mathrm{Mn_{I}}$ moment from 4.5 to 3.5 μ_B. (d) The sum of the total and z-components of the $\mathrm{Mn_{I(II)}}$ moments follows the ac-susceptibility behavior. No in-plane component is present below 80 K. (e) A change in the slope of the heat capacity curve is observed in the vicinity of the spin-reorientation. (f) Evolution of the lattice parameters with temperature: the change in the magnetism is echoed mainly by the c-parameter, while a evolves monotonically.

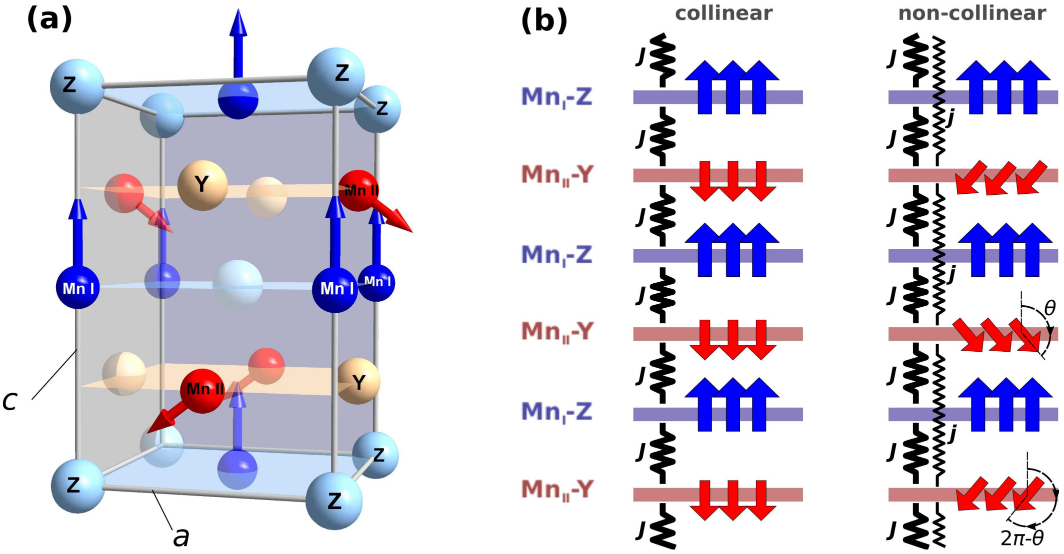

Figure 2.13: (a) Crystal and magnetic structures of Mn_2YZ Heusler compounds. Due to the magneto-crystalline anisotropy induced by the tetragonal distortion, the Mn_I magnetic moments are oriented along the c axis; the moments on Mn_{II} are canted in an alternating manner with respect to the c axis. (b) Schematic picture of the leading magnetic exchange interactions between different atomic layers in Mn_2YZ (atomic planes containing Z and Y elements are shown in blue and red, respectively). The arrows show the orientation of the spin moments on Mn and the springs show the exchange interactions between different planes. Considering only the nearest antiparallel interactions J (between Mn_I-Z and Mn_{II}-Y planes) leaves the magnetic structure collinear; introducing the next-nearest antiparallel coupling j (between Mn_{II}-Y planes) leads to the alternating canting of Mn_{II} moments by θ and $2\pi - \theta$.

respectively (Fig. 2.13 a).

The most significant exchange coupling between the nearest Mn_I and Mn_{II} atoms is characterized by a large exchange constant ($J_{Mn_I - Mn_{II}} \sim -20$ meV) (e.g. [157]) that leads to a typical collinear FiM (ferrimagnetic) state. Despite the fact that the in-plane interaction of Mn atoms can be rather complicated (e.g. the nearest in-plane neighbors couple parallel, the next-nearest couple antiparallel or parallel, and so on), these interactions are rather weak compared to $J_{Mn_I - Mn_{II}}$, which always aligns the Mn spin moments of the same plane parallel to one another (Fig. 2.13 b). For this reason, we initially do not consider the in-plane interactions but will expand the description in terms of the effective *inter-plane* exchange coupling J, which indicates the interaction of a certain Mn atom (i) with all other Mn atoms (i') in a different plane, i.e. $J = \sum_{i'} J_{ii'}$.

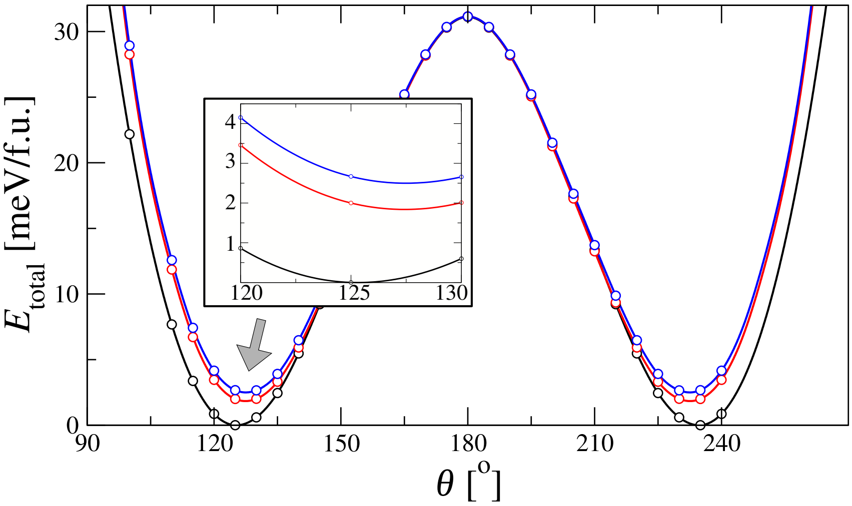

Figure 2.14: Total energy per Mn_2RhSn formula unit computed as a function of the orientation of the Mn_{II} magnetic moment characterized by angle θ. We compare three magnetic orientations: black - total magnetization is along the c-axis; blue and red - total magnetization within ab-plane, but with Mn_{II}-moments staggering within ab and within ac-planes, respectively. Inset shows the detailed energy trends near to the canting minimum at about 125°.

Since the collinear order being substantially determined by the nearest-plane J interaction becomes even more stable if the Y atom is magnetic (as e. g. in case of Mn_2CoZ systems [157]), our further consideration concerns Mn_2YZ Heusler materials with the non-magnetic heavy Y elements (such as Rh or Ir, since in case of light elements, such as Ti or V, Mn atoms occupy equivalent 2c and 2d positions). In this case, the collinearity can be perturbed by the next important interaction j between the next-nearest planes, e.g. between pairs of Mn_{II}-Y planes as shown in Fig. 2.13 b. This interaction is antiparallel due to its indirect origin realized through the main-group element Z (super-exchange) [158]. Since j tends to rotate the moments of the nearest Mn_{II}-Y planes antiparallel to each other, it competes with the strong antiparallel exchange J, and may then result in a non-trivial canting angle ($\theta \neq 0°, 180°$, Fig. 2.13 b). The relevant θ-dependent part of the Heisenberg

Mn_2YZ	m_{Mn_I}	$m_{Mn_{II}}$	$\theta_{1,2}[^\circ]$	m_Y	M	M_{exp}
Mn_2RhSn	3.51	3.08	180 ± 55	0.14	1.9	1.97

Table 2.2: Computed atomic magnetic moments m, canting angle $\theta_{1,2}$ and total magnetization per formula unit $M = m_{Mn_I} + m_{Mn_{II}} \cdot \cos\theta + m_Y$, compared to the experimentally measured magnetization M_{exp}. Values of magnetic moments/magnetization are given in μ_B.

Hamiltonian will contain only antiparallel interactions:

$$H_\theta = -J\cos\theta - {}^1\!/\!_2 \cdot j\cos 2(\pi - \theta)\,, \tag{2.4}$$

where the first term is the coupling of the nearest planes (Mn_I-Z with Mn_{II}-Y) and the second is that of the next-nearest (Mn_{II}-Y) planes. The factor 1/2 accounts for the twice sparser entrance of the next-nearest plane couplings. The extrema of H_θ are found from:

$$\sin\theta\left({}^1\!/\!_2 + \frac{j}{J}\cos\theta\right) = 0\,, \tag{2.5}$$

and $\theta_{1,2} = 180^\circ \pm \arccos\left(\frac{J}{2j}\right)$ non-collinear solutions are given subject to the condition $j/J > {}^1\!/\!_2$, which means that the canting occurs only if the next-nearest antiparallel exchange j is sufficiently strong.

The plot of the total energy as a function of θ indeed exhibits two energy minima corresponding to the non-trivial canting angles $\theta_{1,2} = 180^\circ \pm 55^\circ$. Calculated local moments, their orientations, total magnetization, and experimentally measured one, are summarized in Tab. 2.2.

From the θ-dependent total energy the canting angle $\theta_{1,2} = 180^\circ \pm 55^\circ$ is inferred. The difference between a FM and a FiM configurations is ~0.67 eV, which is perturbed by the canting of about 0.06 eV energy gain.

To prove the proposed mechanism, the exchange coupling constants were computed (using the approach in Ref. [159]) for the model Eq.2.4 directly minimizing the Heisenberg Hamiltonian. The obtained values of ($J = -63.46$ and $j = -53.05$ meV) satisfy criterion: $j/J = 0.83 > {}^1\!/\!_2$. This then leads to $\theta_{1,2} = 180^\circ \pm 53.3^\circ$, which is in reasonable agreement with the *ab-initio* calculated value in Tab. 2.2.

In order to analyze the possible long-range magnetic orders, and in particular, the possibility of skyrmions in Mn_2RhSn, the absolute values of the Dzyaloshinskii-

Moriya (DM) vectors were computed by following the scheme introduced in Ref. [160]. In addition the magneto-crystalline anisotropy was computed as the energy difference between orientations of the total magnetization along the *c*-axis and within *ab*-plane. Due to canting, for the second case two orientations are separated - first, when $\mathrm{Mn_{II}}$ moments stagger within *ab*-plane and second - within *ac*-plane (see Fig. 2.14).

As it follows from the inset, the energy minima for the *ab*-orientations are shifted by few degrees. Their absolute values are about 2.5 (staggering within *ab*-plane) and 1.8 meV/f.u. (staggering within *ac*-plane).

2.4.4 Continuum model of magnetic order in $\mathrm{Mn_2RhSn}$

Despite of the rich physical phenomena, magnetic orders in Heusler compounds are rather simple. Currently presented result is pioneering in this family of materials. The observed non-collinearity, presence of two magnetic transitions, non-centrosymmetric crystal structure and a large spin-orbit coupling imply a discussion of a possible skyrmion state. Experimentally, such studies require certain efforts: single crystal samples for the small-angle neutron scattering or Lorentz - transmission electron microscopy (TEM) investigations with a pinpoint accuracy. Nevertheless, a phenomenological continuum theory together with the obtained Landau-Ginzburg functional suggest the possibility of a skyrmion state in $\mathrm{Mn_2RhSn}$ and other related $\mathrm{Mn_2}$-based Heusler materials.

The phenomenological continuum theory for the magnetism of $\mathrm{Mn_2RhSn}$ can be written in terms of the four sublattices ($l = 1, 2, 3, 4$) consisting of the two sublattices $\mathrm{Mn_{I}}$ on Wyckoff site $2a$ and $\mathrm{Mn_{II}}$ on site $2c$. Standard methods have been used to derive a quantitative model in the shape of this phenomenological theory by a systematic coarse-graining of a microscopic model, where direct and antisymmetric DM exchange are calculated with DFT methods. Eventually, by adding magnetic anisotropies, also from DFT calculations and Zeeman energy, a micromagnetic low-temperature continuum model can be constructed. For the thermal phase diagram, empirical input is needed to write a Landau-Ginzburg functional for coupled magnetic modes.

As the low acentric symmetry of $\mathrm{Mn_2RhSn}$ allows for the presence of chiral inhomogeneous DM couplings, the resulting model has the form of a Dzyaloshinskii-model [47] marked by the presence of Lifshitz-type invariants that couple different magnetic order parameters. This coarse-grained continuum theory for the ground-state can be derived from the microscopic classical Hamiltonian of the lattice and symmetry constraints. Using the results of the *ab-initio* calculations, the magnetic energy can be expressed by a model including direct (isotropic) Heisenberg-like exchange couplings and the DM-couplings. It must be noted that there is no weak ferromagnetism or weak antiferromagnetism in the tetragonal inverse Heusler structure, i.e., there are no bilinear coupling terms between components of the staggered and ferromagnetic vectors derived from the DM-exchange, because the four sublattices are related by non-primitive translations.

After quantification of the exchange couplings terms, it is convenient to analyze the 4-sublattice system by using staggered and ferromagnetic vectors of two sublattices,

$$\begin{aligned} m_{\mathrm{Mn_I}}\cdot\mathbf{L} &= \frac{(\mathbf{m}_1-\mathbf{m}_3)}{2}; \quad m_{\mathrm{Mn_I}}\cdot\mathbf{F} = \frac{(\mathbf{m}_1+\mathbf{m}_3)}{2}; \\ m_{\mathrm{Mn_{II}}}\cdot\mathbf{l} &= \frac{(\mathbf{m}_2-\mathbf{m}_4)}{2}; \quad m_{\mathrm{Mn_{II}}}\cdot\mathbf{f} = \frac{(\mathbf{m}_2+\mathbf{m}_4)}{2}, \end{aligned} \tag{2.6}$$

where the spin vectors **L** and **F** are related to $\mathrm{Mn_I}$, and **l** and **f** – to $\mathrm{Mn_{II}}$ sublattice.

In the ground-state configurations, these vectors fulfill

$$\begin{aligned} \mathbf{L}^2+\mathbf{F}^2 &= 1; \qquad \mathbf{L}\cdot\mathbf{F}=0 \\ \mathbf{l}^2+\mathbf{f}^2 &= 1; \qquad \mathbf{l}\cdot\mathbf{f}=0\,. \end{aligned} \tag{2.7}$$

Dropping irrelevant terms, the homogeneous part of the continuum theory is expressed as

$$\begin{aligned} \tilde{w}_0 = {} & J_F\mathbf{F}\cdot\mathbf{F} + J_L\mathbf{L}\cdot\mathbf{L} + J_f\mathbf{f}\cdot\mathbf{f} + J_l\mathbf{l}\cdot\mathbf{l} \\ + {} & J_c\mathbf{F}\cdot\mathbf{f} + J'\mathbf{F}\cdot\mathbf{l} - 2(m_{\mathrm{Mn_I}}\cdot\mathbf{F} + m_{\mathrm{Mn_{II}}}\cdot\mathbf{f})\cdot\mathbf{H}\,. \end{aligned} \tag{2.8}$$

Here the notation is used for the effective exchange, internal to the ordering modes and between the modes, and using the spin moments from the DFT calculations $m_{\mathrm{Mn_{I(II)}}} = 3.51\ (3.08)\ \mu_{\mathrm{B}}$. The field **H** in (2.8) is the internal magnetic field.

The exchange couplings have a clear hierarchy, showing that magnetic ordering is either dominated by the FM order on $\mathrm{Mn_I}$ sublattice or by staggered AFM order on $\mathrm{Mn_{II}}$. This AFM order is only very weakly coupled via the staggered vectors **L**, which however is not the dominating magnetic mode on $\mathrm{Mn_I}$ sublattice. Hence, $\mathrm{Mn_2RhSn}$ is close to a tetracritical (or bicritical) point, where these two magnetic modes would coexist with the paramagnetic state. The FM mode **f** is a secondary magnetic order for sublattice $\mathrm{Mn_{II}}$, which is *antiparallel* to **F** via the very strong coupling J_c. The superposition of $\mathbf{F}$, $\mathbf{l}$ and $\mathbf{f}$ determines a canted state for the magnetic order with the magnetic cell equivalent to the crystallographic unit cell.

Ground state

The homogeneous ground state can be found by writing a coplanar canted state arbitrarily in the *ac*-plane, using $\mathbf{F} \equiv \mathbf{F}_0 = (0, 0, 1)$, $\mathbf{l} \equiv \mathbf{l}_0 = (\sin[\pi - \vartheta], 0, 0)$, and $\mathbf{f} \equiv \mathbf{f} = (0, 0, \cos[\pi - \vartheta])$. Its energy is given by

$$w_0 = J_F + J_l + (J_f - J_l)\,\xi^2 + J_c\xi; \quad \xi = \cos[\pi - \vartheta]\,. \tag{2.9}$$

The solution for the canting angle is

$$\vartheta = \pi - \arccos \frac{J_c}{2(J_f - J_l)}\,. \tag{2.10}$$

Using the parameters above, the canting angle is $\vartheta_0 = 64.2°$, which is in reasonable agreement with the *ab-initio* calculations finding $\theta_{1,2} = 55°$, considering that the exchange approximation in Eq. (2.8) neglects the anisotropy which has an easy-axis character for the canted sublattice $\mathrm{Mn_{II}}$ (see Fig. 2.14).

The ground state, thus, is composed of the two modes $\mathbf{F}$ and $\mathbf{l}$, which are almost decoupled for $J' \simeq 0$, and by the induced FM mode $\mathbf{f}$ on $\mathrm{Mn_{II}}$. However, the conditions (2.7) provide a non-linear coupling between these different modes in a proper micromagnetic model.

Inhomogeneous states

The micromagnetic model requires now to include the exchange terms and the inhomogeneous DM-couplings, i.e., the gradient energy is given by

$$w_2 = w_J + w_D. \tag{2.11}$$

An inhomogeneous modification of the ground-state takes place on long lengths, owing to the weakness of the DM-exchange compared to the direct exchange. Considering that the DM-couplings and also applied magnetic fields and anisotropies are small in comparison to the strong local exchange forces, the basic canted structure is preserved in each unit cell. But it can be slowly rotated over length of many unit cells.

Landau-Ginzburg functional

In order to complete the phenomenological theory, the form of an appropriate Landau-Ginzburg functional is discussed, which could be used to model the thermal phase diagram and the phase transitions. The two primary order parameters (OPs) are the FiM and the AFM modes, $\mathbf{F}$ and $\mathbf{l}$. They and the coupling between them have to be considered with respect to the secondary OP, which is the FM mode $\mathbf{f}$.

The complete Landau-Ginzburg (LG) functional for the magnetic free energy then is given by

$$w_{LG} = w_0 + w_J + w_D + w_a \,, \tag{2.12}$$

where w_0 is a ground state magnetic free energy, w_J described the isotropic exchange, w_D is the energy term of inhomogeneous DM couplings and the w_a collects anisotropic contributions, not contained in the first three terms, i.e., the magnetocrystalline and exchange anisotropies.

A complete microscopic derivation of the terms in the LG-functional would require a detailed finite temperature statistical theory beyond the input from the DFT-calculations for ground-states. And, for the behavior at lower temperatures, the higher-order-terms (h.o.t.'s) are required in the thermodynamic potential. However, a semi-quantitative model could be written in the usual manner by restricting the temperature dependence of the model to the coefficients of the square terms in the primary OPs:

$$\begin{aligned} a_F(T) &= \alpha_F \, (T - T_C^0) \\ a_l(T) &= \alpha_l \, (T - T_N^0) \end{aligned} \tag{2.13}$$

In Mn_2RhSn the bare FiM Curie temperature $T_C^0 \sim 270$ K $< T_C$, and the $T_N^0 \sim 80$ K, i.e. close to the onset of the AFM mode on Mn_{II}-sublattice. Here it is to point out that the suppression of the FM mode $\mathbf{F}$ on Mn_I-sublattice below the onset of the AFM signals leads to the competition of the FiM and AFM modes and as a result to the formation of inhomogeneous textures.

Skyrmions in the ferrimagnetic state

The qualitative discussion of the LG-functional is sufficient to understand the basic features of inhomogeneous state in the intermediate temperature range $T_N^0 < T < T_C$ where only the FiM collinear state exists. In that case, the FM mode on the $\mathrm{Mn_{II}}$-sublattice is antiparallel to FM mode on the $\mathrm{Mn_{I}}$-sublattice, $\mathbf{f} = -\mathbf{F}$. Considering also the Zeeman term an magneto-crystalline uniaxial anisotropy, yields inhomogeneous FiM states in the *ab*-plane:

$$\begin{aligned}\tilde{w}_{\mathrm{FiM}} = &\tilde{A}[\partial_a\mathbf{F}\cdot\partial_a\mathbf{F} + \partial_b\mathbf{F}\cdot\partial_b\mathbf{F}] + \tilde{D}[F^c\bar{\partial}_b F^a + F^c\bar{\partial}_a F^b] \\ &- 2\,(m_{\mathrm{Mn_I}} - m_{\mathrm{Mn_{II}}})\,\mathbf{F}\cdot\mathbf{H} - K\,(F^c)^2\,.\end{aligned} \tag{2.14}$$

These states are exactly equivalent to the FM Dzyaloshinskii-model for chiral magnets from crystal class $\overline{4}2m$ studied earlier [81, 124]. In particular, the solutions for isolated and condensed chiral 'vortices' and the magnetic phase diagram presented in this pioneering work describe what is now known as chiral skyrmions in the FiM state of acentric $\mathrm{Mn_2YZ}$ inverse tetragonal Heusler alloys.

The parameters of this model for $\mathrm{Mn_2RhSn}$ can be calculated as $\tilde{A} = A_F + A_f - 2\,A_{Ff} = 16.5$ meV$/a^2$ and $\tilde{D} = D_F + D_f - D_c = 7.0$ meV$/a$. The DFT calculations of anisotropy suggest an effective easy-axis anisotropy of the order $K \simeq 2$ meV/f.u. It is assumed that the magnetic coupling coefficients do not depend strongly on temperature, i. e., their temperature dependence should essentially scale only with the square of the saturation magnetization. This means that all the ratios of coupling terms in the free energy Eq. (2.14) are almost constant with temperature. Then, we may use the coefficients from the microscopic ground-state calculation to estimate materials parameters of $\mathrm{Mn_2RhSn}$ at elevated temperatures and evaluate the sizes or stability of skyrmions and the phase diagram in $\mathrm{Mn_2RhSn}$ in the FiM state. The chiral magnetic twisting lengths is given by

$$\Lambda = 4\pi\,\tilde{A}/\tilde{D}, \tag{2.15}$$

which means $\Lambda \sim 29.5\ a \sim 130$ nm for $\mathrm{Mn_2RhSn}$. The strengths of the easy-axis anisotropy determines whether a modulated spiral ground-state exists and whether a field-induced skyrmion lattice in an effective field pointing along the *c*-axis occurs (see Figs. 9 and 10 in Ref. [124]).

The different cases can be distinguished by the parameter

$$\kappa = \pi\,\tilde{D}/4\,\sqrt{\tilde{A}\,K}\,. \tag{2.16}$$

For $\kappa < 1$, the ground state is collinear as the strong anisotropy suppresses the spiral state. For $\kappa > 1.14$, there is a field-induced skyrmion lattice in the magnetic equilibrium phase diagram for fields along c.

For the estimated coefficients, $\kappa \simeq 0.95$ has a reasonable value for Mn_2RhSn but close to the critical κ.

The spiral magnetic states in crystals with $\overline{4}2m$ crystals can have demagnetizing fields, as they are of cycloidal (Néel)-like character when propagating along (110)-directions, while they are of helical (Bloch)-like character for propagation along (100)-directions. The demagnetizing field further reduces the effective κ and oblique/skew spirals for propagation directions in between, as discussed in Ref. [124]. Hence, the quantitative estimates for the micromagnetic model $\tilde{w}_{\mathrm{FiM}}$ suggest a collinear FiM state in Mn_2RhSn. The solutions for isolated chiral skyrmions with a single FM ordering mode have been presented in Ref. [124] for the basic model Eqs. (2.14).

The shape of an isolated skyrmion in Mn_2RhSn is sketched in Fig. 2.15. Close to the reorientation transition, where the AFM ordering sets in, the magnitude of the $\mathbf{l}$-mode is small and can be modulated ($|\mathbf{l}| \neq$const). As long this mode is subjugated to the FiM order it remains perpendicular to the $\mathbf{F}$-mode. Owing to its softness, it will not only rotate in a manner, so as to minimize the energy of its Lifshitz-invariants, it also will be modulated with a zero, $\mathbf{l} = 0$, in the center in form of a vortex-like defect.

In Mn_2RhSn, the coefficients $\tilde{D}$ and D_l have similar magnitude and the same sign, so that the screw-sense of the rotation of $\mathbf{F}$ and $\mathbf{l}$ are not in conflict. Hence, close to T_N^0 the $\mathbf{l}$-mode follows and co-rotates the FiM mode $\mathbf{F}$ while being modulated in lengths, Fig. 2.15 (c, d). At lower temperatures, the necessity to have a defect of the $\mathbf{l}$-mode in the skyrmion center and the associated large defect-energy most likely will destabilize the skyrmions. However, there may exist other localized solitonic textures in this acentric coupled magnetic system, which may cause inhomogeneous magnetic states to exist in the acentric Mn_2YZ alloys.

2.5 Chemical and structural phase stability of Mn_2RhSn

Since Heusler compounds are known to be amenable first of all to chemical disorder, a phase stability is indeed a vital aspect to be discussed. For example, in the present case, the magnetic state would be severely influenced by any type of antisite disorder.

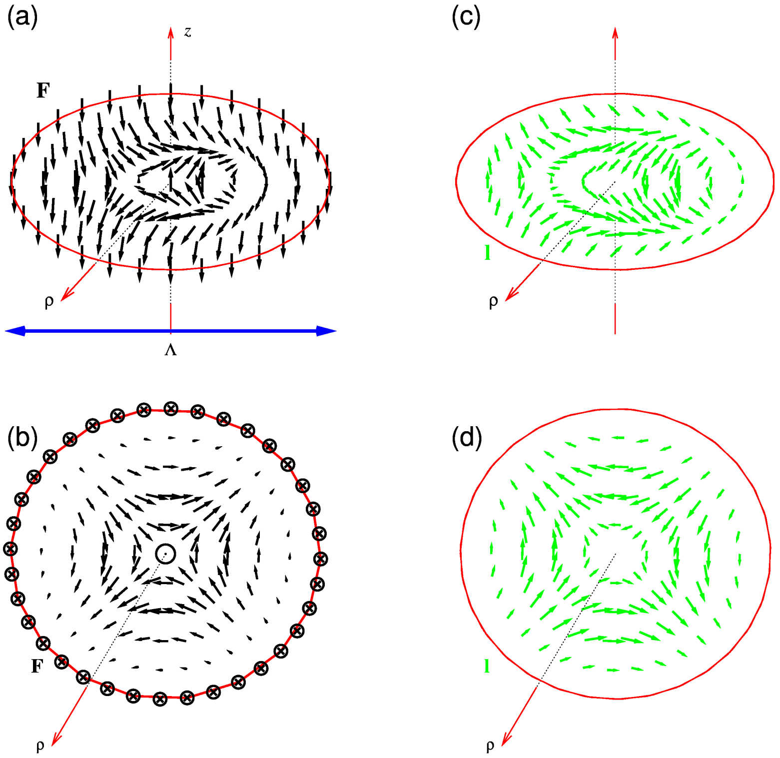

Figure 2.15: (a) Shape of the double-twisted skyrmion configuration in the tetragonal inverse Heusler alloys of $\bar{4}2m$ symmetry. The FM magnetization $\mathbf{F}$ on sublattice Mn$_{\text{I}}$ parametrizes the FiM collinear state at higher temperatures in Mn$_2$RhSn. The corresponding magnetization $\mathbf{f}$ on sublattice Mn$_{\text{II}}$ is strictly antiparallel to $\mathbf{F}$. (b) Projection of the skyrmion in the *ab*-plane. (c) Close to the reorientation transition, the AFM mode $\mathbf{l}$ on Mn$_{\text{II}}$-sublattice sets in: $|\mathbf{l}| \ll |\mathbf{F}|$ and also $|\mathbf{l}| \ll |\mathbf{f}|$. $\mathbf{l}$ is perpendicular to $\mathbf{F}$ and rotates with it in the same plane in each radial direction. In the center $|\mathbf{l}| = 0$. (d) Projection of $\mathbf{l}$ onto *ab*-plane.

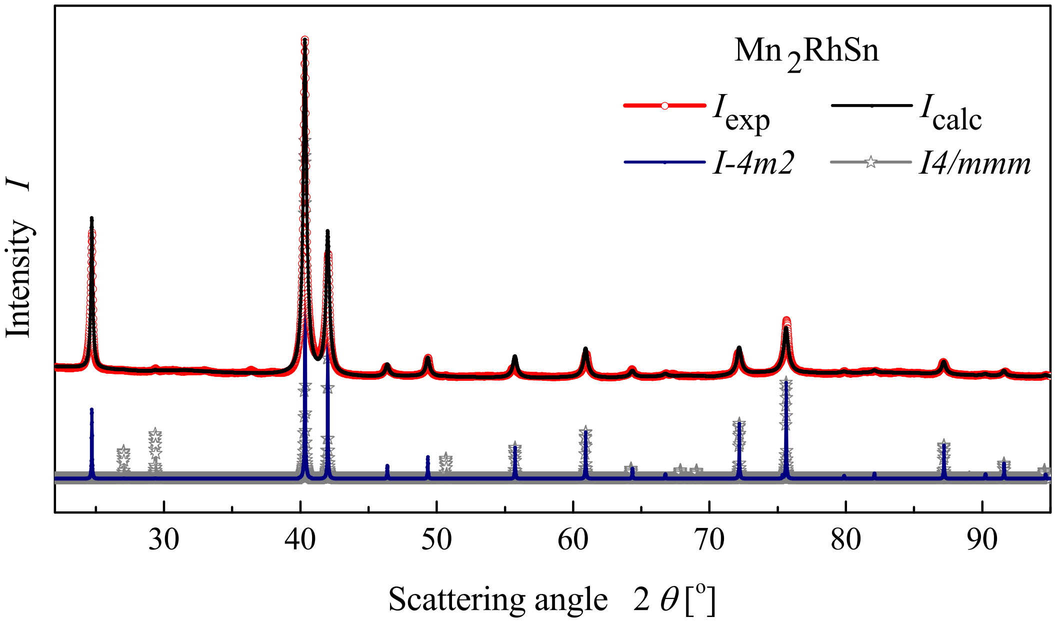

Figure 2.16: XRD powder pattern of Mn_2RhSn. The measured pattern has been refined using the $I\bar{4}m2$ non-centrosymmetric tetragonal Heusler structure as a model (119 symmetry type). For comparison, the 119 and 139 structures are showed below (blue and grey respectively), which differ by the presence of inversion center and Mn-Rh disorder.

Random exchange between Rh and Mn_I would increase the amount of Mn_{II} type (magnetically antiparallel to Mn_I). In turn, the exchange between Sn and Mn_{II} will increase the amount of Mn_I type. The exchange between Rh and Sn will locally convert Mn_I into Mn_{II} within Mn_I-Sn planes, and Mn_{II} into Mn_I - within Mn_{II}-Rh planes. In which way particular type of disorder will affect the system exactly, is rather a complicated question, as it implies not just a straightforward redistribution of different Mn types, but the change of the whole magnetic coupling picture. One can show (e. g., by first-principle calculations) that in all cases the total energy drastically increases, which indicates that such events are of small probability (once the system holds the correct stoichiometry and is properly annealed). In any case, if such situation would occur, the interpretation of the neutron spectra using the proposed magnetic picture would be unreliable.

As for the present samples, such straightforward reason for chemical disorder as deviation between the actual and the target compositions can be excluded due to

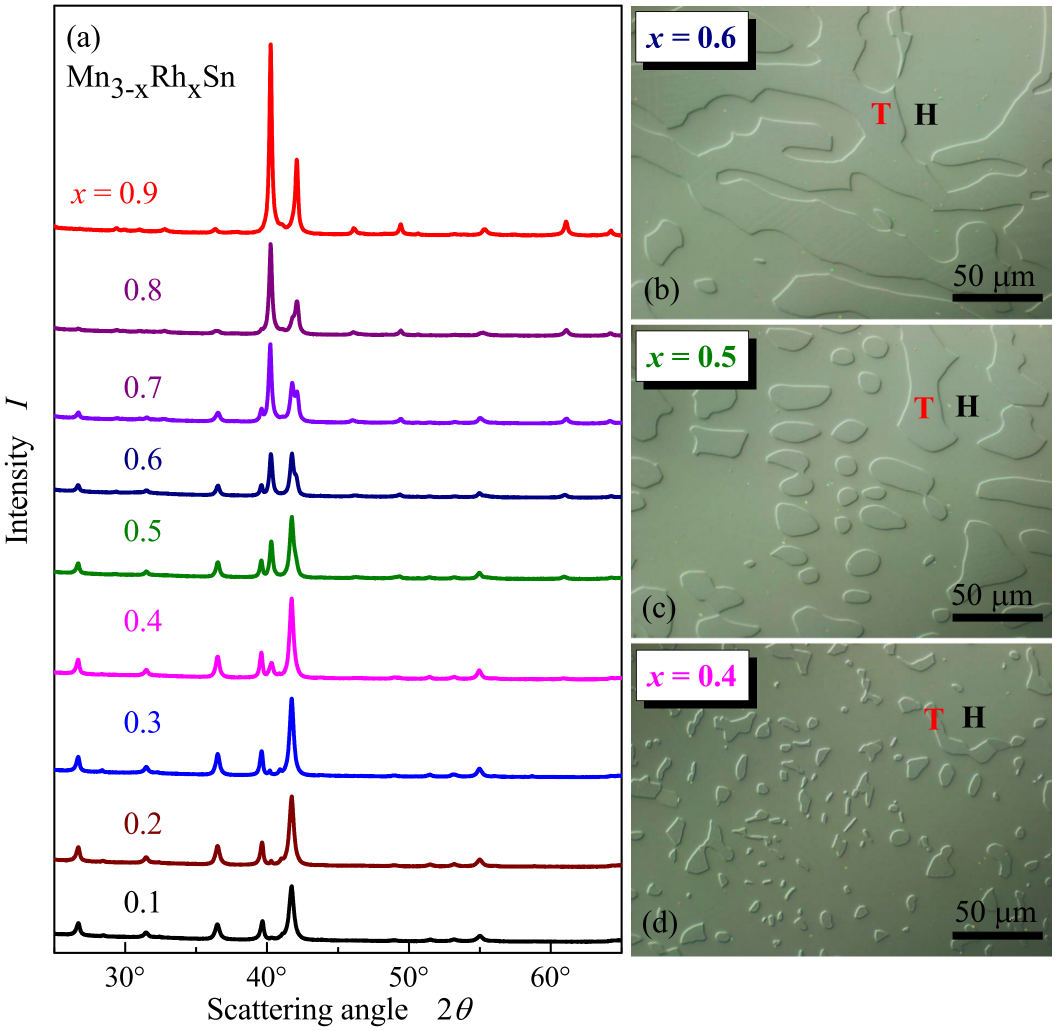

Figure 2.17: Structure of $Mn_{3-x}Rh_xSn$ bulk samples. (a) Powder XRD of the bulk sample series with the composition step $x = 0.1$. By decreasing the Rh content a gradually increasing hexagonal phase (symmetry group 194) is separating from the tetragonal phase (symmetry group 119). (b), (c) and (d) Phase separation is observed by the differential interference contrast microscopy for the Rh content of $x = 0.6$, 0.5 and 0.4 respectively.

the high quality evidenced by EDX and also XRD. Within this restriction, certain random intermixing of different atomic types would be still possible. However, any mixtures involving Sn are excluded, as this affects the zinc-blende substructure, which is the 'skeletons of any Heusler alloy (one can represent the Heusler structure as a zinc-blende + extra *d* elements). Certain intermixing in Rh-Mn_{II} plane would still be possible (indeed, there are Heusler systems stabilized by such mechanisms, e. g., Fe_2CuGa exhibits Fe-Cu intermixing [143]). However such disorder at high rates would lead to the statistical emergence of the inversion symmetry (which contradicts to the present XRD data, convincingly deducing the 119 symmetry group instead of 139, i. e., absence of the inversion symmetry, see Fig. 2.16).

Experimentally the phase stability of the compound with respect to composition has been investigated by considering Mn- and Rh-excess regimes. The Mn-excess series ($Mn_{3-x}Rh_xSn$, $x = 0.9, ..., 0.1$) always exhibit the phase separation, in a form of a growing amount of Mn-rich Mn_3Sn phase (group N 194, hexagonal), and the 'host' phase of Mn_2RhSn (see Fig. 2.17).

There is no direct transition between these crystal structures for the symmetry reasons: right at the composition of $Mn_{2.1}Rh_{0.9}Sn$ the phase separation begins, which is observed with the help of XRD, EDX, optical and electron microscopy. Introduction of additional Rh in Mn_2RhSn system (studied on thin films) reduces the c/a ratio and gradually brings the structure to the cubic phase (see Fig. 4.1). The stoichiometry control in thin films deposition is more sophisticated compared to the bulk synthesis; also, fewer reflexes are available for the XRD studies. However, from the peak positions and their intensity ratios it is concluded that the smallest Rh content, which is enough to form a cubic structure is $Mn_2Rh_{1.17}Sn$ (will be discussed in more details later). Thus, the Mn_2RhSn phase is rather sensitive to a slight stoichiometric deviation of Rh or Mn.

2.6 Summary

As demonstrated theoretically and experimentally, the design of non-collinear magnets within the Heusler family of materials can be based on Mn_2YZ compositions, with Y and Z being a non- or weakly-magnetic transition-metal and a main-group element, respectively. The choice of the Mn_2YZ Heusler group allows to control the canting angles by, e.g. combining the Y and Z elements or varying the Mn content. The use of heavy transition metals (e.g. as in the present case, Y=Pt, Rh, Ir and Z=Sn, In) amplifies the magnetically-relevant relativistic effects that are already present in these systems, such as the DM interaction and magneto-crystalline anisotropy. Such multiple magnetic degrees of freedom together with the possibility of their manipulation provided by the family of Mn_2YZ Heusler materials is vital for efficient engineering and stabilization of various magnetic orders. In particular, Mn_2RhSn is suggested to be a promising candidate for realizing the skyrmion state in the Heusler family.

3 Increasing the Curie temperature of Mn_2RhSn by Co-doping

For technological applications it would be desirable to increase the thermal stability, since Mn_2RhSn shows $T_C = 270$ K, i.e. below the room temperature. As it is well-known, the most thermally stable Heusler compounds are the Co-rich ones. Since Rh and Co belong to the same periodic group, partial substitution of Rh with Co seems to be the most straightforward way. On the other hand, since Mn_2CoSn is known to be cubic, one needs to find a compromise between the possibility of high T_C and sufficiently large tetragonal distortion.

3.1 Preface

To be applied in the spintronic devices, materials are required to switch magnetization at low critical current density and to exhibit a high thermal stability simultaneously. Due to the broad range of possible element combinations, Heusler compounds exhibit a flexible set of parameters. By tuning the composition and/or the heat treatment regime one can achieve a preferred structure symmetry (cubic, tetragonal, hexagonal), magnetic moment, spin-polarization and Curie temperature. Also, the lattice parameter can be optimized in order to achieve high-quality epitaxial thin films on the MgO substrate (tunneling barrier).

According to the Slonczewski-Berger equation [109, 110], tetragonal compounds with a low magnetic moment are preferred for the spin-torque transfer applications. Up to now, the most famous tetragonal Heusler examples are Mn_3Ga [111, 161] and related compositions - $Mn_{3-x}Ga$ with $Mn_{3-x}Co_xGa$ [112, 162]. Mn_2RhSn shows much closer lattice match with the MgO; in addition, its crystal structure can be much deeply analyzed - the compound is brittle, high quality powder can be easily obtained in contrast to ductile Ga-containing Heuslers.

Being tetragonal, Mn_2RhSn already exhibits a non-zero magnetocrystalline anisotropy in comparison to the cubic Heusler materials. Also, the presence of two magnetic sublattices introduces an additional degree of freedom for the magnetization control. Due to the fact that Mn magnetic sublattices orient in the antiparallel manner, the total magnetic moment is not very large, which is beneficial for the magnetization switching by the spin-torque process. However, the application potential of the Mn_2RhSn should be improved as of the low $T_C = 270$ K. Among the Heusler family, Co-containing compounds show the highest values of T_C for example, $T_C = 1120$ K of Co_2FeSi [108]. The following chapter discusses how the T_C can be significantly improved by the isovalent substitution of Rh by Co.

3.2 Sample preparation and precharacterization

The $Mn_2Rh_{1-x}Co_xSn$ polycrystalline bulk samples were repeatedly arcmelted from stoichiometric amounts of high-purity commercially available elements (> 99.99%) in an Ar atmosphere using the Ti getter. After six runs, the overall mass loss was less than 0.5 wt. %.

Similar to the parent The Mn_2RhSn compound, a two-step process was used. First, Rh-Co-Sn premelts were obtained, then preliminary purified Mn was introduced into the system: Mn chips were sealed in evacuated quartz ampules with relatively large internal volume and heated at 1000°C overnight. Later the samples were wrapped in Tantalum foil and sealed in evacuated silica tubes. Annealing lasted 1 week at 800°C. Samples were slow-cooled and pre-characterized.

Prior to structural and element-specific analysis, all samples were investigated by optical microscopy in a bright light (see Fig. 3.1), polarized light and back-scattering electrons (BSE) regimes. To prepare a smooth surface, samples were embedded in epoxy resin blocks. Metallographic analysis revealed that the samples are single-phase materials with a homogeneous composition distribution. The composition was characterized by the EDX spectroscopy at the precision of $\leq$0.5 at.%. Table 3.1 summarizes the results of the EDX, which are in a good agreement with the intended values.

Fig. 3.1 shows the microscopy of two compositions - the $Mn_2Rh_{0.7}Co_{0.3}Sn$ and $Mn_2Rh_{0.3}Co_{0.7}Sn$. The early sample reveals a certain stripe-like texture, which suggests the presence of a tetragonal structure. The latter sample shows a flat image under the polarized light, which corresponds to the structure of a higher symmetry. This discrepancy attracts an special attention to the crystal structure analysis.

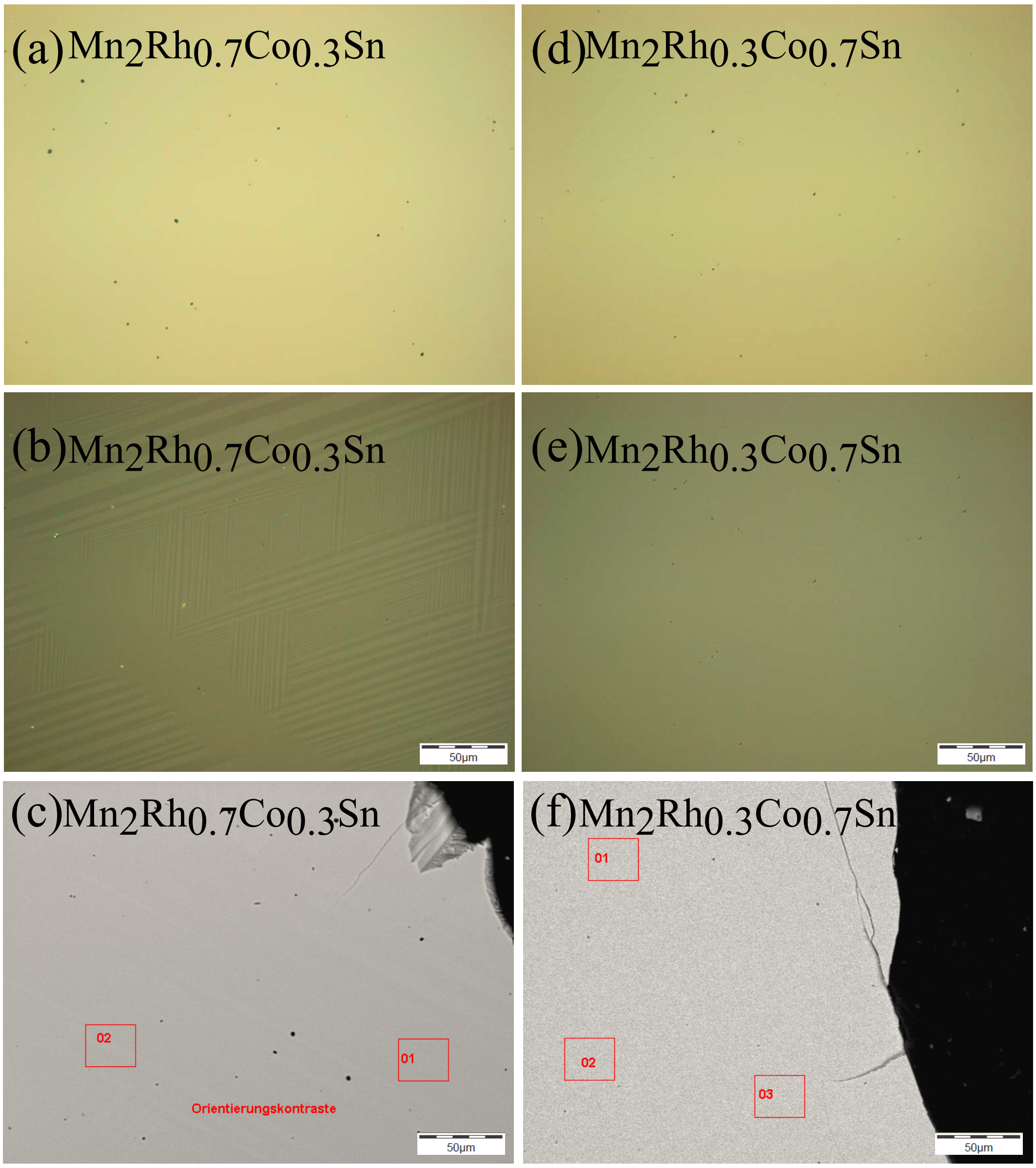

Figure 3.1: $Mn_2Rh_{0.7}Co_{0.3}Sn$ and $Mn_2Rh_{0.3}Co_{0.7}Sn$ in the bright light (a, d), polarized light (b, e) and back scattering electrons (BSE) (c, f) regimes.

No	Composition	Measured composition [at.%]			
		Mn	Rh	Co	Sn
1.	Mn_2RhSn	49.73	25.55	-	24.71
2.	$Mn_2Rh_{0.9}Co_{0.1}Sn$	49.64	23.13	2.81	24.42
3.	$Mn_2Rh_{0.8}Co_{0.2}Sn$	49.99	20.52	4.93	24.55
4.	$Mn_2Rh_{0.7}Co_{0.3}Sn$	49.51	17.06	8.41	25.03
5.	$Mn_2Rh_{0.5}Co_{0.5}Sn$	49.56	12.49	12.66	25.29
6.	$Mn_2Rh_{0.4}Co_{0.6}Sn$	49.46	10.13	15.32	25.09
7.	$Mn_2Rh_{0.3}Co_{0.7}Sn$	49.15	7.96	17.90	24.99
8.	$Mn_2Rh_{0.2}Co_{0.8}Sn$	49.96	5.34	19.53	25.17

Table 3.1: Composition analysis of $Mn_2Rh_{1-x}Co_xSn$ Heusler compounds.

3.3 Crystal structure analysis: tetragonal-to-cubic phase transition

This chapter is dedicated to the change of the $Mn_2Rh_{1-x}Co_xSn$ crystal parameters with the growing Co/Rh ratio. First, the RT results are discussed, then the transition into the high-temperature cubic phase is studied for different compositions.

Similar to the previous chapter, the room temperature powder XRD patterns were obtained in asymmetric Guinier transmission geometry (Image plate Guinier camera Huber G670, Cu K_α radiation, see Fig. 2.4) with LaB_6 added as an internal standard. To improve the peak-width and eliminate the powder size distribution, each sample has been preliminary sieved through 40 μm mesh. The obtained powder XRD patterns were refined by the Rietveld method with the help of FullProf [151] software. The treatment was done in 10 different steps: optimization of scale, peak shape, zero shift, background modeling, lattice constants, thermal expansion parameter, overall temperature factor, half-width parameters (U, V, W), peak asymmetry and a ratio of Lorentian-to-Gaussian peak profile.

No	Composition	a [Å]	c [Å]	c/a
1.	Mn_2RhSn	4.292(1)	6.619(1)	1.542
2.	$Mn_2Rh_{0.9}Co_{0.1}Sn$	4.287(1)	6.588(2)	1.537
3.	$Mn_2Rh_{0.8}Co_{0.2}Sn$	4.280(2)	6.559(1)	1.533
4.	$Mn_2Rh_{0.7}Co_{0.3}Sn$	4.272(1)	6.538(2)	1.530
5.	$Mn_2Rh_{0.5}Co_{0.5}Sn$	4.267(1)	6.449(1)	1.511
6.	$Mn_2Rh_{0.4}Co_{0.6}Sn$	6.145(8)	6.145(8)	1
7.	$Mn_2Rh_{0.3}Co_{0.7}Sn$	6.134(4)	6.134(4)	1
8.	$Mn_2Rh_{0.2}Co_{0.8}Sn$	6.119(7)	6.119(7)	1
9.	$Mn_2Rh_{0.1}Co_{0.9}Sn$	6.094(1)	6.094(1)	1

Table 3.2: The lattice parameters of $Mn_2Rh_{1-x}Co_xSn$ Heusler compounds at the room temperature.

3.3.1 Composition dependence

The gradual substitution of Rh by Co leads to the linear decrease of the c/a ratio (see Tab. 3.2). The phase transition into the cubic phase ($F\overline{4}3m$, no. 216) is observed at the $Mn_2Rh_{0.4}Co_{0.6}Sn$ composition. Fig. 3.2 represents the refined powder patterns of two mirror compositions: (a) a tetragonal $Mn_2Rh_{0.7}Co_{0.3}Sn$ and (b) a cubic $Mn_2Rh_{0.3}Co_{0.7}Sn$.

3.3.2 Temperature dependence

For the differential scanning calorimetry, $\sim$ 50 mg of a powder sample was prepared, the sample was encapsulated in the Al_2O_3 crucible, measurements were performed in Ar atmosphere from the room temperature up to 1500°C.

As it is known from the spin-resolved DOS calculations (private communications), the cubic phase is stable at larger unit cell volumes - therefore it forms at the elevated temperatures. In case of Mn_2RhSn parent phase, the cubic phase establishes between 530° C and 594° C, which is far above the $T_C = 270$ K. Therefore, magnetism was not considered in the calculations - this resulted into even larger instability at the

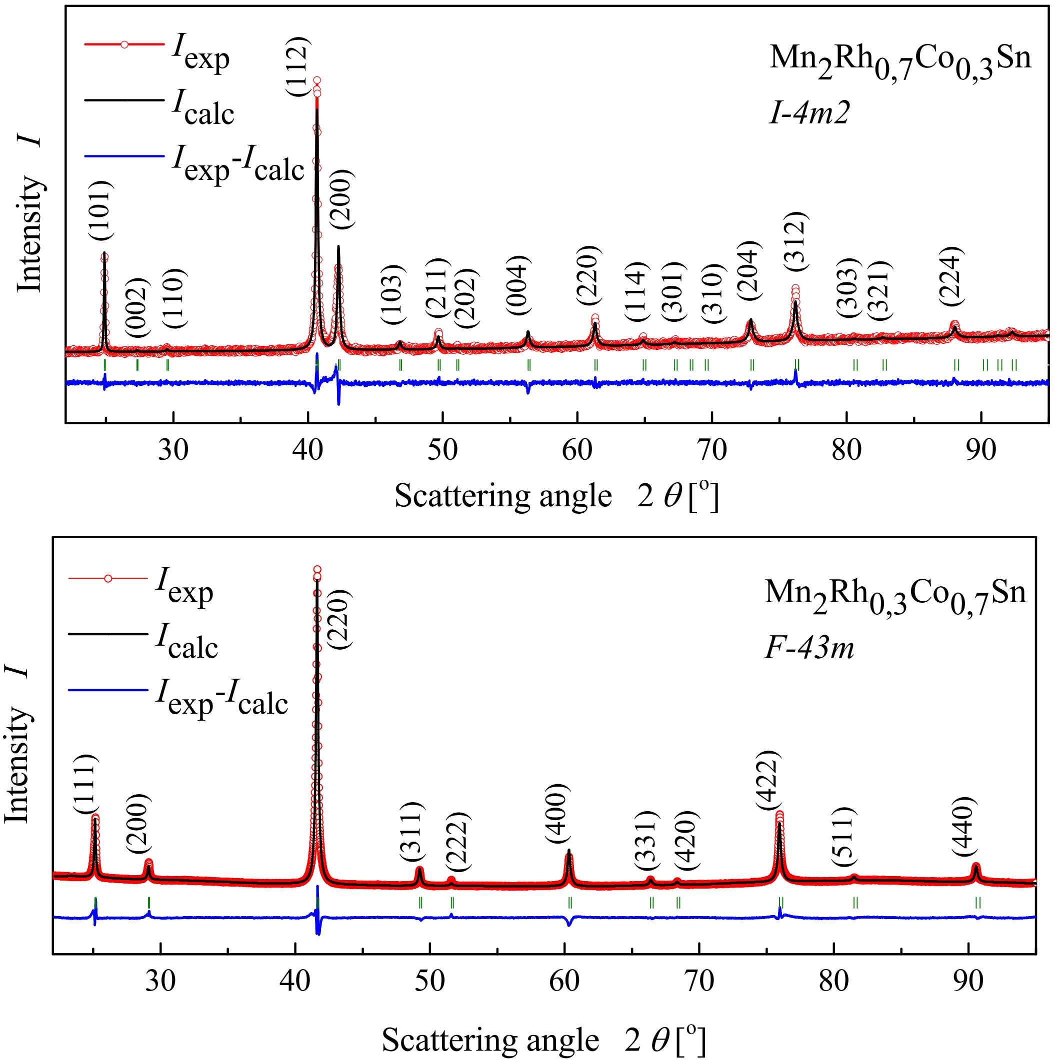

Figure 3.2: Room temperature powder XRD patterns of Rh- and Co-rich compounds of $Mn_2Rh_{1-x}Co_xSn$ series. $Mn_2Rh_{0.7}Co_{0.3}Sn$ and $Mn_2Rh_{0.3}Co_{0.7}Sn$ crystallize in the inverse tetragonal $I\bar{4}m2$ and inverse cubic $F\bar{4}3m$ structures respectively.

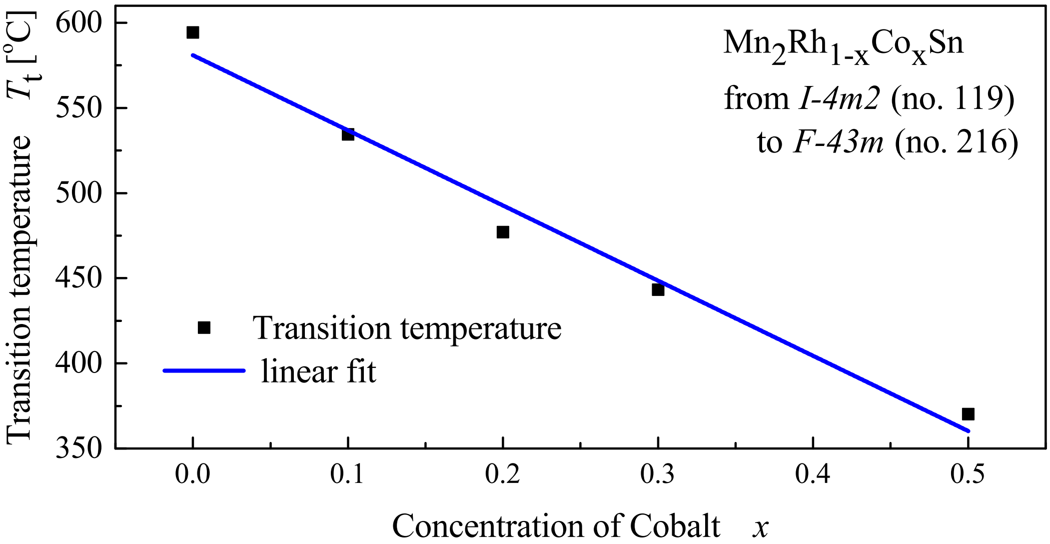

Figure 3.3: Dependence of the cubic-tetragonal transition temperature with the Co content. Inset: thermal hysteresis of Mn_2RhSn and $Mn_2Rh_{0.9}Co_{0.1}Sn$, intense and pale red correspond to heating regime, intense and pale blue mark cooling regime.

ϵ_F. Magnetism is a stabilizing factor in the formation of the cubic structure. When non-magnetic Rh is gradually substituted by the magnetic atom of Co, the transition temperature T_t linearly drops with the Co concentration (see Fig. 3.3).

The transition temperature as a function of Co-concentration follows a linear dependence with a negative slope of -441.34 K/atom (or -38.1 meV/atom).

3.4 Magnetic moment and Curie temperature

Temperature dependent magnetization measurements have been performed at constant field sweeps ranging from 0.1 to 5 T using Quantum Design MPMS XL superconducting quantum interference device (SQUID) magnetometer in the zero-field-cooled and field-cooled regimes. Additionally, an oven was used for the samples with the high T_C. Total magnetization was obtained from the hysteresis loops at 1.8 K.

Gradual introduction of Co into the system strengthens the effective magnetic coupling. This results in a monotonic increase of the T_C with respect to the Co content

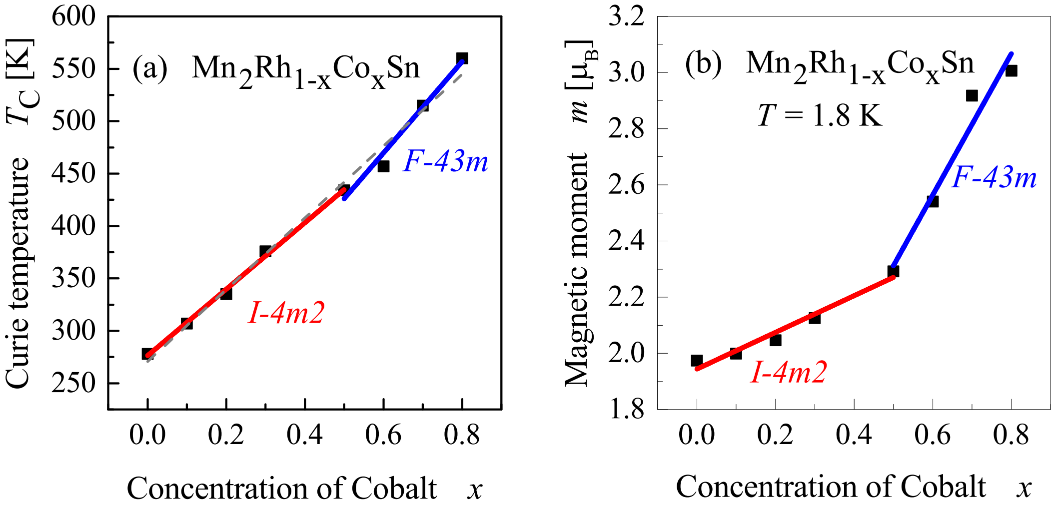

Figure 3.4: Left: T_C linearly increases with the Cobalt content. Right: magnetic moment increases at different rates for cubic and tetragonal phases.

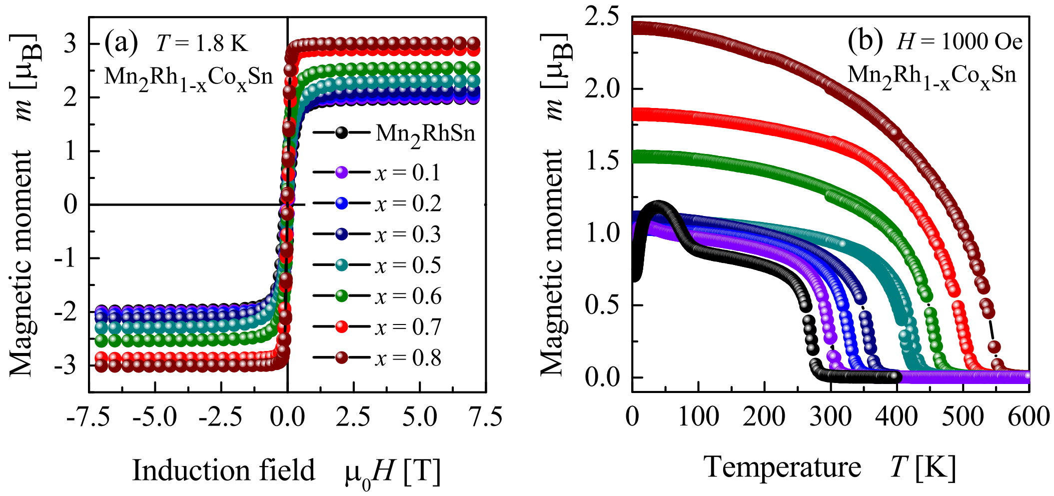

Figure 3.5: The highest value of the coercive field is observed for the tetragonal Mn_2RhSn compound. Further decrease of anisotropy shrinks the hysteresis loop.

(see Fig. 3.4, (a)). Interestingly, the behavior is rather independent of the tetragonal-to-cubic transition - the change of slope is insignificant at this point; the whole range of concentration reveals the slope of 342.3 K/atom (29.5 meV/atom). In contrast to the T_C, the magnetic moment shows two distinct areas corresponding to the $I\bar{4}m2$ (no. 119) and $F\bar{4}3m$ (no. 216) structures respectively (see Fig. 3.4, (b)). In the tetragonal phase, the increase is rather moderate with a slope of 0.65 μ_B/at, while in the cubic phase it becomes nearly 4 times larger: 2.5 μ_B/at. In the cubic symmetry, inter- and in-plane distances become equal, the total magnetic moment per unit cell is promoted by the strengthening of an additional magnetic Co-sublattice instead of non-magnetic Rh. The more rapid increase of the magnetic moment in the cubic phase can be explained by the reduced anisotropy and the soft hysteresis behavior (see Fig. 3.5, (a)). Introduction of Co into $\mathrm{Mn_2RhSn}$ balances the competing antiparallel interactions between the $\mathrm{Mn_I}$ and $\mathrm{Mn_{II}}$ sublattices. The magnetic transition caused by the spin reorientation of the second Mn sublattice, is observed only in the initial $\mathrm{Mn_2RhSn}$ phase and gets smeared by the increasing Co content (see Fig. 3.5, (b)).

3.5 Heat capacity

Heat capacity measurements were carried out using a bulk policrystalline pieces of about 50 mg from the room temperature down to 2 K. No magnetic field was applied.

Heat capacity represents the degrees of freedom for the crystal lattice to vibrate (a combination of the kinetic and potential energy) during the transfer of the thermal energy through the system. The mean internal energy $k_\mathrm{B}T$ of the linear harmonic oscillator consists of a kinetic part, namely, the vibrational motion of the oscillator, and the potential part, which corresponds to the elastic deformation. The energy per one mole of such an oscillator can be written as:

$$E = 3N_0 k_\mathrm{B} T = 3RT\,, \tag{3.1}$$

with the following heat capacity:

$$C_\mathrm{V} = \frac{\partial E}{\partial T} = 3R\,. \tag{3.2}$$

The majority of solids, which contain relatively heavy ions ($N_Z > N_\mathrm{Fe}$), follow the empirical Dulong-Petit law[1]:

$$3R = 24.94 \ [\mathrm{J/mol\ K}] \ . \tag{3.3}$$

This means that they are expected to have the same heat capacity at the room temperature. In case, the value of heat capacity is greater than the one expected from the Eq. (3.3), not only lattice vibration plays a role. The Eq. (3.3) considers the internal energy as a sum of energies from every atom, which is a linear oscillator with six degrees of freedom. Since there is still much of discrepancy between theory and experimental results, many models have been developed by now. The classical Einstein's theory is based on an assumption that each atom is free to move as a three-dimensional oscillator meaning that all atoms are vibrating with the same angular frequency.

Careful measurements show, however, that the Einstein's model goes somewhat below the experimental data. The Debye's model treats the solid as a continues elastic body rather than assuming a single vibration frequency for all $3N$ oscillators. In this case, each vibrational wave is a matter wave with an own de Broglie wavelength. Each energy level can be occupied by unlimited amount of phonons, therefore they are treated as bosons. The lattice vibrations are quantized, at the low temperature only the low-frequency modes are excited. Since their wavelengths are typically much longer than the inter-atomic distances, the solid is treated as a continuous media. Setting an upper limit for the frequency w_{D}, one can separate the low-temperature regime where all atomic vibrations are collective from the high-temperature regime with an independent vibrations of atoms. The limiting wavelength should be comparable with the inter-atomic distances, while the shorter wavelengthes are not permitted by the Debye theory. The characteristic temperature is also called the Debye temperature and can be defined for the isotropic media, N molecules per mole each comprising n atoms as follows:

$$\Theta_{\mathrm{D}} = \frac{\hbar w_{\mathrm{D}}}{k_{\mathrm{B}}} = \frac{\hbar c}{k_{\mathrm{B}}} \left(\frac{6\pi^2 N n}{V} \right) . \tag{3.4}$$

Taking the derivative of the energy E

$$E = E_0 + 9Nnk_{\mathrm{B}}T \left(\frac{T}{\Theta_{\mathrm{D}}} \right)^3 \int\limits_0^{x_{\mathrm{D}}} \frac{x^3 dx}{e^x - 1} \tag{3.5}$$

---

[1] The Dulong-Petit law holds for the specific heat at the constant volume C_{V}. However, the discrepancy at the room temperature is minor $\frac{C_{\mathrm{P}} - C_{\mathrm{V}}}{C_{\mathrm{V}}} \leq 0.04$ [163].

with respect to the temperature, Debye obtained the expression for specific heat [164]:

$$C_V = 9Rn \left[\frac{4}{x_D^3} \int_0^{x_D} \frac{x^3 dx}{e^x - 1} - \frac{x_D}{e^{x_D} - 1} \right] , \tag{3.6}$$

where $x = \hbar w / k_B T$ and $x_D = \hbar w_D / k_B T = \Theta_D / T$. Comparing the theoretical models with experimental results, one finds described the heat capacity by the contributions from the crystal lattice, itinerant electrons having a high mobility, and magnons or magnetic anomalies, represented by the localized electrons:

$$C_P(T) = C_{latt} + C_{el} + C_{magn} . \tag{3.7}$$

At the very low temperature, in a linear regime, the heat capacity is defined as

$$C_{latt}(T) = \beta T^3 . \tag{3.8}$$

where the β-coefficient is connected to the Debye temperature $\Theta_D = \sqrt[3]{1944 n / \beta}$. In the temperature range ($\Theta_D/50 \leq T \leq \Theta_D/10$) the phonon heat capacity needs a more sophisticated description:

$$C_{latt} = \beta T^3 + \delta T^5 + \epsilon T^7 + \ldots . \tag{3.9}$$

and is not considered here. The Debye temperature Θ_D cannot be simply treated as a number, since it is a temperature-dependent function and can have a non-trivial behavior. It stays constant up to the $\Theta_0/50$, where the Θ_0 is defined from the low-temperature fit and can be called an initial Debye temperature. Later, it experiences a minimum at $\sim \Theta_0/10$, then increases up to the $\Theta_0/2$. The Debye temperature plays a major role in the solid state physics, consequently it can be defined from a series of other experiments: measurement of the velocity of sound, resistivity, thermal expansion measurements, melting point or γ-, X-ray or neutron scattering. The electron heat capacity in the first approximation is obtained from

$$C_{el} = \gamma T . \tag{3.10}$$

Defining the Sommerfeld coefficient of the electronic heat capacity γ, one can estimate the amount of states at the Fermi level ϵ_F by the relation:

$$\eta(\epsilon_F) = 0.42425 \cdot \gamma \tag{3.11}$$

Plotting the experimental data $C/T = f(T^2)$ up to 10 K one obtains β as a slope

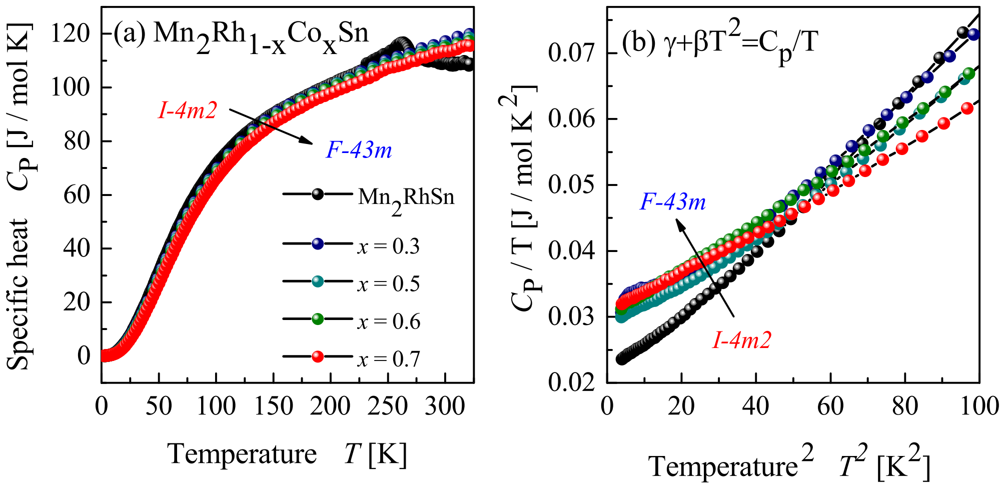

Figure 3.6: (a) Specific heat of the $Mn_2Rh_{1-x}Co_xSn$ series. (b) The electronic contribution to the heat capacity is defined as an intercept from the linear fit of the $\gamma + \beta T^2 = C_P/T$.

and γ as an intercept from the linear fit (see Fig. 3.6, (b)). The β and Θ_D are related through

$$\Theta_D = \sqrt[3]{\frac{1944 \cdot n}{\beta}} \tag{3.12}$$

The ratio of γ and β gives the squared value of the crossover temperature $T_{cr} = \sqrt{\gamma/\beta}$.

Though magnetic excitations at the low temperature can be by about 50 times smaller than the other two [165] and are hardly visible, one may still extract this contributions as follows [166]:

$$C_{magn} = \delta T^{3/2}\,. \tag{3.13}$$

Therefore, the total heat capacity contains all three terms:

$$C_V = \gamma T + \beta T^3 + \delta T^{3/2}\,. \tag{3.14}$$

By analyzing the zero-field heat capacity of $Mn_2Rh_{1-x}Co_xSn$ series (see Tab. 3.3), it is observed that Sommerfeld coefficient of the electronic heat capacity increases with the increased Co concentration.

x	γ [mJ/mol K^2]	β [mJ/mol K^4]	δ [mJ/mol K^2]	$\eta(\epsilon_\mathrm{F})$ [states/eV f.u.]	Θ_D [K]
-	21.84(7)	0.41(5)	6.50(1)	9.27	279.1
0.3	31.50(2)	0.26(1)	10.31(2)	13.36	310.5
0.5	29.11(4)	0.28(3)	10.82(1)	12.35	303.8
0.6	30.19(6)	0.35(5)	12.82(2)	12.81	282.3
0.7	30.87(4)	0.29(3)	13.06(2)	13.10	297.6

Table 3.3: Physical property data of the $Mn_2Rh_{1-x}Co_xSn$ series derived from the zero-field heat capacity measurements.

The low-temperature fit of the phonon contribution reveals slightly scattered values with the composition; overall, it is reduced with the increased Co content. Contrary, the magnon propagation becomes promoted and linearly increases.

3.6 Summary

As shown experimentally, the Mn_2RhSn can be optimized for the industrial applications in terms of the structure, magnetic moment, lattice parameter, anisotropy and the Curie temperature. If focused on the tetragonal distortion, which is favorable for the STT technology - the optimal composition is $Mn_2Rh_{0.5}Co_{0.5}Sn$. It still preserves the distortion while exhibiting the significantly improved $T_\mathrm{C} = 434$ K in comparison to the 270 K of Mn_2RhSn. Moreover, the lattice parameter of $Mn_2Rh_{1-x}Co_xSn$ gradually approaches the lattice parameter of the MgO with the increase of Co concentration.

4 Structural, electronic, and magnetic properties of perpendicularly magnetised Mn_2RhSn thin films

Epitaxial thin films of Mn_2RhSn were grown on MgO(001) substrate by magnetron co-sputtering of the constituents. An optimised range of temperature for heat treatment was used to stabilise the tetragonal structure and to prevent capping Rh layer from diffusing into the Heusler layer. Electronic and magnetic properties were analysed by hard X-ray photoelectron spectroscopy (HAXPES) as well as field and temperature dependent Hall and resistivity measurements. The measured valence spectra are in good agreement with the calculated density of states. The measured saturation magnetisation corresponds to 1 μ_B per formula unit. The magnetisation measurements revealed an out–of–plane anisotropy energy of 180 kJ/m^3 and a maximum energy product of 45.3 kJ/m^3. The magnetoresistance ratio is lower than 2% for fields below 9 T. The lattice parameter of the compound has a very small mismatch with MgO, which makes it promising for coherent electron tunnelling phenomena.

4.1 Preface

Mn_2YZ-based Heusler systems (where Y is a late transition metal and Z is a main-group element) represent a large family of ferrimagnets, which enables the engineering of exotic magnetic and transport phenomena. Among the most recent of them, for instance, are the single-spin localization [113], spin gapless semiconductivity [132] in the Mn_2CoAl compounds, and giant intrinsic exchange bias in the $Mn_{3-x}Pt_xGa$ alloys [130]. As tunable ferrimagnets, Mn-based systems exhibit large variability of compensation temperatures, which automatically makes them interesting candidates for all-optical switching [167]. Due to their non-centrosymmetric and tetragonally distorted structure, they can exhibit important relativistic effects, such as Dzyaloshinskii-Moriya interaction [16, 17] and magnetocrystalline anisotropy, which can be further amplified by introducing heavy Y and Z elements. As it is well-known, these are the necessary ingredients for the formation of the magnetic skyrmion structures [81, 124, 168, 169, 93]. Skyrmions were theoretically predicted for the bulk non-centrosymmetric systems more than a decade ago [49]. Recent experimental studies, which demonstrate a complex non-collinear magnetic behavior in Mn_2RhSn [170], also indicate the realistic possibility of engineering the skyrmion states in this and similar Heusler systems.

In order to understand the applicability and the potential for a possible skyrmion state in Mn_2RhSn, it is necessary to produce the material in a thin film form, which is suitable for various experimental characterizations. Moreover, in geometrically constrained systems, the skyrmion phase persists within a wider field-temperature regime [93]. Thin films allow further incorporation into more complicated devices based on superstructures and multilayers combined with the most commonly used substrate or spacer materials. One of the important technological requirements for new materials is their lattice match with MgO as tunnelling barrier. Also, thin films are perfect samples for the ferromagnetic resonance experiments due to the sample amount, shape factor and defined magnetization direction. This is one motivation for the present chapter, which is devoted to the growth and characterization of the magnetic and electronic properties of Mn_2RhSn thin films.

4.2 Sample preparation and precharacterization

Thin films of $(Mn_2Sn)_{1-x}Rh_x$ compositions have been deposited by a magnetron co-sputtering technique from two cathodes ($Mn_{60}Sn_{40}$ and Rh) in ultra-high vacuum. By varying the plasma power ratio of the targets and maintaining the constant deposition rate, a proper 2:1:1 composition was achieved. MgO single crystal (001) substrates were preliminary cleaned in ultrasonic bath using acetone, ethanol and distilled water. To remove residual water, the substrates were annealed at 700°C for 1 hour. All films were initially capped with a 5 nm Rh capping layer. Later, the samples for XMCD were gently cleaned by removing the existing Rh layer and recapped with 3 nm of Al.

To control the film thickness, two samples were deposited in each experimental run. An additional sample was grown through a mask; a difference between the empty substrate and the area of deposited material was checked by the thickness profile.

Table 4.1: Lattice parameters (in Å) measured at room temperature for several Mn-based Heusler materials compared to the MgO lattice, bulk samples [139, 111, 171, 172, 173, 174]. Note^1: these Heusler compounds crystallize in the structure.
Note^2: $a/\sqrt{2}$ is given for cubic compounds.

MgO	Mn_2RhSn	Mn_3Ga	Mn_2FeGa	Mn_2NiGa^1	Mn_2CoGa^1	Co_2MnSi^1
4.212	4.289	3.904	3.715	4.177^2	4.145^2	4.009^2

4.3 Crystal structure

Mn_2RhSn crystallizes in the inverse tetragonal Heusler structure [139], which in contrast to most of Ga-based compounds, exhibits a rather small lattice mismatch with MgO - about 2% (see Table 4.1). This is an important precondition for the successful manufacturing of thin films and tunnel junction.

X-ray diffraction patterns have been recorded in the in–plane and out–of–plane geometries. For a first estimation of the deposition parameters, the substrate temperature was varied from the 20°C to 700°C. The structure of the films was analyzed by X-ray diffraction using the parameters of a bulk Mn_2RhSn sample [139] as a reference. The films deposited at 450°C show the best matching peak positions and intensity ratios with respect to the powder XRD. Thus the tetragonal $I\bar{4}m2$ (space group no.: 119) structure of thin films is confirmed. The crystal structure has no inversion center and the Mn atoms occupying different Wyckoff sites: Mn_I in $2b$ (0, 0, 1/2) and Mn_{II} in $2c$ (0, 1/2, 1/4), whereas Rh is in $2d$ (0, 1/2, 1/4) and Sn in $2a$ (0, 0, 0) positions.

Fig. 4.1 shows the XRD pattern of thin films depending on the composition (4.1, (b)) or annealing procedure (4.1, (c)). The bulk compound shown in 4.1, (a) is given for comparison. Introducing additional Rh into the tetragonal Mn_2RhSn (space group $I\bar{4}m2$, no. 119) results in a gradual decrease of the c/a ratio and a tetragonal to cubic phase transition (see Fig. 4.1) is observed. The stoichiometric thin film exhibits lattice parameters of $a = 4.37$ Å and $c = 6.52$ Å resulting in $c/a = 1.51$.

To find a proper Rh:(Mn_2Sn) ratio, the composition was tuned from the Rh-rich to the Rh-poor regime. Rh_2MnSn crystallizes in a cubic structure [175, 176, 177, 178]. The other limiting case, Mn_2Sn [179, 180] has a hexagonal structure. The reduction of Rh content in the $Mn_{2+x}Rh_{1-x}Sn$ compound leads to a decomposition into two

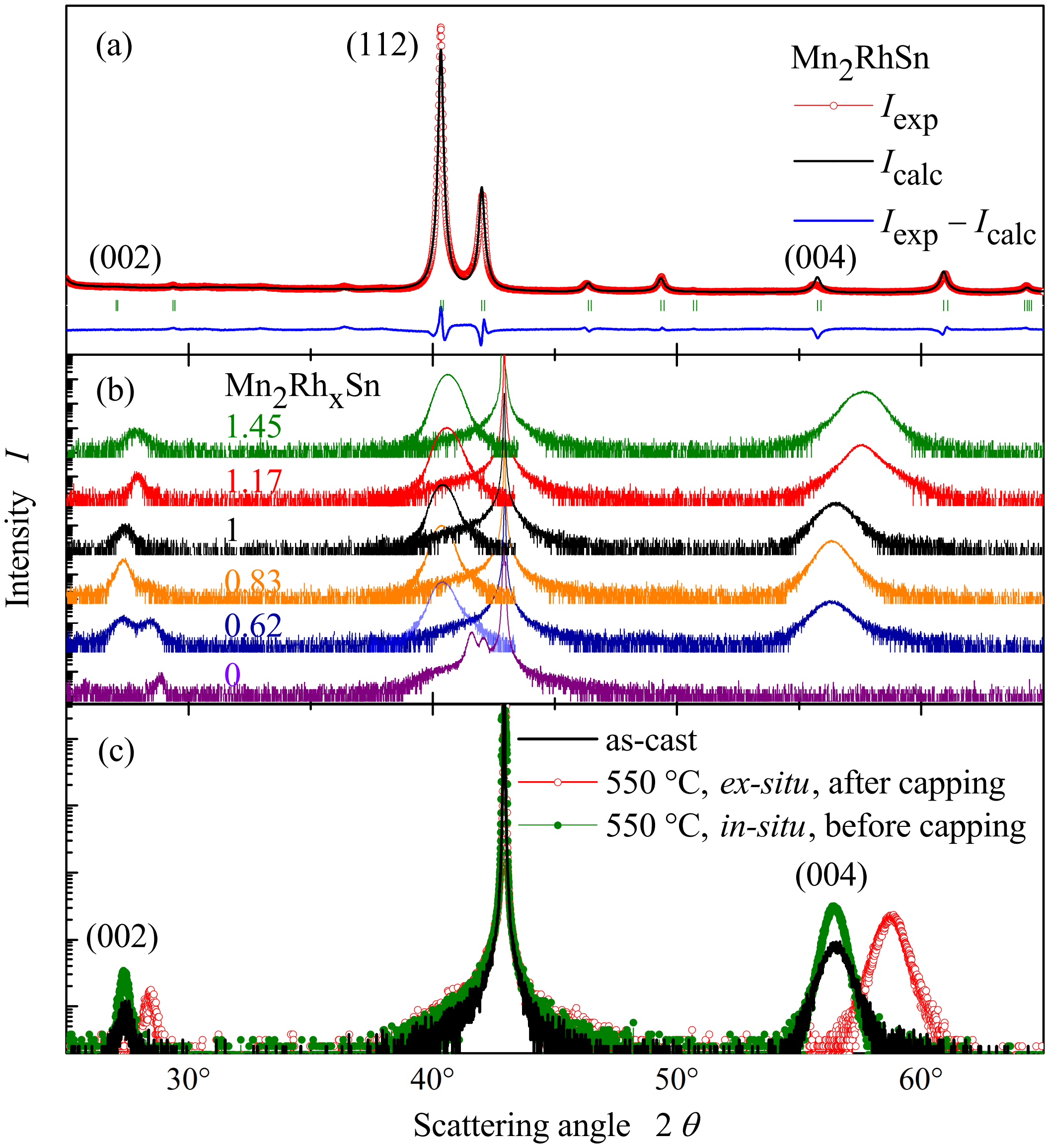

Figure 4.1: (a) Powder XRD of Mn_2RhSn bulk sample. (b) XRD of Mn-Rh-Sn thin films, shift of the (002), (004) and (112) peaks with respect to the Mn_2Sn-Rh ratio. Here the (002) and (004) peaks were obtained in the out–of–plane scan, while the (112) peak was recorded in the in–plane geometry and later added to the (002) and (004) data. (c) The *in-situ* annealing at 550°C is preferred before the capping deposition, since the *ex-situ* process leads to Rh diffusion from the capping layer and a change to the cubic structure.

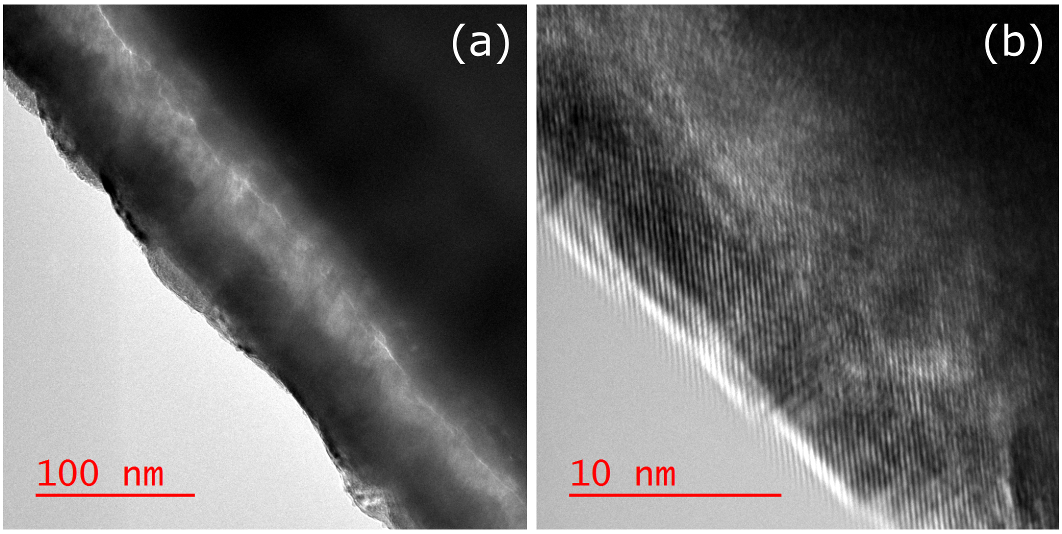

Figure 4.2: (a) TEM and (b) HR-TEM images of Mn_2RhSn thin films.

phases with competing structures (see Fig. 2.17). For example, $Mn_{2.5}Rh_{0.5}Sn$ is represented as a sum of hexagonal $Mn_{2.75}Rh_{0.17}Sn$ and tetragonal $Mn_2Rh_{0.85}Sn$ (within an experimental uncertainty of about 1 at.%). This behavior, known from the bulk studies [139], is well reproduced in the thin films. $Mn_2Rh_{0.83}Sn$ shows a higher (002) peak (see Fig. 4.1), which is due to a contribution from the growing Mn_2Sn phase. The Rutherford backscattering spectrometry (RBS) revealed a composition of $Mn_{48.1\pm1}Rh_{26.3\pm2}Sn_{25.6\pm2}$. This proves the adjustment of the stoichiometry by means of the lattice parameter optimization. A 5 nm thick capping layer of Rh was deposited on top of the Heusler film to protect the films from oxidation.

The quality of the samples strongly depends on the heat treatment, therefore, an annealing step is essential. According to differential scanning calorimetry and high temperature XRD – both measured on bulk samples – the structure exhibits a transition into a high-temperature cubic phase between 570 and 580°C. The films were annealed at 550°C (see Fig. 4.1 (c)) to preserve the tetragonal distortion. Nonetheless, the cubic structure was formed due to the Rh diffusion from the capping layer into the Heusler layer. On the other hand, the *in-situ* annealing prior to the deposition of the capping layer significantly improves the crystallinity while preserving the tetragonal structure.

Additionally, the samples were investigated by the transmission electron microscopy (TEM). Preparing a sufficient sample is a jewelery art work. For the planar view, first, 9 μm diamond film was used for thinning the sample at a very gentle speed of 20 rpm. When the thickness was reduced to 300 μm, a more fine diamond film of 6 μm was applied until the thickness of 100 μm was achieved. Further, the sample was thinned by a dimple grinder. A shiny thin surface was achieved by cubic boron nitride and aluminum oxide abrasive materials. The sample was then placed on a copper mesh and fixed with glue. For the cross-section view, the sample was cut with the focused ion beam (FIB). The TEM images in a normal and a high-resolution mode (see Fig. 4.2) represent the film structure. The thickness is proved to be about 50 nm, while roughness could be further improved.

4.4 Spectral characterization

Hard X-ray photoemission spectroscopy (HAXPES) has been performed at the undulator beamlines BL47XU [181] and BL15XU [182, 183] of SPring-8 (Japan). See Ref. [184, 185, 186] for more details of the HAXPES measurements. The films with and without Rh capping as well as 2 nm Al-capped films were studied, the results were compared to the bulk sample fractured *in-situ*. The spectra were obtained in the temperature range between 20 and 300 K in the base pressure of 10^{-7} mbar. The core level spectra have been treated using the Unifit 2013 software [187]. The background was subtracted according to the Shirley correction procedure. An iterative fitting was performed until the least-square discrepancy ($\chi^{\star 2}$) was reduced to below 1.

A bulk sample has been used as a reference to study the spectral characteristics of the film. The wide energy HAXPES (see Fig. 4.3) spectra show all expected electronic contributions from the constituting elements. Changing the excitation energy results in different cross sections. This changes the peak intensities of different element contributions but keeps the intensity ratio within each element.

The bulk sample (see Figure 4.3 (c)) was fractured *in-situ* in the ultra high vacuum chamber. No trace of MnO_x was observed (MnO_2 states are expected at about 530 eV as marked by an arrow in the inset). The survey of the Al-capped film perfectly resembles the states of the bulk sample. The additional oxygen 1s state being observed in the spectrum of the thin film arises from the AlO_x capping layer. The peaks in the vicinity of the Fermi energy ϵ_F are by two orders of magnitude less intense than the core level states [188] and require longer measurement time. At least 25 measurement iterations were carried out to improve the signal to noise ratio of the valence band spectra.

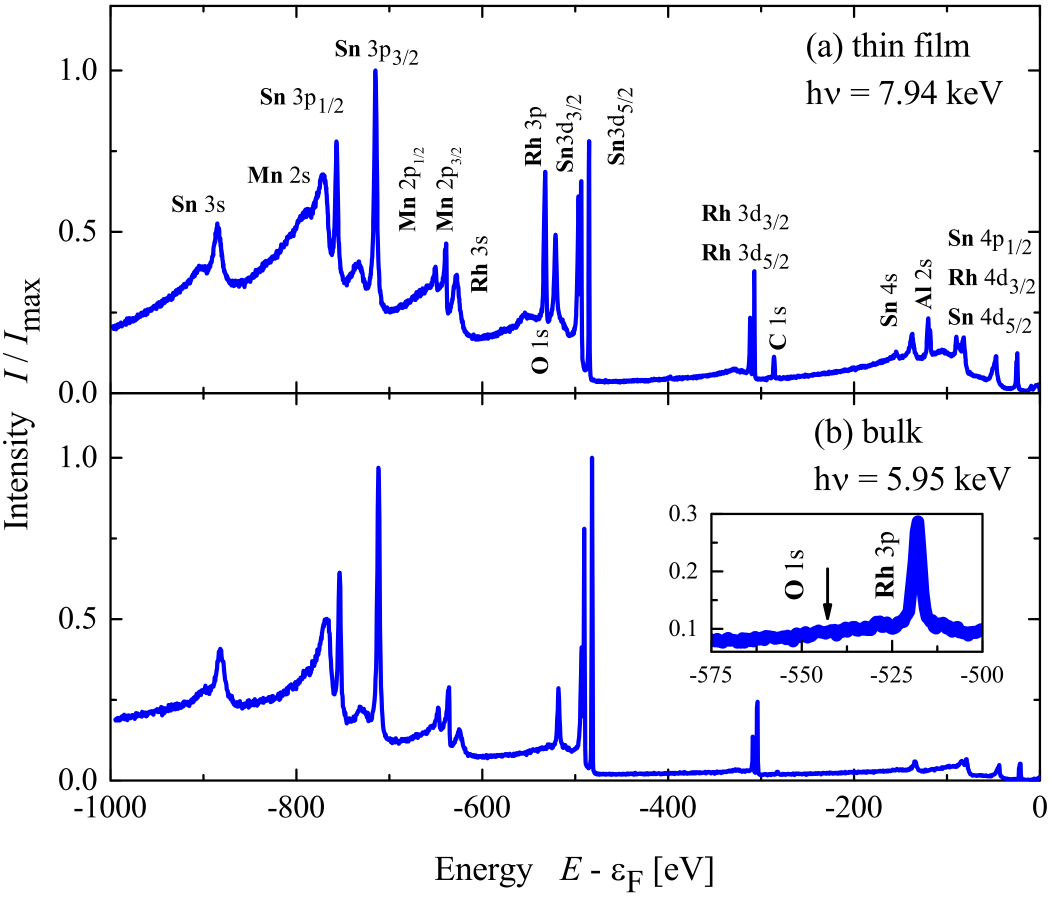

Figure 4.3: HAXPES survey spectra of Mn_2RhSn. Panel (a) shows the wide energy range spectrum of the AlO_x capped thin film measured at 40 K with an excitation energy of 7.94 keV. (b) Spectrum of the bulk sample obtained at 20 K with 5.94 keV. Inset: For the bulk sample no trace of oxidation is observed in the vicinity of the O 1*s*-peak.

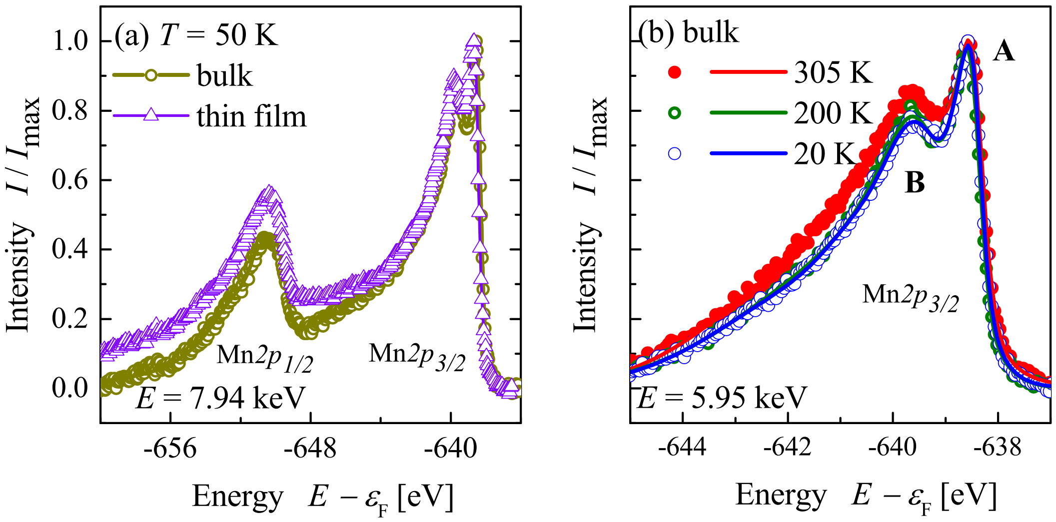

Figure 4.4: HAXPES spectra of the $2p$ core states of Mn in Mn_2RhSn; open marks are the measured data and solid line is the result of refinement. (a) Spectra of the bulk sample compared with the Al-capped film. Measurement was carried out at 50 K with an excitation energy of 7.94 keV. (b) Mn $2p_{3/2}$ states evolve with the temperature. The spectra from bulk were obtained at 5.95 keV incoming photon energy. **A** and **B** assign the well screened peak with high J and the poorly screened satellite.

4.4.1 HAXPES of core states

The Sn $3d$ state exhibits a larger spin-orbit splitting compared to Rh $3d$ core level: $\Delta_{\mathrm{SO}}^{\mathrm{Sn}}(3d) = 8.4$ eV and $\Delta_{\mathrm{SO}}^{\mathrm{Rh}}(3d) = 4.6$ eV. The splitting of the Rh $3p$ states is about 6 times larger compared to that of Rh $3d$: $\Delta_{\mathrm{SO}}^{\mathrm{Rh}}(3p) = 24.8$ eV. Instead of a pure spin orbit doublet, the Mn $2p$ states show a complicated multiplet structure (Figure 4.4). Similar splittings in Heusler compounds have been first observed by Yarmoshenko *et al* [189]. Such behavior is attributed to the exchange coupling of the $2p$ core hole and the localized valence d states of Mn. This many electron effect was explained for Heusler compounds in Refs [190, 191] or in more general by de Groot and Kotani in Reference [192]. The multiplet effect is observed in both, the bulk sample and the thin film.

A closer look at the Mn $2p_{3/2}$ excitation (see Fig. 4.4 (b) for the bulk sample) reveals a splitting into four major sublevels separated by about 1 eV. Their width is about 0.5 eV. The complete multiplet structure spans over about 4 eV below the main $2p_{3/2}$ line. The $2p_{3/2}$ multiplet can be described by a jj coupled state that is LSJ coupled to the valence electrons. The ground state of the Mn atom is $3d^5 4s^2 (^6S_J)$. The $2p - 3d$ exchange interactions couples the $2p^5$ core hole and the $3d^5$ valence electrons to four levels with total angular momenta $J = 4, 3, 2$, and 1. In localized materials the states with lowest binding energy are well screened (peak **A** in Figure 4.4 (b)) in contrast to the poorly screened states at higher binding energies. The electron correlation effects are mainly responsible for the shape of the satellite features. The shape of the $2p_{3/2}$ spectrum is different from that of Heusler compounds with regular $L2_1$ crystalline structure (compare Refs [190, 191]). The differences are attributed to the differences in the crystalline structure. In the present case of Mn_2RhSn, the Mn atoms occupy two different, non equivalent sites. Therefore, an additional broadening of the lines appears that is caused by the two specific surroundings of the Mn atom (see Fig. 4.5, inset).

The exchange splitting of the Mn $2p_{3/2}$ state depends on the temperature, as is seen in Fig. 4.4 (b). The intensity ratio for the bulk sample is calculated between the well screened peak (**A**) and the satellite (**B**). It increases with increasing temperature and equals to 0.77, 0.78 and 0.86 for 20, 200, and 305 K, respectively. This hints that even above the T_C a localized but disordered magnetic moment persists at the Mn atoms [193].

4.4.2 HAXPES of valence states

The HAXPES valence band spectra of Mn_2RhSn bulk material and thin film are shown in Fig. 4.5(a) and compared to the calculated density of states in Fig. 4.5(b). The valence band spectrum of the Al-capped Mn_2RhSn thin film is slightly different from that of the bulk sample. It exhibits more pronounced features due to the higher crystalline order. Deposition of a Rh capping layer influences the photoemission signal of the core levels and the valence states. For instance, the so-called Heusler gap (at about -8 eV) is completely covered by Rh d-states and not longer visible in spectra (not shown her). It was not possible to detect the Heusler layer underneath a Rh capping layer of 5 nm thickness. The situation is different in the case of an AlO_x capped film. The states of an insulating AlO_x capping layer don't contribute to the emission close to ϵ_F energy due to the wide band gap of the oxide.

The electronic structure of Mn_2RhSn was calculated with the SPR-KKR method [155]. A comparison of the valence-band photoelectron spectra to the atomic site resolved densities of states reveals the origin of its main features (see Fig. 4.5). The Mn

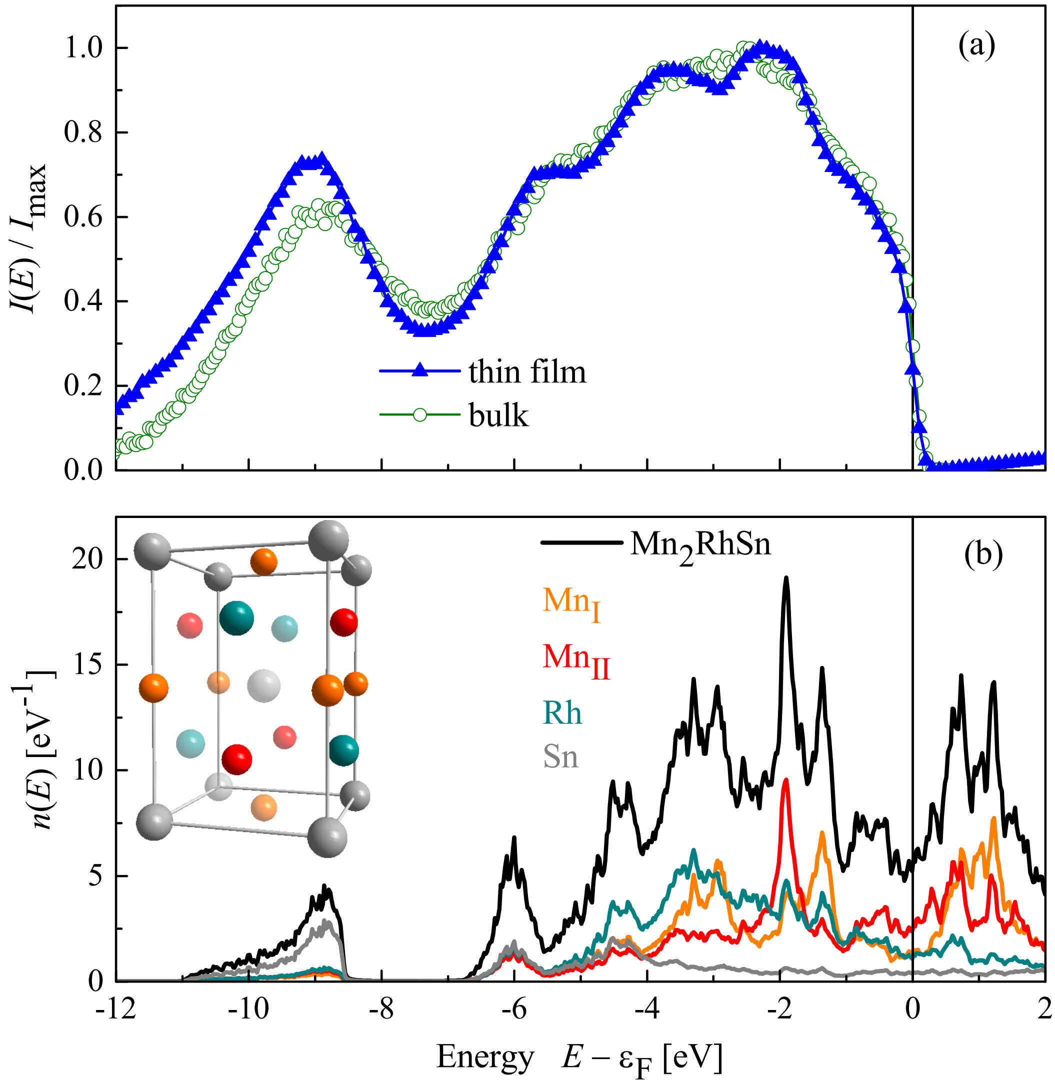

Figure 4.5: HAXPES spectra of the Mn_2RhSn valence band measured with the excitation energy of 7.94 keV. (a) Spectra of a bulk sample and a thin film measured at 50 K. (b) Calculated total and site resolved partial density of states.

Table 4.2: Scattering contributions to the temperature-dependent resistivity obtained as fit parameters of the Bloch–Grüneisen equation.

Temperature range [K]	$\rho_{e\text{-}e}$ [$\mu\Omega$cm]	$\rho_{e\text{-}ph}$ [$\mu\Omega$cm]	Θ [K]
2 – 60	42.9±2.8	20.5±3.1	295.5±8.9
2 – 70	38.2±1.5	24.2±2.1	280.1±4.4
2 – 80	34.0±1.0	28.6±1.8	266.4±3.1
2 – 90	30.4±0.9	33.0±1.7	254.8±2.6
2 – 100	26.4±1.0	38.7±2.1	241.6±2.8
2 – 110	21.1±1.3	46.4±2.9	224.2±3.5

atoms are well distinguished by their different surroundings. $\mathrm{Mn_I}$ in the 2a Wyckoff position is considered more localized, whereas $\mathrm{Mn_{II}}$ in the 2c position is more itinerant. Structural stability of the compound is indicated by the fairly large *sp* hybridization (Heusler) gap (between -8.5 and -6.8 eV) and the absence of a sharply peaked density of states in the vicinity of the Fermi energy ϵ_F. Three maxima are resolved in the energy range of the d states. The states closest to ϵ_F are mainly contributed by $\mathrm{Mn_{II}}$ and less pronounced from $\mathrm{Mn_I}$ or Rh. The excitation at about -2 eV has the highest intensity in the photoelectron spectrum. It consists of d-states from $\mathrm{Mn_I}$ (-1.5 eV) and $\mathrm{Mn_{II}}$ (-2 eV). The density of Rh states increases with increasing distance from ϵ_F and has a maximum at about -3.5 eV as seen from the calculated density of states. The s-band appears below -8 eV. It is more intense for the film compared to the bulk sample. Such an enhancement is caused by the roughness of the bulk material after fracturing. The bulk sample has no microscopically well defined surface normal compared to the thin film.

4.5 Transport properties

The *zero-field* temperature dependent resistivity is shown in Fig. 4.6. It exhibits a positive temperature coefficient which manifests a typical metallic behaviour. The residual resistivity $\rho_{2\mathrm{K}} = 113$ $\mu\Omega$cm at 2 K and the residual resistivity ratio $RRR = \rho_{300\mathrm{K}}/\rho_{2\mathrm{K}} = 1.34$ are in the typical range of sputtered Heusler films [194, 195, 196, 197]. The high temperature resistivity follows above 150 K a nearly linear behavior

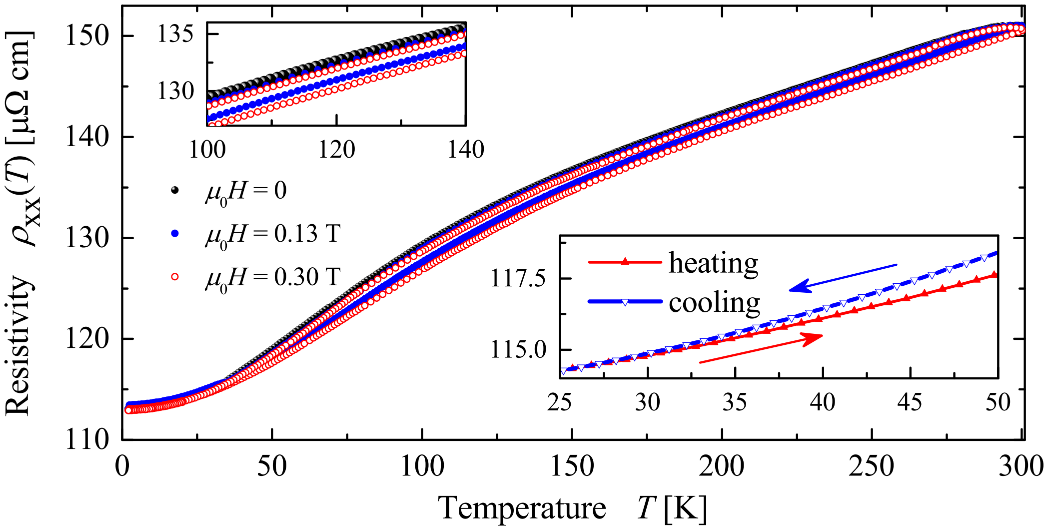

Figure 4.6: The temperature-dependent resistivity of Mn$_2$RhSn measured in 0 T, 0.13 T and 0.30 T. While cooling from the room temperature down to 2 K, the sample was first measured without magnetic field (black curve). Then, 0.13 T induction field was applied at 2 K and the resistivity was measured up to room temperature and back to 2 K (blue curve). The same procedure was repeated for a field of 0.30 T (red curve). Insets: enlarged view of the temperature-dependent resistivity and the resistivity hysteresis in the field of 0.30 T.

with a change of the slope at $T_C = 290$ K.

The low-temperature resistivity ($T \leq 110$ K) is described by the Bloch–Grüneisen equation [198, 199]:

$$\rho(T) = \rho(0) + \sum_n A_n \left(\frac{T}{\Theta}\right)^n \int\limits_0^{x=\frac{\Theta}{T}} \frac{x^n}{(e^x - 1)(1 - e^{-x})} dx \,, \tag{4.1}$$

where $\rho(0)$ is the residual resistivity, A_n are coefficients that depend on the underlying physical effects, T is the temperature, and Θ is the Debye temperature. The second, integral term is a sum over 3 different contributions with exponents $n = 2$, 3, and 5. Those correspond to the electron–electron (*e-e*), the *s-d* electron and the electron–phonon (*e-ph*) scattering. The *e-ph* interaction is the dominating mechanism, whereas *e*-*e* scattering becomes important at low temperature. The two contributions are comparable at about 90 K with a subsequent increase of the electron–electron scattering part with decreasing temperature. The *s*-*d* term has found to be six orders of magnitude smaller than the *e*-*e* or *e*-*ph* contributions and can be neglected. The existing phenomenology can barely explain all mechanisms that contribute to the temperature-dependent resistivity. The full temperature range cannot be sufficiently analyzed within the present model. The Debye temperature from a simple phonon density model is again a temperature-dependent quantity. It is derived as a fit parameter and listed in Table 4.2.

4.6 Magnetic and magnetotransport properties

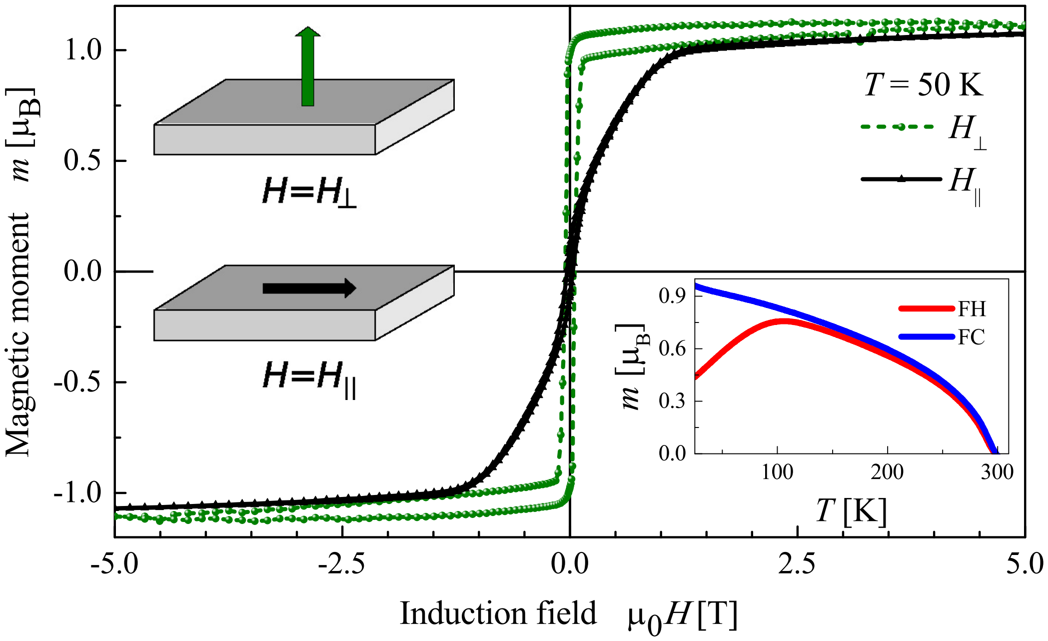

Figure 4.7: Magnetic properties of Mn_2RhSn thin films. Shown are the in–plane ($H_{\|}$) and out–of–plane ($H_{\perp}$) magnetic hysteresis loops measured at 50 K. The corresponding geometries are schematically shown. The inset shows the temperature dependence of the magnetization. The Curie temperature is about 290 K.

The magnetic properties of Mn_2RhSn thin films grown on MgO are shown in Fig. 4.7. The MgO substrate is diamagnetic, but may also contain random paramagnetic inclusions that slightly affect the overall magnetization signal in particular at low temperatures. The diamagnetic contribution of the MgO substrate has been subtracted from the magnetic moment measurements.

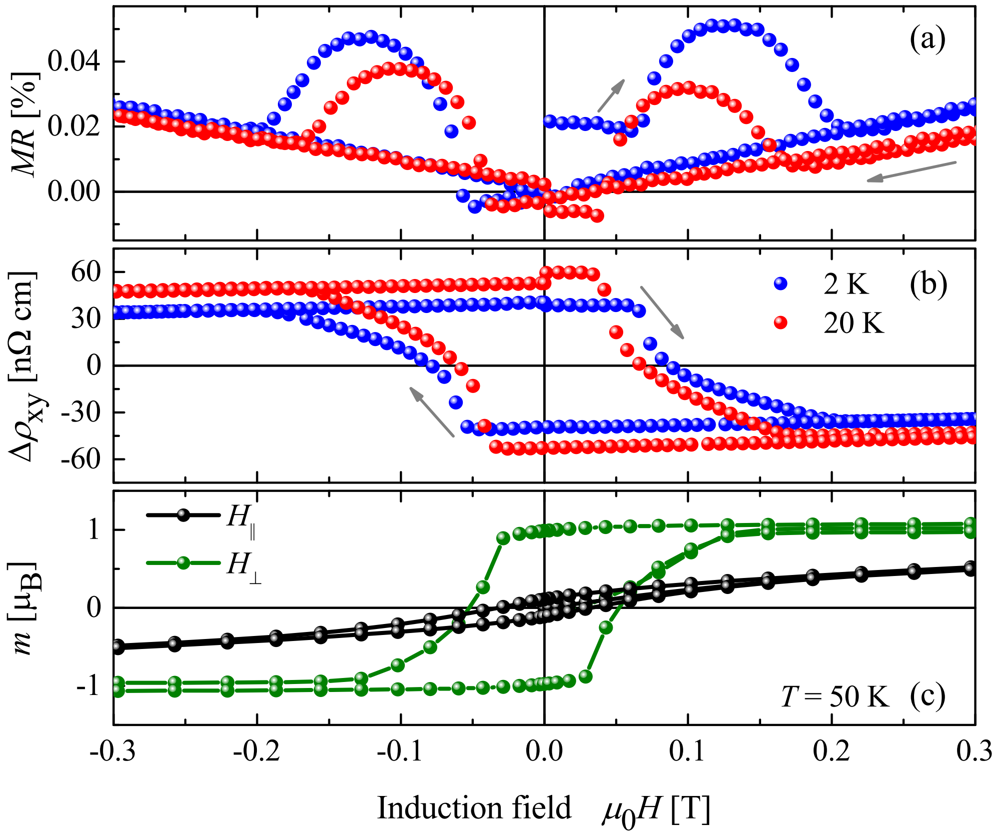

Figure 4.8: Magnetotransport of Mn_2RhSn. (a) Longitudinal magnetoresistance $MR(H_\perp)$ measured at 2 and 20 K. (b) The Hall resistance measured at the same temperatures. (c) Magnetisation measured at 50 K for in–plane ($H_\|$, black) and out–of–plane ($H_\perp$, green) geometry. The maximum energy product determined from the $H_\perp$ hysteresis amounts to $BH_{\max} = 45.3$ kJ/m^3.

The magnetization curves displayed in Fig. 4.7 reveal an out–of–plane easy axis. It is characterized by an anisotropy field of $H_K \approx 1.2$ T. This field corresponds to a moderate anisotropy energy of $H_K m_s \approx 0.18$ MJ/m^3. This value is by two orders of magnitude lower compared to the bulk anisotropy of ≈ 50 MJ/m^3 deduced from first principles calculations as an estimate of the *'upper' limit* [170]. The measured value for the film is reduced because of temperature effects or by dipole-dipole interactions that favor an in-plane orientation. Between 100 and 150 K the system undergoes a transition from a non-collinear into a collinear ferrimagnetic state. The system is magnetically soft with a coercive field of about 0.05 T (see Figure 4.8 (c)). The magnetization is $m_s \approx 1$ μ_B. Here, it is small due to the ferrimagnetic alignment of the magnetic moments. This allows to keep the out–of–plane anisotropy intact.

The coercive field for $H_{||}$ amounts to approximately 0.03 to 0.04 T and is comparable to that measured with $H_\perp$ (see Fig. 4.8). This may be a sign of a certain staggered component of magnetization, which resides in the film plane. It has two main origins. As it was shown earlier [170], the bulk magnetic structure is canted for $T < 50$ K. The first magnetic sublattice is aligned along the c-axis while the second sublattice is forced to tolerate two antiparallel couplings between the nearest and the next-nearest neighbors. Therefore the net total moment deviates from the c axis. This situation may also preserve in thin films. Another reason is the Dzyaloshinskii-Moriya interaction that gives rise to a long-range magnetic modulation. It is already present in the non-centrosymmetric bulk sample and may be amplified on the surface due to additional symmetry reduction. The temperature dependence of the magnetization (see inset in Fig. 4.7) reveals the T_C of 290 K. This is slightly higher compared to the bulk value of 270 K.

4.6.1 Magnetoresistance

An interesting behavior is observed for the transversal magnetoresistance $MR = (\rho_H - \rho_0)/\rho_0$, measured in $H_\perp$-mode (Fig. 4.8 (a)). It consists of positive, nearly linear dependencies superimposed with a pair of local maxima centered at around ±0.125 T at 2 K. The maxima shift down to smaller fields at higher temperatures. These maxima result from magnetic inhomogeneities such as propagating domain walls. The movement of the domain walls causes also the non-linear curvature of the hysteresis in Figure 4.8 (c). One observes the same trend in the anomalous Hall signal $\Delta\rho_{xy}$ (Fig. 4.8 (b)). $\rho_{xy}(H)$ is proportional to the magnetization, and changes its sign at about the coercive field. The anomalous Hall conductivity is $\sigma_{xy}^{AH} = \rho_{xy}/\rho_{xx}^2 = 310$ S/m at 2 K and zero field.

Fig. 4.9 shows the angular dependence of the magnetoresistance and Hall effect for high magnetic fields. The measurements are acquired with fields in the range of $\mu_0 H \lesssim 9$ T and with varying angle ($0 \leq \theta \leq 90°$) between external field and electric current. It is not necessary that the magnetization and the external field are parallel at low fields, due to remanently magnetized or virgin domains oriented along the easy direction. The non-linear contribution at $\mu_0 H \lesssim 1.5$ T to the magnetoresistance is anisotropic and ranges from about 1% at $\theta = 0$ ($H_{||}$) to 0 at $\theta = 90°$ ($H_{\perp}$). For a given θ ($\theta < 90°$) the anisotropic magnetoresistance (AMR) increases with field due to a rotation of the magnetization from perpendicular orientation (easy axis) towards the external field. The AMR saturates at about $\mu_0 H_{||} = 1.2$ T ($\theta = 0$). For $\mu_0 H \gg 1.2$ T, all localized electron orbits responsible for the magnetization are oriented perpendicular to the external field (and to the direction of electric current). This situation provides the maximal $s - d$ scattering cross-section for conduction electrons.

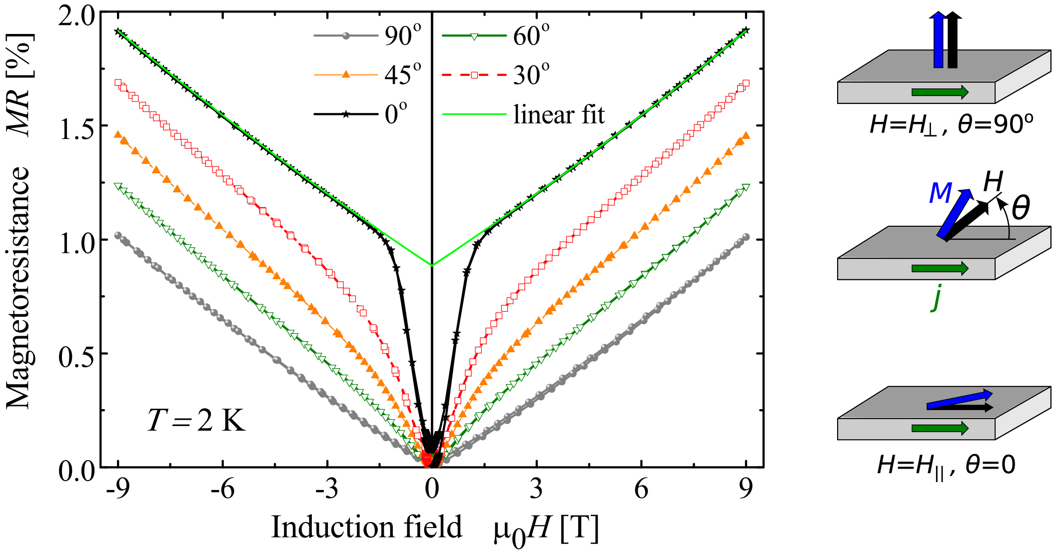

Figure 4.9: Magnetoresistance measured as function of applied magnetic field H at 2 K for different orientations $0 < \theta < 90°$ of the field with respect to the electric current. The relation between magnetization M, external field H, and current j is given in the sketches of the geometry.

The magnetoresistance behaves similar in the saturated part of the magnetization when the angle between field and current is varied. A detailed analysis reveals that the field dependence of the derivative of the magnetoresistance contains not only a

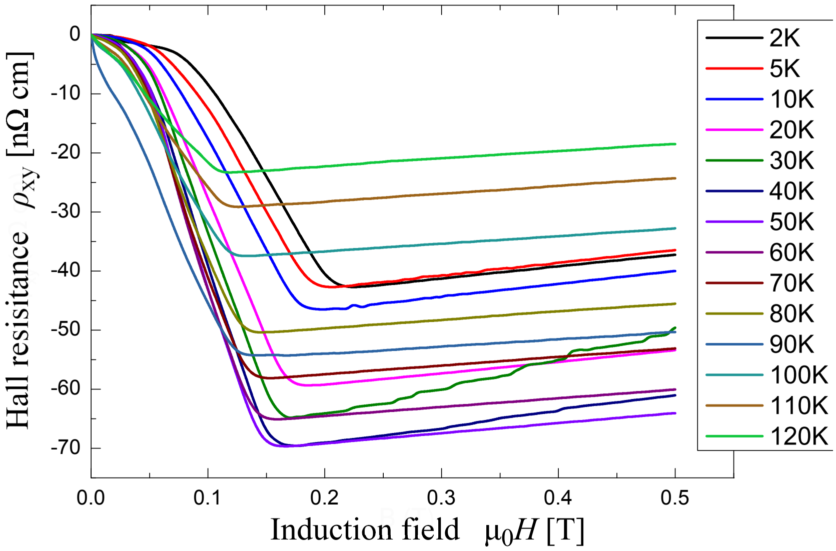

Figure 4.10: Hall resistance measured as function of applied magnetic field H and temperature T. The topological contribution is observed within the fields of $\mu_0 H = 0.1 - 0.2$ T and temperatures $T = 2 - 120$ K.

constant value but also a linear part. The linear part of the slope hints on a quadratic behavior for $H \gg H_c$. The quadratic part of the transverse magnetoresistance determined from the slope is given by $MR = 0.15 \times 10^{-3}\ \mathrm{T}^{-2} * (\mu_0 H_\perp)^2$ and of about the same order for the longitudinal magnetoresistance.

The longitudinal magnetoresistance ($H_\parallel$) behaves at low fields different from the transversal magnetoresistance. It increases strongly up to the saturation field of about 1.5 T, where it has a value of about 1%, as mentioned above. At higher fields it develops parallel to the transversal magnetoresistance. This means that the slopes of the field dependence are rather independent on the angle. The offset between low and high field behavior increases with decreasing angle.

4.6.2 Anomalous Hall effect

Materials with antiparallel alignment of their magnetic sublattices are known to exhibit topological Hall resistance when driven into the non-collinear phase [200]. In the ordinary conductor, the Hall voltage is measured transverse to the current in the perpendicularly applied magnetic field. The effect arises from the Lorenz force that

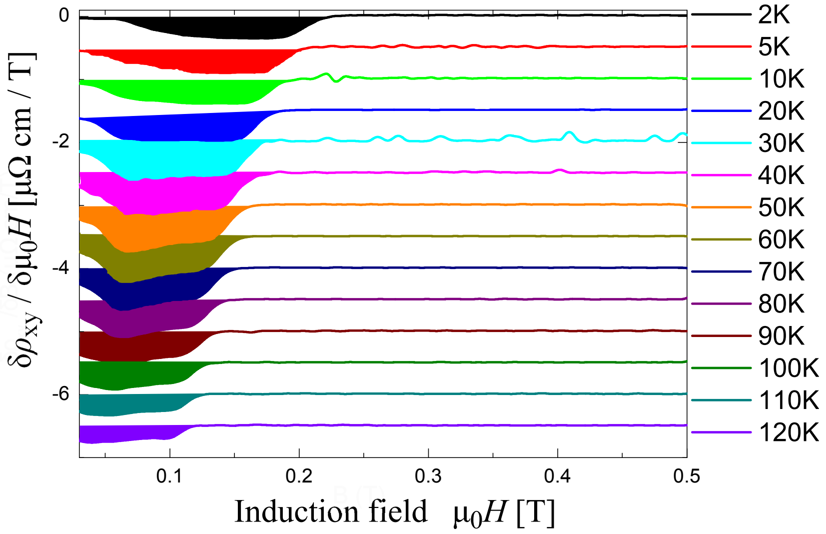

Figure 4.11: Magnetic-field-induced phase diagram of the non-collinearity in the thin film of Mn_2RhSn.

interacts with the charge carriers. The presence of an internal magnetism brings additional contributions to the Hall voltage. The so-called anomalous Hall effect arises in collinear spin structures due to the magnetization and spin-orbit coupling. The non-collinearity with a fixed sense of modulation can introduce a certain Berry phase, which in turn yields the topological contribution to the Hall effect (THE). In literature, the THE is attributed to the skyrmion phase of non-centrosymmetric B20 helimagnets [201, 202] or other non-trivial spin structures.

The field-dependent Hall resistance shows a non-linear behavior, which evolves with the temperature (see Fig. 4.10). In the low field regime $\mu_0 H \leq 0.2$ T the Hall resistance shows an enhancement of ρ_{xy}, which is attributed to the non-collinear spin structure. As the external field rises, the ρ_{xy} changes the slope and slowly increases without saturation, which corresponds to the collinear ferrimagnetic state. The difference of the resistivity signal $\rho_{xy}(H) - \rho_{xy}(0)$ gradually increases for the temperatures $T \leq 50$ K and then slowly drops as the temperature rises. The measurement of the ρ_{xy} allows to build a magnetic field induced phase diagram of the non-collinearity in Mn_2RhSn thin film (see Fig. 4.11). The first derivative of the signal with respect to the applied magnetic field reveals a pocket, which corresponds to the non-collinear magnetic state.

4.7 Spin reorientation in Mn_2RhSn by FMR

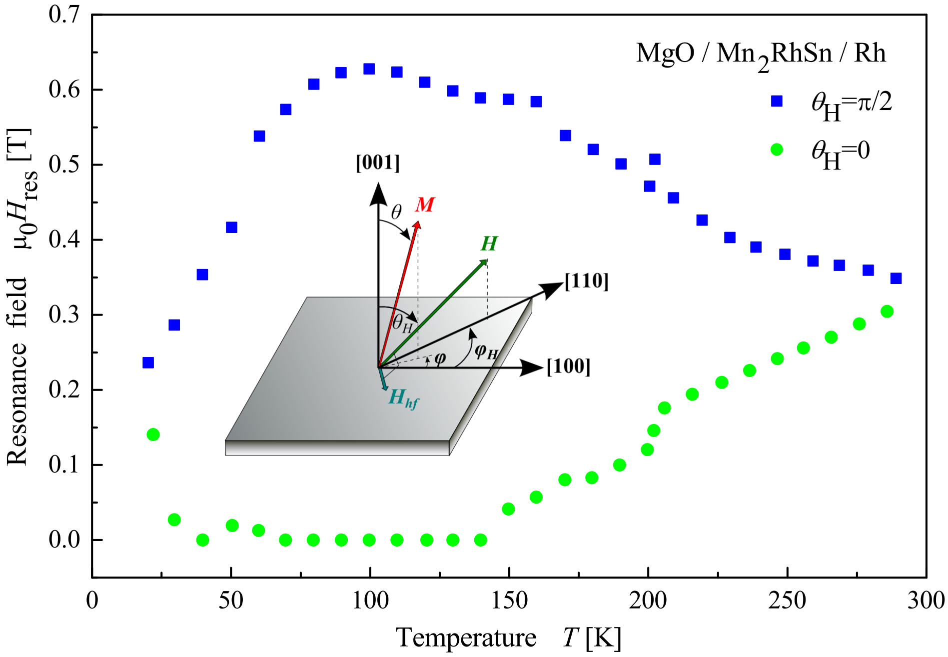

Figure 4.12: Temperature-dependent in-plane and out-of-plane FMR measurement of the Rh-capped Mn_2RhSn thin film. The resonance field values were obtained from the Lorentzian fit of the resonance line. Inset: Orientation of the film in the external magnetic field. The magnetization vector is defined by the polar and azimuthal angles θ and ϕ with respect to the crystallographic directions. Since the magnetization vector prefers an out-of-plane axis, the $\theta_H \geq \theta$. The high-frequency field $H_{hf} \perp H$ lies always in the film plane.

Mn_2RhSn has a noncollinear magnetic structure in the ground state and undergoes a spin reorientation transition in one of the Mn-sublattices at the elevated temperatures. Frequently, such phenomena have their origin in the temperature-dependent evolution of the effective magnetic anisotropy energy [203, 204, 205].

As of the random crystallite orientation, the crystallographic axes are not defined in a bulk policrystalline ingots. Therefore, single crystalline samples, preferably in the form of thin films, are inevitable. To probe the coupling of magnetization vector with the crystal directions, temperature and angle dependent ferromagnetic

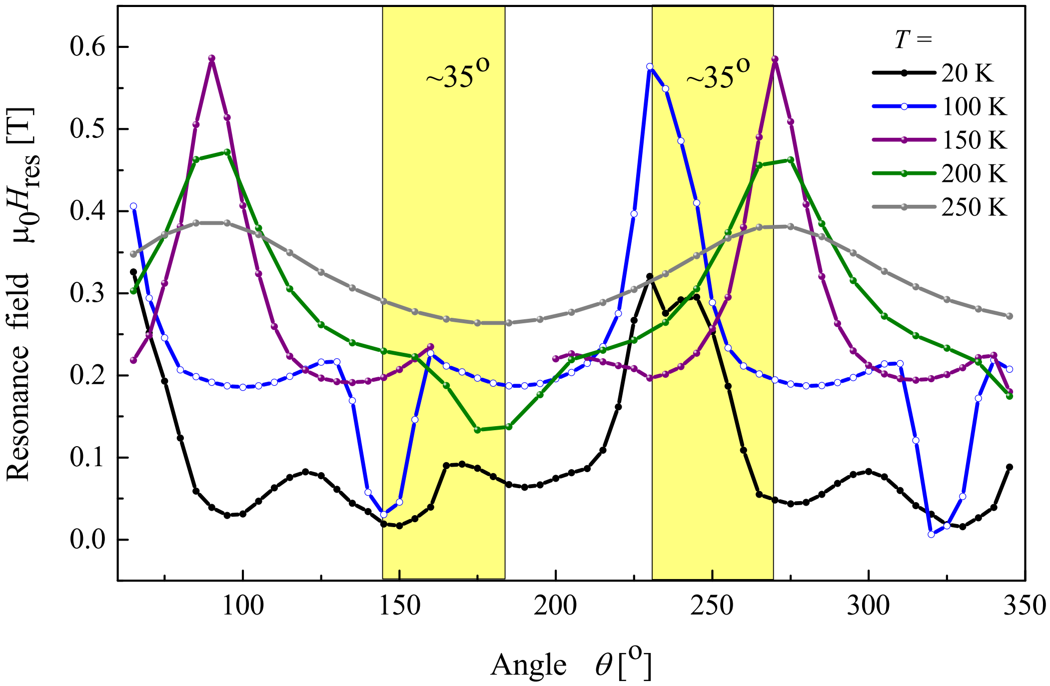

Figure 4.13: Angle and temperature-dependent FMR measurement of the Rh-capped Mn_2RhSn thin film. The resonance field values were obtained from the Lorentzian fit of the resonance line. $\theta = 90°$ and $\theta = 180°$ correspond to the in-plane and out-of-plane orientation of the film correspondingly.

resonance (FMR) spectroscopy [206, 207] can be used. Thin ferromagnetic layers are perfect sample form due to the (1) known shape and demagnetization factors (2) defined orientation of crystallographic axes and (3) small amount of a metallic material that is exposed to microwave radiation - while interacting with a metal, microwaves excite eddy curets that lead to the parasitic heat. One more condition is that (4) for the homogeneous excitation, the film thickness should be smaller than the microwave skin depth.

In a conventional setup, the sample is placed in the magnetic field, which creates the Zeeman splitting of energy levels. Simultaneously, the second alternating field of a fixed frequency is irradiating the sample, which excites the magnetic dipole transitions between the split Zeeman levels. The precession frequency of local magnetic moments is tuned by the external magnetic field; when it reaches the value of applied microwave frequency, the resonance condition is fulfilled and the microwave power is absorbed by the sample.

The temperature- and angular-dependent resonances were recorded from the room temperature down to 20 K by a commercially built setup using the frequency f=9.39603 GHz. To prevent the sample from the loosen rotation in the external field, the film was fixed with glue in a capillary. The resonance line was fit with a Lorentzian peak profile.

The free energy density of a film with tetragonal symmetry is written as [208]:

$$\begin{aligned} E = & -HM\left(\sin\theta\sin\theta_H\cos(\phi-\pi/4)+\cos\theta\cos\theta_H\right)+2\pi M^2\cos^2\theta- \\ - & \; K_U\cos^2\theta-\frac{1}{2}K_{1\perp}\cos^4\theta-\frac{1}{2}K_{1\|}\frac{1}{4}\left(3+\cos^4\phi\right)\sin^4\theta\,, \end{aligned} \tag{4.2}$$

where the first and the second terms correspond to the Zeeman and demagnetizing energy respectively; the perpendicular uniaxial anisotropy of the second and fourth orders is given by K_U and $K_{1\perp}$; the fourfold in-plane anisotropy is described by the $K_{1\|}$. For more details, see [209, 208]. The angles θ and θ_H are the polar angles from the film normal to the vectors of magnetization and applied field respectively. The azimuthal angles ϕ and ϕ_H are counted with respect to the [100] crystallographic direction (see the scheme on Fig. 4.13). When saturating the magnetization perpendicular to the film surface, the FMR condition is defined as [210]:

$$w_0=\gamma\sqrt{\left(H+(N_y-N_z)M\right)\left(H+(N_x-N_z)M\right)}\,, \tag{4.3}$$

with the demagnetization factors $N_x = N_z = 0$, $N_y = 4\pi$. The magnetization should be saturated to a single domain state. Minimizing the free energy density by the angle, the Eq. (4.2) can be simplified [211]

$$\begin{aligned} 2\pi f &= |\gamma|\sqrt{H_{\|}\left(H_{\|}+4\pi M_{\text{eff}}\right)}; \qquad \text{for } \theta_H=\pi/2 \\ 2\pi f &= |\gamma|\left(H_{\perp}-4\pi M_{\text{eff}}\right); \qquad \text{for } \theta_H=0 \end{aligned} \tag{4.4}$$

The fingerprints of a resonance phenomena in a ferromagnet are the shape and linewidth of an absorption spectrum, which contain the information about the magnetocrystalline anisotropy and the Gilbert damping parameter α. The latter is of an utmost interest recently due to its crucial significance for the memory technology and the fast magnetization switching process [109, 110, 212, 213].

The temperature-dependent FMR measurements (see Fig. 4.13, (a)) show a significant difference between the parallel and perpendicular orientation of the sample in the external magnetic field (see the sketch in Fig. 4.13, (b)). According to the hysteresis loops (see Fig. 4.7), the Mn_2RhSn thin film can be considered to have large magnetic domains. In the easy magnetization direction (out of the film plane), the magnetic moment becomes fast saturated already in small fields. In the opposite case of small magnetic domains, an antiferromagnetic interaction between them would work against the external magnetic field. Therefore, the saturation of magnetization would occur at the larger field values. For more details, see Fig. 5 (b, c) in the Ref. [214].

The resonance field position at $T = 250$ K proves the out-of-plane easy axis of magnetization by having its maximum at $\theta = 90°$ and minimum at $\theta = 180°$. At this temperature, the magnetic anisotropy is nearly vanished due to the approaching to the T_C. By lowering the temperature down to $T = 150$ K, the difference between the resonance field maxima and minima increases due to the rising anisotropy. At the temperature $T = 100$ K, the magnetization vector tilts for about 35°. Further, at $T = 20$ K two additional minima add as satellites in the vicinity of 150°. This might be explained by the canting in the Mn_{II} sublattice, known from the bulk studies.

4.8 Summary

Stoichiometric Mn_2RhSn thin films have been synthesized with high crystallinity order, as it is proved by the detailed XRD analysis. The composition ratio of Mn:Rh:Sn was confirmed to be 2:1:1 with help of the RBS technique. The phase stability is observed within a narrow composition range. A slight excess of Rh brings the structure to the cubic state while Rh deficiency leads to decomposition into tetragonal Mn_2RhSn and hexagonal Mn_3Sn (Mn_2Sn) phases. The valence band HAXPES spectra of the films are very similar to bulk spectra and agree very well with the density of states found in *ab-initio* calculations. In particular, details of maxima in the density of states are better resolved due to a higher crystalline order of the films. The thin Mn_2RhSn films exhibit a Curie temperature of 290 K that is about 20 K higher compared to bulk material. The determination of the magnetization reveals a soft magnetic behavior with perpendicular magnetic anisotropy. The anisotropy energy and the maximum energy product amount to $H_K m_s = 180$ kJ/m^3 and $BH_{\max} = 45.3$ kJ/m^3, respectively. The anomalous Hall conductivity has a value of $\sigma_A H = 310$ S/m at 2 K. A non-trivial behavior of the magnetoresistance is observed for fields below the coercive or saturation fields. The longitudinal and transversal magnetoresistance components are both positive and in the order of few percent for fields of up to 9 T. The magnetic-field-induced phase diagram of the non-collinearity in Mn_2RhSn is build based on the anomalous Hall resistance. The onset of the collinear ferrimagnetic phase is attributed to the change of magnetocrystalline anisotropy - the spin reorientation transition at the temperatures $T \geq 150$ K is revealed from the FMR studies.

5 Vector network analyzer ferromagnetic resonance (VNA-FMR) setup

The conventional FMR experiment can be upgraded by the additional degree of freedom [215, 216]. Together with the possibility of external field sweep, one can also sweep the excitation frequency in a broad range. The possibility of a simultaneous field-frequency variation allows to define the Gilbert damping - one of the key parameters for the ultrafast magnetization switching [109, 110, 212, 213].

The magnetization dynamics is well-described by the Landau-Lifshitz-Gilbert equation [217]:

$$\frac{\partial \mathbf{M}}{\partial t} = -\gamma \mathbf{M} \times \left(\mathbf{H}_{\mathrm{eff}} - \frac{\alpha}{\gamma M_{\mathrm{S}}} \frac{\partial \mathbf{M}}{\partial t} \right) = -\gamma \mathbf{M} \times \mathbf{H}_{\mathrm{eff}} + \frac{\alpha}{M_{\mathrm{S}}} \mathbf{M} \times \frac{\partial \mathbf{M}}{\partial t}\,, \tag{5.1}$$

where the first term corresponds to the excitation of the precession motion and the second term describes damping; $\mathbf{H}_{\mathrm{eff}}$ and $\mathbf{M}$ are the effective field and magnetization vectors, M_{S}, γ and α are the saturation magnetization, gyromagnetic ratio and the Gilbert damping constant respectively. The $\mathbf{H}_{\mathrm{eff}}$ is an integrated influence of the externally applied static and dynamic magnetic fields together with the internal fields induced by the magnetocrystalline, shape and magnetoelastic anisotropies. The effective damping parameter contains several contributions: the material-specific Gilber damping, two-magnon scattering process, scattering on the grain boundaries, etc. In general, it is directly proportional to the ratio of absorption linewidth ΔH and the resonance frequency f:

$$\alpha = \frac{\mu \gamma \Delta H}{4 \pi f}\,, \tag{5.2}$$

here γ is the gyromagnetic ratio. The first term is frequency-independent and results from the present magnetic inhomogeneities while the second term corresponds to the viscous damping.

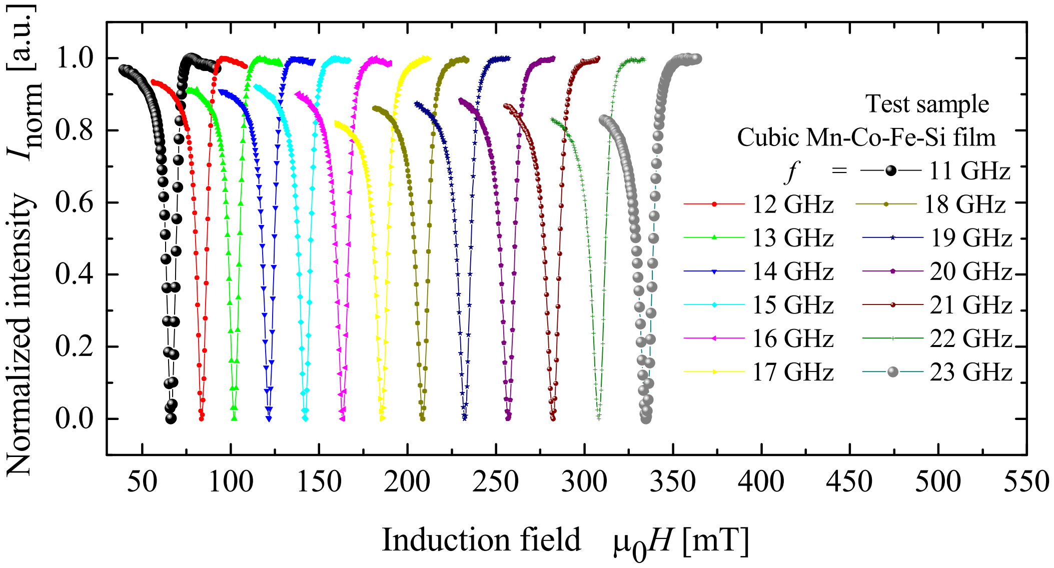

Figure 5.1: Shift of the absorption peak with the excitation frequency.

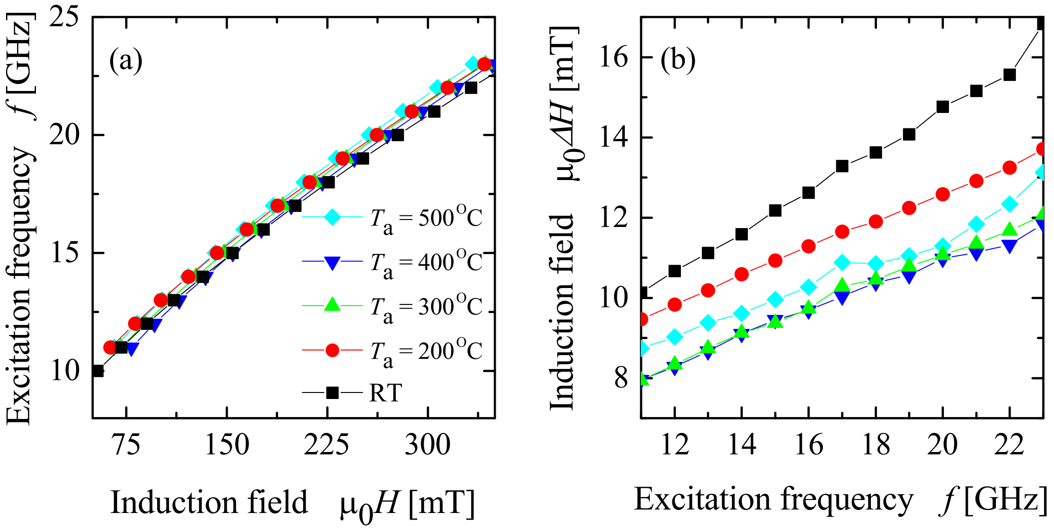

Figure 5.2: (a) Dependence of the resonance frequency as a function of external magnetic field. (b) Linewidth of the absorption spectra as a function of the resonance frequency.

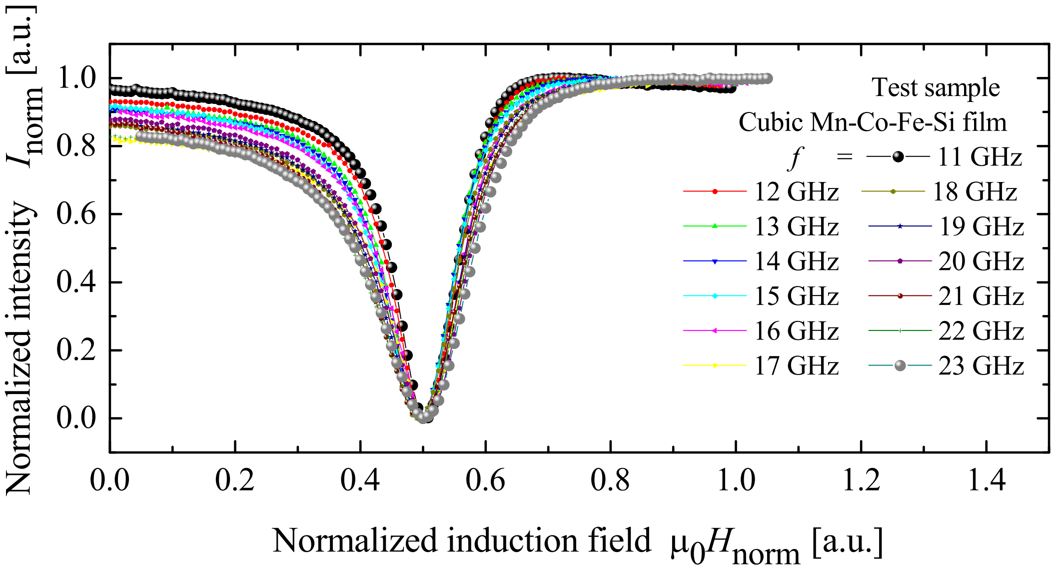

Figure 5.3: Evolution of the absorption peak profile with the excitation frequency. Annealing temperature of the sample $T_\mathrm{a} = 500°\mathrm{C}$.

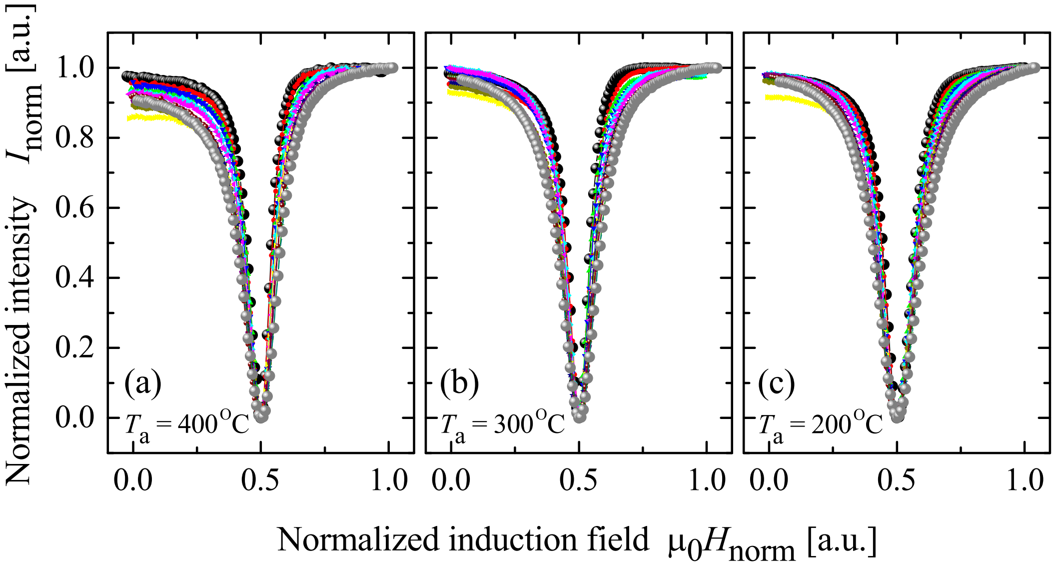

Figure 5.4: Evolution of the absorption peak profile with the excitation frequency. The asymmetry gradually reduces with the lowering of annealing temperature (a) $T_\mathrm{a} = 400°\mathrm{C}$, (b) $T_\mathrm{a} = 300°\mathrm{C}$ and (c) $T_\mathrm{a} = 200°\mathrm{C}$.

The VNA-FMR system consists of two major components: a controlled electromagnet for the field sweeps up to 350 mT and a commercial 2-port vector network analyzer ZVA40 Rhode&Schwarz, which generates and reads back the frequency-domain measurements in the range of 20 MHz - 40 GHz. The incoming signal is analyzed by the amplitude and phase and compared to the outgoing signal. Instead of a conventional resonator, the sample is placed on top of the coplanar wave guide (CPW) with a characteristic impedance of 50Ω. The radio-frequency signal of about 10 dB intensity is supplied to the CPW through the coaxial cables and non-magnetic microwave connectors. For the resonance condition, the H_{rf} field is perpendicular to H_{dc} field.

The FMR studies were carried out at the room temperature using the frequency f range of 8 GHz to 23 GHz. The microwave signal was supplied to the sample via a coplanar waveguide and detected back in a transmission mode. First, the sample was saturated in the high magnetic field driving the resonance peak beyond the investigated frequency window; a reference measurement was recorded. Then, for each frequency, magnetic field sweeps were performed; the data was obtained as a real and imaginary components of the transmitted microwave power through the sample. The data acquisition and treatment may employ various methods [216, 218], here the $\log Z_{\mathrm{step}}/Z_{\mathrm{ref}}$ formula was used, where $Z = \sqrt{S21_{\mathrm{Re}}^2 + S21_{\mathrm{Im}}^2}$, $S21_{\mathrm{Re}}$ and $S21_{\mathrm{Im}}$ are the real and imaginary parts of the transmitted microwave power in dB. Finally, the plotted absorption spectrum is a result of averaging over 201 measurement runs; the linewidth and the resonance field value were extracted from the Lorentz peak fit. To test the setup, a test specimen of Mn-Co-Fe-Si Heusler film was used (produced in Bielefeld by D. Ebke). The sample was annealed at 500°C, crystallizes in a cubic structure, is magnetically soft and has a thickness of about 50 nm (private communications). Before the measurement, the sample was saturated in the external field $H \geq H_{\mathrm{C}} = 500$ mT. Fig. 5.1 shows a typical resonance absorption line and its shift with increased excitation frequency. Fig. 5.3 shows the change of the peak shape at different excitation frequencies. A certain asymmetry is already present at the lowest frequency of $f = 11$ GHz, which increases and leads to the additional peak broadening at higher frequencies up to $f = 23$ GHz. For comparison, the samples of the same structure and composition but different annealing temperatures were measured (see Fig. 5.4). Surprisingly, the asymmetry reduces with the decrease of annealing temperature: at the $T_{\mathrm{a}} = 200$°C the peak broadening is rather symmetric. The origin of this effect is not yet understood and requires additional studies. The linear dependence of the resonance frequency (see Fig. 5.2, (a)) was fit according to the Kittel formula eq. (4.4). The slope well-correlates with the typical behavior of the Heusler films (e.g., see review [219]), the obtained values of α are 0.0074, 0.0069, 0.0074, 0.0074 and 0.0109 for the $T_\mathrm{a} = 500°\mathrm{C}$, $T_\mathrm{a} = 400°\mathrm{C}$, $T_\mathrm{a} = 300°\mathrm{C}$, $T_\mathrm{a} = 200°\mathrm{C}$ and the RT correspondingly. The damping phenomena can be composed of several contributions: excited magnons may relax to the lattice vibrations either directly or in steps trough the two-magnon, multiple magnon or magnon - conduction electron scattering processes [220]. The expression is given for the uniform excitation and might be questioned due to the finite size of the coplanar waveguide or inhomogeneous field excitation and resulting generation of spin waves. However, due to the negligible cause to the frequency shift this effect can be omitted [215].

6 Summary and outlook

The present work provides an insight into the emergent Mn_2-based Heusler materials. The establishment and evolution of canted ferrimagnetic spin arrangement in the novel Mn_2RhSn compound is shown experimentally and explained theoretically. In particular, the compound shows all necessary pre-conditions for the formation of the skyrmion phase: (1) a non-centrosymmetric crystal structure and a Dzyaloshinskii-Moriya (DM) interaction; (2) it contains a heavy transition metal element Rh, which enchances relativistic effects and the DM coupling and (3) shows two magnetic transitions. Based on the *ab-initio* calculations, the continuum model of the magnetic order in Mn_2RhSn suggests a formation of the skyrmion lattice in a collinear ferrimagnetic state ($T \geq 80$ K) with a skyrmion size of about 140 nm. In addition to the rich magnetic behavior, the Mn_2RhSn shows a structural transition into the cubic structure at the elevated temperatures. The gradual substitution of Rh with Co linearly reduces the transition temperature until the cuic phase is achieved already at the ambient conditions for the Co concentration $\geq 60\%$. Beside from the structural transition, the Co-doping linearly increases T_C, Sommwrfeld coefficient of the electronic heat capacity and reduces the lattice mismatch with the MgO, which makes the $Mn_2Rh_{1-x}Co_xSn$ series potential candidates for the spintronic applications.

Inspired by the measurements on the bulk sample, thin films of the same composition were successfully fabricated for the electronic, magnetotransport and magnetocrystalline anisotropy studies. The stoichiometry of Mn_2RhSn composition was fully optimized by XRD and later proved by the RBS. The films show the $T_\mathrm{C} = 290$ K, which is higher than in case of the bulk samples and a perpendicular magnetic anisotropy in the ground state. The anisotropy energy and the maximum energy product amount to $H_K m_s = 180$ kJ/m^3 and $\mathrm{BH}_\mathrm{max} = 45.3$ kJ/m^3, respectively. The anomalous Hall conductivity has a value of $\sigma_A H = 310$ S/m at 2 K. A non-trivial behavior of the magnetoresistance is observed for fields below the coercive or saturation fields. The longitudinal and transversal magnetoresistance components are both positive and in the order of few percent for fields of up to 9 T.

As an outlook for future studies, the single crystal growth is inevitable for the small-angle neutron scattering and magnetotransport measurements.

Bibliography

[1] T. Moriya and Y. Takahashi. Itinerant electron magnetism. *Annu. Rev. Mater. Sci.*, 14(1):1, 1984.

[2] W. Heisenberg. Zur Theorie des Ferromagnetismus. *Z. Phys.*, 49(9-10):619, 1928.

[3] J. Frenkel and J. Doefman. Spontaneous and induced magnetisation in ferromagnetic bodies. *Nature*, 126:274, 1930.

[4] M.A. Ruderman and C. Kittel. Indirect exchange coupling of nuclear magnetic moments by conduction electrons. *Phys. Rev.*, 96:99, 1954.

[5] T. Kasuya. A theory of metallic ferro- and antiferromagnetism on Zener's model. *Prog. Theor. Phys.*, 16(1):45, 1956.

[6] K. Yosida. Magnetic properties of Cu-Mn alloys. *Phys. Rev.*, 106:893, 1957.

[7] J.H. Van Vleck. Note on the interactions between the spins of magnetic ions or nuclei in metals. *Rev. Mod. Phys.*, 34:681, 1962.

[8] H.A Kramers. L'interaction entre les atomes magnétogènes dans un cristal paramagnétique. *Physica*, 1:182, 1934.

[9] P.W. Anderson. Antiferromagnetism. Theory of Superexchange Interaction. *Phys. Rev.*, 79:350, 1950.

[10] J.H. Van Vleck. Theory of the variations in paramagnetic anisotropy among different salts of the iron group. *Phys. Rev.*, 41:208, 1932.

[11] F. Bloch. Zur Theorie des Austauschproblems und der Remanenzerscheinung der Ferromagnetika. *Z. Phys.*, 74(5-6):295, 1932.

[12] L. Landau and E. Lifshitz. On the theory of the dispersion of magnetic permeability in ferromagnetic bodies. *Phys. Z. Sowjetunion*, 8:153, 1935.

[13] L. Néel. Some new results on antiferromagnetism and ferromagnetism. *Rev. Mod. Phys.*, 25:58, 1953.

[14] A.S. Borovik-Romanov and M.P. Orlova. *Zh. Eksp. Teor. Fiz.*, 31:579, 1956.

[15] I.E. Dzyaloshinskii. Thermodynamic theory of weak ferromagnetism in antiferromagnetic substances. *Sov. Phys. JETP*, 5 (6):1259, 1957.

[16] I. Dzyaloshinskii. A thermodynamic theory of 'weak' ferromagnetism of antiferromagnetics. *J. Phys. Chem. Solids*, 4(4):241, 1958.

[17] T. Moriya. Anisotropic superexchange interaction and weak ferromagnetism. *Phys. Rev.*, 120:91, 1960.

[18] L.D. Landau and E.M. Lifshitz. *Course of Theoretical Physics.* Pergamon Press, 1980.

[19] J. Kübler and K.-H. Hock and J. Sticht and A.R. Williams. Density functional theory of non-collinear magnetism. *J. Phys. F: Metal Physics*, 18(3):469, 1988.

[20] J. Sticht and K.-H. Höck and J. Kübler. Non-collinear itinerant magnetism: the case of Mn_3Sn. *J. Phys.: Condens. Matter*, 1(43):8155, 1989.

[21] P.J. Brown, V. Nunez, F. Tasset, J.B. Forsyth, and P. Radhakrishna. Determination of the magnetic structure of Mn_3Sn using generalized neutron polarization analysis. *J. Phys.: Condens. Matter*, 2(47):9409, 1990.

[22] L. Keller, A. Dönni, H. Kitazawa, and B. van den Brandt. Geometrical frustration and incommensurate magnetic ordering in cepdal: a low-temperature neutron-diffraction study. *App. Phys. A: Mater. Sci. Process.*, 74:s686, 2002.

[23] H. Tanaka, T. Ono, S. Maruyama, S. Teraoka, K. Nagata, H. Ohta, S. Okubo, S. Kimura, T. Kambe, H. Nojiri, and M. Motokawa. Electron spin resonance in triangular antiferromagnets. *Journal of the Physical Society of Japan*, 72SB(Supplement B):84, 2003.

[24] I. Syôzi. Statistics of Kagomé lattice. *Prog. Theor. Phys.*, VI, 1951.

[25] A. Keren and P. Mendels and M. Horvatić and F. Ferrer and Y.J. Uemura and M. Mekata and T. Asano. ^{69,71}Ga NMR in the Kagomé lattice compound $SrCr_{9-x}Ga_{3+x}O_{19}$. *Phys. Rev. B*, 57:10745, 1998.

[26] J.L. Atwood. Kagomé lattice: A molecular toolkit for magnetism. *Nat. Mater.*, 1:91, 2002.

[27] S. Chu and T.M. McQueen and R. Chisnell and D.E. Freedman and P. Müller and Y.S. Lee and D.G. Nocera. A Cu^{2+}($S = 1/2$ Kagomé antiferromagnet: $Mg_xCu_{4-x}(OH)_6Cl_2$. *J. Am. Chem. Soc.*, 132:5570, 2010.

[28] S. Yan, D.A. Huse, and S.R. White. Spin-liquid ground state of the S = 1/2 Kagomé Heisenberg antiferromagnet. *Science*, 332:1173, 2011.

[29] A.H. Morrish. *Canted Antiferromagnetism: Hematite.* World Scientific, Singapore, 1994.

[30] S.P. Sellers, B.J. Korte, J.P. Fitzgerald, W.M. Reiff, and G.T. Yee. Canted ferromagnetism and other magnetic phenomena in square-planar, neutral Manganese(II) and Iron(II) Octaethyltetraazaporphyrins. *J. Am. Chem. Soc.*, 120:4662, 1998.

[31] K. Nakamura and J. Freeman. Canted ferromagnetism in $RuSr_2GdCu_2O_8$. *Phys. Rev. B*, 66:140405, 2002.

[32] D. Hobbs and J. Hafner. Noncollinear magnetism. *MCFA Annals*, IV, 2005.

[33] G. Bihlmayer. *Non-collinear magnetism: Exchange parameter and* T_C, chapter Computational Nanoscience: Do It Yourself, pages 447–467. John von Neumann Institute for Computing, 2006.

[34] G. Bouzerar, R. Bouzerar, and O. Cépas. Superexchange induced canted ferromagnetism in dilute magnets. *Phys. Rev. B*, 76:144419, 2007.

[35] S.T. Bramwell and M.J.P. Gingras. Spin ice state in frustrated magnetic pyrochlore materials. *Science*, 294:1495, 2001.

[36] C. Castelnovo, R. Moessner, and S.L. Sondhi. Magnetic monopoles in spin ice. *Nature*, 451:42, 2008.

[37] B. Klemke. *Thermal properties of Dysprosium-Titanate in the spin ice state.* PhD thesis, Technische Universität Berlin, 2011.

[38] C. Nisoli, R. Moessner, and P. Schiffer. *C*olloquium: Artficial spin ice: Designing and imaging magnetic frustration. *Rev. Mod. Phys.*, 85:1473, 2013.

[39] L. Bovo, X. Moya, D. Prabhakaran, Y.A. Soh, A.T. Boothroyd, N.D. Mathur, G. Aeppli, and S.T. Bramwell. Restoration of the third law in spin ice thin films. *Nat. Commun.*, 5:1, 2014.

[40] A. Herpin and P. Meriel. Etude de l'antiferromagnétisme hélicoidal de $MnAu_2$ par diffraction de neutrons. *J. Phys. Radium*, 22:337, 1961.

[41] Yu.A. Izyumov. Modulated, or long-periodic, magnetic structures of crystals. *Sov. Phys. Usp*, 27:845, 1984.

[42] I. Urcelay-Olabarria, E. Ressouche, A.A. Mukhin, V.Yu. Ivanov, A.M. Balbashov, J.L. García-Mu noz, and V. Skumryev. Conical antiferromagnetic order in the ferroelectric phase of $Mn_{0.8}Co_{0.2}WO_4$ resulting from the competition between collinear and cycloidal structures. *Phys. Rev. B*, 85:224419, 2012.

[43] K. Motoya, H. Yasuoka, Y. Nakamura, and J.H. Wernick. Helical spin structure in MnSi - NMR studies. *Solid State Commun.*, 19(6):529, 1976.

[44] P. Nordblad. The 3d Ising spin glass. *Brazilian Journal of Physics*, 30:762, 2000.

[45] C.A.M. Mulder, A.J. van Duyneveldt, and J.A. Mydosh. Susceptibility of the CuMn spin-glass: Frequency and field dependences. *Phys. Rev. B*, 23:1384, 1981.

[46] G.J. Nieuwenhuys, H. Stocker, B.H. Verbeek, and J.A. Mydosh. Differential susceptibility of spin glass - ferromagnetic systems. *Solid State Communications*, 27(3):197, 1978.

[47] I.E. Dzyaloshinskii. *Zh. Eksp. Teor. Fiz.*, 47:992, 1964.

[48] I.E. Dzyaloshinskii. Theory of helicoidal structures in antiferromagnets. *JETP*, 20:665, 1965.

[49] A.N. Bogdanov, U.K. Rößler, M. Wolf, and K.-H. Müller. Magnetic structures and reorientation transitions in noncentrosymmetric uniaxial antiferromagnets. *Phys. Rev. B*, 66:214410, 2002.

[50] V.G. Bar'yakhtar, A.N. Bogdanov, and D.A. Yablonskii. The physics of magnetic domains. *Phys. Usp.*, 31(9):810, 1988.

[51] L.J. de Jongh and A.R. Miedema. Experiments on simple magnetic model systems. *Adv. Phys.*, 23(1):1, 1974.

[52] A.S. Borovik-Romanov and M.P. Orlova. Magnetic properties of cobalt and manganese carbonates. *Soviet Physics JETP*, 4:531, 1957.

[53] K.P. Belov, A.K. Zvezdin, A.M. Kadomtseva, and R.Z. Levitin. Spin-reorientation transitions in rare-earth magnets. *Phys. Usp.*, 19:574, 1976.

[54] V. Skumryev, F. Ott, J.M.D. Coey, A. Anane, J.-P. Renard, L. Pinsard-Gaudart, and A. Revcolevschi. Weak ferromagnetism in $LaMnO_3$. *EPJ. B*, 11:401, 1999.

[55] M.C. Guidi, G. Allodi R. Renzi, G. Guidi, M. Hennion, L. Pinsard, and A. Amato. Staggered magnetization, critical behavior, and weak ferromagnetic properties of $LaMnO_3$ by muon spin rotation. *Phys. Rev. B*, 64:064414, 2001.

[56] Y. Shapira. Ultrasonic behavior near the spin-flop transitions of Hematite. *Phys. Rev.*, 184:589, 1969.

[57] Q.A. Pankhurst, C.E. Johnson, and M.F. Thomas. A Mössbauer study of magnetic phase transitions in alpha -Fe_2O_3 crystals. *J. Phys. C: Solid State Physics*, 19:7081, 1986.

[58] J. Baruchel. X-ray and neutron topographical studies of magnetic materials. *Phys. B: Condensed Matter*, 192:79, 1993.

[59] Y. Isikawa, K. Tajima, D. Bloch, and M. Roth. Helical spin structure in manganese silicide MnSi. *Solid State Commun.*, 19:525, 1976.

[60] Y. Xiao, Y. Su, W. Schmidt, K. Schmalzl, C. M.N. Kumar, S. Price, T. Chatterji, R. Mittal, L. J. Chang, S. Nandi, N. Kumar, S.K. Dhar, A. Thamizhavel, and Th. Brueckel. Field-induced spin reorientation and giant spin-lattice coupling in $EuFe_2As_2$. *Phys. Rev. B*, 81:220406, 2010.

[61] G.W. Durbin, C.E. Johnson, and M.F. Thomas. Direct observation of field-induced spin reorientation in $YFeO_3$ by the Mössbauer effect. *J. Phys. C: Solid State Physics*, 8(18):3051, 1975.

[62] G.W. Durbin, C.E. Johnson, and M.F. Thomas. Temperature dependence of field-induced spin reorientation in $GdFeO_3$. *J. Phys. C: Solid State Physics*, 10:1975, 1977.

[63] L.A. Prelorendjo, C.E. Johnson, M.F. Thomas, and B.M. Wanklyn. Spin reorientation transitions in $DyFeO_3$ induced by magnetic fields. *J. Phys. C: Solid State Physics*, 13:2567, 1980.

[64] A.M. Kadomtseva, Y.F. Popov, G.P. Vorob'ev, K.I. Kamilov, P.N. Makhov, M.M. Tehranchi, and A. Phirouznia. Induced by magnetic field spin reorientation in YMn_2O_5. *Phys. B: Condensed Matter*, 329-333, Part 2:856, 2003.

[65] Y.T. Millev, H.P. Oepen, and J. Kirschner. Influence of external fields on spin reorientation transitions in uniaxial ferromagnets. II. Ultrathin ferromagnetic films. *Phys. Rev. B*, 57:5848, 1998.

[66] B.F. Miao, Y.T. Millev, L. Sun, B. You, W. Zhang, and H.F. Ding. Thickness-driven spin reorientation transition in ultrathin films. *Sci. China. Phys. Mech. Astron.*, 56:70, 2013.

[67] H. Hornet and C.M. Varma. Nature of spin-reorientation transitions. *Phys. Rev. Lett.*, 20:845, 1968.

[68] B. Antonini and P. Paroli. First experimental verification of the Landau-like theory of spin reorientations. *Lettere Al Nuovo Cimento Series 2*, 40(14):422, 1984.

[69] F.J. Darnell, W.H. Cloud, and H.S. Jarrett. X-Ray and Magnetization Studies of Cr-Modified Mn_2Sb. *Phys. Rev.*, 130:647, 1963.

[70] A. Zheludev, G. Shirane Y. Sasago, N. Kiode, and K. Uchinokura. Spiral phase and spin waves in the quasi-two-dimensional antiferromagnet $Ba_2CuGe_2O_7$. *Phys. Rev. B*, 54:15163, 1996.

[71] A. Zheludev, S. Maslov, G. Shirane, Y. Sasago, N. Koide, K. Uchinokura, D.A. Tennant, and S.E. Nagler. Square-lattice spiral magnet $Ba_2CuGe_2O_7$ in an in-plane magnetic field. *Phys. Rev. B*, 56:14006, 1997.

[72] A. Zheludev, S. Maslov, G. Shirane, Y. Sasago, N. Koide, and K. Uchinokura. Field-induced commensurate-incommensurate phase transition in a Dzyaloshinskii-Moriya spiral antiferromagnet. *Phys. Rev. Lett.*, 78:4857, 1997.

[73] M.D. Lumsden, B.C. Sales, D. Mandrus, S.E. Nagler, and J.R. Thompson. Weak ferromagnetism and field-induced spin reorientation in $K_2V_3O_8$. *Phys. Rev. L*, 86:159, 2001.

[74] W. C. Koehler. Neutron diffraction by helical spin structures. *J. Appl. Phys.*, 32:S20, 1961.

[75] C. Wilkinson, F. Sinclair, and J.B. Forsyth. Neutron scattering from cubic FeGe powder. In *5th Int. Conf. on Solid Compounds of Transition Elements, Uppsala, Sweden*, 1976.

[76] B. Lebech, J. Bernhard, and T. Freltoft. Magnetic structures of cubic FeGe studied by small-angle neutron scattering. *J. Phys.: Condens. Matter*, 1:6105, 1989.

[77] S. Mühlbauer, B. Binz, F. Jonietz, C. Pfleiderer, A. Rosch, A. Neubauer, R. Georgii, and P. Böni. Skyrmion lattice in a chiral magnet. *Science*, 323(5916):915, 2009.

[78] F. Jonietz, S. Mühlbauer, C. Pfleiderer, A. Neubauer, W. Münzer, A. Bauer, T. Adams, R. Georgii, P. Böni, R. A. Duine, K. Everschor, M. Garst, and A. Rosch. Spin transfer torques in MnSi at ultralow current densities. *Science*, 330(6011):1648, 2010.

[79] R. Wäppling and L. Häggström. Mössbauer study of cubic FeGe. *Phys. Lett. A*, 28(3):173, 1968.

[80] S. Martynov. The incommensurate magnetic structure of a tetragonal antiferromagnet with antisymmetric exchange. *J. Exp. Theor. Phys.*, 109:979, 2009.

[81] A.N. Bogdanov and D.A. Yablonskii. Thermodynamically stable ”vortices” in magnetically ordered crystals. The mixed state of magnets. *Sov. Phys. JETP*, 68:101, 1989.

[82] W. Heisenberg. *Einführung in die einheitliche Feldtheorie der Elementarteilchen.* Stuttgart: Hirzel, 1969.

[83] T.H.R. Skyrme. A non-linear field theory. *Proc. R. Soc. Lond. Ser. A*, 260:127, 1961.

[84] R. Durrer, M. Kunz, and A. Melchiorri. Cosmic structure formation with topological defects. *Phys. Rep.*, 364:1, 2002.

[85] C. Bäuerle, Yu.M. Bunkov, S.N. Fischer, H. Godfrin, and G.R. Picket. Laboratory simulation of cosmic string formation in the early Universe using superfluid ^{3}He. *Nature*, 382:332, 1996.

[86] L. Brey, H.A. Fertig, R. Cote, and A.H. MacDonald. Skyrme crystal in a two-deminsional electron gas. *Phys. Rev. Lett.*, 75:2562, 1995.

[87] U. Al’Khawaja and H.T.C. Stoof. Skyrmions in a ferromagnetic Bose-Einstein condensate. *Nature*, 411:918, 2001.

[88] M.C. Cross and P.C. Hohenberg. Pattern formation outside of equilibrium. *Rev. Mod. Phys.*, 65:852, 1993.

[89] S.L. Sondhi, A. Karlhede, S.A. Kivelson, and E.H. Rezayi. Skyrmions and the crossover from the integer to the fractional quantum Hall effect at small Zeeman energies. *Phys. Rev. B*, 47:16419, 1993.

[90] D.C. Wright and N.D. Mermin. Crystalline liquids - the blue phases. *Rev. Mod. Phys.*, 61:385, 1989.

[91] U.K. Rößler, A.N. Bogdanov, and C. Pfleiderer. Spontaneous skyrmion ground states in magnetic metals. *Nature*, 442:797, 2006.

[92] X.Z. Yu, Y. Onose, N. Kanazawa, J.H. Park, J.H. Han, Y. Matsui, N. Nagaosa, and Y. Tokura. Real-space observation of a two-dimensional skyrmion crystal. *Nature*, 465:901, 2010.

[93] X.Z. Yu, N. Kanazawa, Y. Onose, K. Kimoto, W.Z. Zhang, S. Ishiwata, Y. Matsui, and Y. Tokura. Near room-temperature formation of a skyrmion crystal in thin-films of the helimagnet FeGe. *Nat. Mater.*, 10:106, 2011.

[94] S. Heinze, K. von Bergmann, M. Menzel, J. Brede, A. Kubetzka, R. Wiesendanger, G. Bihlmayer, and S. Blügel. Spontaneous atomic-scale magnetic skyrmion lattice in two dimensions. *Nat. Phys.*, 7:713, 2011.

[95] N. Romming, C. Hanneken, M. Menzel, J.E. Bickel, B. Wolter, K. von Bergmann, A. Kubetzka, and R. Wiesendanger. Writing and deleting single magnetic skyrmions. *Science*, 341:636, 2013.

[96] F. Heusler. Über magnetische Manganlegierungen. *Verhandlungen der Deutschen Physikalischen Gesellschaft*, 12:219, 1903.

[97] A.J. Bradley and J.W. Rodgers. The crystal structure of the heusler alloys. *Proc. R. Soc. Lond. A*, 144:340, 1934.

[98] K. Inomata, N. Ikeda, N. Tezuka, R. Goto, S. Sugimoto, M. Wojcik, and E. Jedryka. Highly spin-polarized materials and devices for spintronics. *Sci. Technol. Adv. Mater.*, 9:014101, 2008.

[99] I. Galanakis, P. H. Dederichs, and N. Papanikolaou. Slater-pauling behavior and origin of the half-metallicity of the full-heusler alloys. *Phys. Rev. B*, 66:174429, 2002.

[100] R.A. de Groot, F.M. Mueller, P.G. van Engen, and K.H.J. Buschow. New Class of Materials: Half-Metallic Ferromagnets. *Phys. Rev. Lett.*, 50:2024, 1983.

[101] J. Kübler, A.R. William, and C.B. Sommers. Formation and coupling of magnetic moments in heusler alloys. *Phys. Rev. B*, 28:1745, 1983.

[102] R.A. de Groot. Half-metallic magnetism in the 1990s. *Physica B*, 172:45, 1991.

[103] J. C. Slater. The ferromagnetism of nickel. *Phys. Rev.*, 49:537, 1936.

[104] L. Pauling. The nature of the interatomic forces in metals. *Phys. Rev.*, 54:899, 1938.

[105] K. Inomata, S. Okamura, and N. Tezuka. Tunnel magnetoresistance using full-Heusler alloys. *J. Magn. Magn. Mater.*, 282:269, 2004.

[106] H. Liu, Y. Honda, T. Taira, K. Matsuda, M. Arita, T. Uemura, and M. Yamamoto. Giant tunneling magnetoresistance in epitaxial $Co_2MnSi/MgO/Co_2MnSi$ magnetic tunnel junctions by half-metallicity of Co_2MnSi and coherent tunneling. *Appl. Phys. Lett.*, 101:132418, 2012.

[107] J. Kübler, G.H. Fecher, and C. Felser. Understanding the trend in the Curie temperatures of Co_2-based Heusler compounds: *Ab initio* calculations. *Phys. Rev. B*, 76:024414, 2007.

[108] S. Wurmehl, G.H. Fecher, H.C. Kandpal, V. Ksenofontov, C. Felser, and H.-J. Lin. Investigation of Co_2FeSi: The Heusler compound with highest Curie temperature and magnetic moment. *Appl. Phys. Lett.*, 88:032503, 2006.

[109] J.C. Slonczewski. Current-driven excitation of magnetic multilayers. *J. Magn. Magn. Mater.*, 159, 1996.

[110] L. Berger. Emission of spin waves by a magnetic multilayer traversed by a current. *Phys. Rev. B*, 54:9353, 1996.

[111] B. Balke, G.H. Fecher, J. Winterlik, and C. Felser. Mn_3Ga, a compensated ferrimagnet with high Curie temperature and low magnetic moment for spin torque transfer applications. *Appl. Phys. Lett.*, 90(15):152504, 2007.

[112] V. Alijani, J. Winterlik, G.H. Fecher, and C. Felser. Tuning the magnetism of the Heusler alloys $Mn_{3-x}Co_xGa$ from soft and half-metallic to hard-magnetic for spin-transfer torque applications. *Appl. Phys. Lett.*, 99:222510, 2011.

[113] S. Chadov, J. Kiss, and C. Felser. Improving spin-transport by disorder. *Adv. Funct. Mater.*, 23:832, 2013.

[114] F. Wu, S. Mizukami, D. Watanabe, H. Naganuma, M. Oogane, Y. Ando, and T. Miyazaki. Epitaxial $Mn_{2.5}Ga$ thin flms with giant perpendicular magnetic anisotropy for spintronic devices. *Appl. Phys Lett.*, 94:122503, 2009.

[115] S. Mizukami, F. Wu, A. Sakuma, J. Walowski, D. Watanabe, T. Kubota, X. Zhang, H. Naganuma, M. Oogane, Y. Ando, and T. Miyazaki. Long-lived ultrafast spin precession in Manganese alloys films with a largeperpendicular magnetic anisotropy. *Phys. Rev. Lett.*, 106:117201, 2011.

[116] S. Ouardi, T. Kubota, G.H. Fecher, R. Stinshoff, S. Mizukami, T. Miyazaki, E. Ikenaga, and C. Felser. Stoichiometry dependent phase transition in Mn-Co-Ga-based thin films: From cubic in-plane, soft magnetized to tetragonal perpendicular, hard magnetized. *Appl. Phys. Lett.*, 2012:242406.

[117] P. Baláž, M. Gmitra, and J. Barnaś. Current-induced dynamics in noncollinear dual spin valves. *Phys. Rev. B*, 80:174404, 2009.

[118] Yoshio Miura, Kazutaka Abe, and Masafumi Shirai. Effects of interfacial noncollinear magnetic structures on spin-dependent conductance in $Co_2MnSi/MgO/Co_2MnSi$ magnetic tunnel junctions: A first-principles study. *Phys. Rev. B*, 83:214411, 2011.

[119] A. Soncini and L.F. Chibotaru. Molecular spintronics using noncollinear magnetic molecules. *Phys. Rev. B*, 81:132403, 2010.

[120] N.L. Chung, M.B.A. Jalil, S.G. Tan, J. Guo, and S.B. Kumar. A study of spin relaxation on spin transfer switching of a noncollinear magnetic multilayer structure. *J. Appl. Phys.*, 104:084502, 2008.

[121] Y.F. Tian, J.F. Ding, W.N. Lin, Z.H. Chen, A. David, M. He, W.J. Hu, L. Chen, and T. Wu. Anomalous exchange bias at collinear/noncollinear spin interface. *Sci. Rep.*, 3:1094, 2013.

[122] X.Z. Yu, N. Kanazawa, W.Z. Zhang, T. Nagai, T. Hara, K. Kimoto, Y. Matsui, Y. Onose, and Y. Tokura. Skyrmion flow near room temperature in an ultralow current density. *Nat. Commun.*, 3, 2012.

[123] T. Schulz, R. Ritz, A. Bauer, M. Halder, M. Wagner, C. Franz, C. Pfleiderer, K. Everschor, M. Garst, and A. Rosch. Emergent electrodynamics of skyrmions in a chiral magnet. *Nat. Phys.*, 8:301, 2012.

[124] A. Bogdanov and A. Hubert. Thermodynamically stable magnetic vortex states in magnetic crystals. *J. Magn. Magn. Mater.*, 138:255, 1994.

[125] U.K. Rößler, A.N. Bogdanov, and C. Pfleiderer. Spontaneous skyrmion ground states in magnetic metals. *Nature*, 442:797, 2006.

[126] S. Seki, X.Z. Yu, S. Ishiwata, and Y. Tokura. Observation of skyrmions in a multiferroic material. *Science*, 336:198, 2012.

[127] X.Z. Yu, M. Mostovoy, Y. Tokunaga, W. Zhang, K. Kimoto, Y. Matsui, Y. Kaneko, N. Nagaosa, and Y. Tokura. Magnetic stripes and skyrmions with helicity reversals. *PNAS*, 109:8856, 2012.

[128] P. Milde, D. Köhler, J. Seidel, L.M. Eng, A. Bauer, A. Chacon, J. Kindervater, S. Mühlbauer, C. Pfleiderer, S. Buhrandt, C. Schütte, and A. Rosch. Unwinding of a skyrmion lattice by magnetic monopoles. *Science*, 340:1076, 2013.

[129] I. Dzyaloshinsky. A thermodynamic theory of weak ferromagnetism of antiferromagnetics. *J. Phys. Chem. Solids*, 4:241, 1958.

[130] A. K. Nayak, M. Nicklas, C. Shekhar, and C. Felser. Kinetic arrest related to a first-order ferrimagnetic to antiferromagnetic transition in the Heusler compound Mn_2PtGa. *J. Appl. Phys.*, 113:17E308, 2013.

[131] S. Chadov, X.-L. Qi, J. Kübler, G.H. Fecher, C. Felser, and S.-C. Zhang. Tunable multifunctional topological insulators in ternary Heusler compounds. *Nature Materials*, 9:541, 2010.

[132] S. Ouardi, G.H. Fecher, C. Felser, and J. Kübler. Realization of Spin Gapless Semiconductors: The Heusler Compound Mn_2CoAl. *Phys. Rev. Lett*, 110:100401, 2013.

[133] T. Klimczuk, C.H. Wang, K. Gofryk, F. Ronning, J. Winterlik, G.H. Fecher, J.-C. Griveau, E. Colineau, C. Felser, J.D. Thompson, D.J. Safarik, and R.J. Cava. Superconductivity in the Heusler family of intermetallics. *Physical Review Letters*, 85:174505, 2012.

[134] P. Villars, K. Cenzual, J.L.C. Daams, H. Hulliger, T.B. Massalski, H. Okamoto, K. Osaki, A. Prince, M. Berndt, K. Branderburg, H. Putz, and S. Iwata. *Pauling File. Inorganic Materials Database and Design System. Binaries Edition.* ASM International, Materials Park (OH), 2002.

[135] T. Graf, C. Felser, and S.S.P. Parkin. Simple rules for the understanding of Heusler compounds. *Prog. Solid State Ch.*, 39(1):1, 2011.

[136] G.E. Bacon and J.S. Plant. Chemical ordering in Heusler alloys with the general formula A_2BC or ABC. *J. Phys. F: Metal Physics*, 11:524, 1971.

[137] H. Pauly, A. Weiss, and H. Witte. The crystal structure of the ternary intermetallic phases Li_2EX (E = Cu, Ag, Au; X = Al, Ga, In, Tl, Si, Ge, Sn, Pb, Sb, Bi). *Bd.*, 59:47, 1968.

[138] J. Winterlik, G.H. Fecher, B. Balke, T. Graf, V. Alijani, V. Ksenofontov, C.A. Jenkins, O. Meshcheriakova, C. Felser, G. Liu, S. Ueda, K. Kobayashi, T. Nakamura, and M. Wójcik. Electronic, magnetic, and structural properties of the ferrimagnet Mn_2CoSn. *Phys. Rev. B*, 83:174448, 2011.

[139] V. Alijani, O. Meshcheriakova, J. Winterlik, G. Kreiner, G.H. Fecher, and C. Felser. Increasing Curie temperature in tetragonal Mn_2RhSn Heusler compound through substitution of Rh by Co and Mn by Rh. *J. Appl. Phys.*, 113:063904, 2013.

[140] P. Souvik and G. Subhradip. Effects of chemical disorder on magnetism in inverse Heusler alloy Mn_2NiSn. *Solid State Physics: Proceedings of the 57th DAE Solid State Physics Symposium 2012*, page 1258, 2012.

[141] S. Skaftouros, K. Özdoğan, E. Şaşioğlu, and I. Galanakis. Search for spin gapless semiconductors: The case of inverse Heusler compounds. *Appl. Phys. Lett.*, 102:022402, 2013.

[142] S. Skaftouros, K. Özdoğan, E. Şaşioğlu, and I. Galanakis. Generalized Slater-Pauling rule for the inverse Heusler compounds. *Phys. Rev. B*, 87:024420, 2013.

[143] J. Kiss, S. Chadov, G.H. Fecher, and C. Felser. Disorder-induced cubic phase in Fe_2-based Heusler alloys. *Phys. Rev. B*, 87:224403, 2013.

[144] J.B. Godenough and A.L. Loeb. Theory of ionic ordering, crystal distortion, and magnetic exchange due to covalent forces in spinels. *Phys. Rev.*, 98:391, 1955.

[145] W. Moffitt and C.J. Ballhausen. Quantum theory. *Annu. Rev. Phys. Chem.*, 7:107, 1956.

[146] D.S. McClure. The distribution of transition metal cations in spinels. *J. Phys. Chem. Solids*, 3:311, 1957.

[147] J.D. Dunitz and L.E. Orgel. Electronic properties of transition metal oxides - ii. *J. Phys. Chem. Solids*, 3:318, 1957.

[148] P.J. Wojtowitz. Theoretical model for tetragonal-to-cubic phase transformations in transition metal spinels. *Phys. Rev.*, 116, 1959.

[149] H.A. Jahn and E. Teller. Stability of polyatomic molecules in degenerate electronic states. *Proc. R. Soc. Lond. A*, 161:220, 1937.

[150] S. Ackerbauer and M. Wedel. Max planck institute for chemical physics of solids. structure competence group. powder diffraction guide, December 2011.

[151] J. Rodríguez-Carvajal. *FULLPROF computer program.* LLB, Saclay, 2004. version 2.80.

[152] D. Jiles. *Magntism and magnetic materials.* Chapman & Hall, 1991.

[153] K. Ullakko, J.K. Huang, C. Kantner, R.C. OŠHandley, and V.V. Kokorin. Large magnetic-field-induced strains in Ni_2MnGa single crystals. *Appl. Phys. Lett.*, 69:1966, 1996.

[154] A. Sozinov, A.A. Likhachev, N. Lanska, and K. Ullakko. Giant magnetic-field-induced strain in NiMnGa seven-layered martensitic phase. *Appl. Phys. Lett.*, 80:1746, 2002.

[155] H. Ebert, D. Ködderitzsch, and J. Minár. Calculating condensed matter properties using the KKR-Green's function method - recent developments and applications. *Rep. Prog. Phys.*, 74(9):096501, 2011.

[156] S.H. Vosko, L. Wilk, and M. Nusair. Accurate spin-dependent electron liquid correlation energies for local spin density calculations: a critical analysis. *Can. J. Phys.*, 58:1200, 1980.

[157] M. Meinert, J.-M. Schmalhorst, and G. Reiss. Exchange interactions and Curie temperatures of Mn_2CoZ compounds. 23:116005, 2011.

[158] H.-B. Luo, Q.-M. Hu, C.-M. Li, B. Johansson, L. Vitos, and R. Yang. Magnetic properties and temperature-dependent half-metallicity of $Co_2Mn(Ga_{1-x}Z_x)$ (Z=Si, Ge, Sn) from first-principles calculation. *J. Phys.: Condenced Matter*, 25(15):156003, 2013.

[159] A.I. Liechtenstein, M.I. Katsnelson, V.P. Antropov, and V.A. Gubanov. Local spin density functional approach to the theory of exchange interactions in ferromagnetic metals and alloys. *J. Magn. Magn. Mater.*, 67:65, 1987.

[160] H. Ebert and S. Mankovsky. Anisotropic exchange coupling in diluted magnetic semiconductors: *Ab initio* spin-density functional theory. *Phys. Rev. B*, 79:045209, 2009.

[161] B. Balke. *Special Heusler Compounds for Spintronic Applications.* PhD thesis, Johannes Gutenberg Univeristy Mainz, 2007.

[162] J. Winterlik, S. Chadov, A. Gupta, V. Alijani, T. Gasi, K. Filsinger, B. Balke, G.H. Fecher, C.A. Jenkins, F. Casper, J. Kübler, D. Liu, L. Gao, S.S.P. Parkin, and C. Felser. Design scheme of new tetragonal Heusler compounds for spin-transfer torque applications and its experimental realization. *Advanced Materials*, 24:6283, 2012.

[163] A. Tari. *The specific heat of matter at low temperatures.* Imperial College Press, 2003.

[164] P. Debye. Zur Theorie der spezifischen Wämen. *Ann. Phys.*, 1912.

[165] C.L. Snow, C.R. Lee, Q. Shi, J. Boerio-Goates, and B.F. Woodfield. Size-dependence of the heat capacity and thermodynamic properties of hematite (α-Fe_2O_3). *J. Chem. Thermodyn.*, 42:1142, 2010.

[166] M. Falkowski, M. Reiffers, M. Zapotoková, A. Kowalczyk, T. Toliński, and E. Gažo. Heat Capacity Studies of $NdNi_4Si$ Compound. *Acta. Phys. Pol. A*, 115, 2009.

[167] C.D. Stanciu, F. Hansteen, A.V. Kimel, A. Kirilyuk, A. Tsukamoto, A. Itoh, and Th. Rasing. All-optical magnetic recording with circularly polarized light. *Phys. Rev. Lett.*, 99:047601, 2007.

[168] A. Bogdanov and A. Hubert. The stability of vortex-like structures in uniaxial ferromagnets. *J. Magn. Magn. Mater.*, 195(1):182, 1999.

[169] U K Rößler, A A Leonov, and A N Bogdanov. Chiral skyrmionic matter in non-centrosymmetric magnets. *Joint Eur. Mag. Symposia*, 303:012105, 2010.

[170] O. Meshcheriakova and S. Chadov and A.K. Nayak and U.K. Rößler and J. Kübler and G. André and A.A. Tsirlin and J. Kiss and S. Hausdorf and A. Kalache and W. Schnelle and M. Nicklas and C. Felser. Large non-collinearity and spin-reorientation in the novel Mn_2RhSn Heusler magnet. *Phys. Rev. Lett*, 113:087203, 2014.

[171] G.D. Liu, J.L. Chen, Z.H. Liu, X.F. Dai, and G.H. Wu. Martensitic transformation and shape memory effect in a ferromagnetic shape memory alloy: Mn_2NiGa. *Appl. Phys. Lett.*, 87:262504, 2005.

[172] T. Gasi, A.K. Nayak, J. Winterlik, V. Ksenofontov, P. Adler, M. Nicklas, and C. Felser. Exchange-spring like magnetic behavior of the tetragonal Heusler compound Mn_2FeGa as a candidate for spin-transfer torque. *Appl. Phys. Lett.*, 102:202402, 2013.

[173] G.D. Liu, X.F. Dai, H.Y. Liu, J.L. Chen, Y.X. Li, G. Xiao, and G.H. Wu. Mn_2CoZ (Z = Al, Ga, In, Si, Ge, Sn, Sb) compounds: Structural, electronic, and magnetic properties. *Phys. Rev. B*, 77:014424, 2008.

[174] E.I. Gladyshevskii, P.I. Krypyakevych, M.Y. Teslyuk, O.S. Zarechnyk, and Y.B. Kyz'ma. Crystal structures of some intermetallic compounds. *Sov. Phys. Crystallogr.*, 6:207, 1961.

[175] M. Pugacheva and A. Jezierski. Dependence of the magnetic moment on the local atomic order in Rh_2MnX Heusler alloys. *J. Magn. Magn. Mater.*, 151:202, 1995.

[176] E. Uhl. Magnetism of two new series of Heusler alloys: $(Rh_{1-x}Co_x)_2MnSn$ and $(Rh_{1-x}Ni_x)_2MnSn$. *J. Magn. Magn. Mater.*, 49:101, 1985.

[177] K.H.J. Buschow, P.G. van Engen, and R. Jongebreur. Magneto-optical properties of metallic ferromagnetic materials. *J. Magn. Magn. Mater.*, 38:1, 1983.

[178] S. Jha, H.M. Seyoum, G.M. Julian, R.A. Dunlap, A. Vasquez, J.G.M. da Cunha, and S.M.M. Ramos. Hyperfine fields at *sp* sites in the Heusler aloy Rb_2MnZ (Z=Ge,Sn,Pb). *Phys. Rev. B*, 32:3279, 1985.

[179] A.I. Kaplienko, B.N. Leonov, and V.V. Chekin. Investigation of the dynamics of a magnetic transition in Mn_2Sn. *Sov. Phys. Solid State*, 11:3030, 1970.

[180] F. Weitzer and P. Rogl. The Mn-Nd-Sn system (Manganese-Neodymium-Tin). *J. Phase Equilibria*, 14:676, 1993.

[181] E. Ikenaga, M. Kobata, H. Matsuda, T. Sugiyama, H. Daimon, and K. Kobayashi. Development of high lateral and wide angle resolved hard X-ray photoemission spectroscopy at BL47XU in SPring-8. *J. Electron. Spectrosc. Relat. Phenom.*, 190:180, 2014.

[182] S. Ueda, Y. Katsuya, M. Tanaka, H. Yoshikawa, Y. Yamashita, S. Ishimaru, Y. Matsushita, and K. Kobayashi. Present status of the NIMS Contract Beamline BL15XU at SPring-8. *AIP Conf. Proc.*, 1234:403, 2010.

[183] S. Ueda. Application of hard x-ray photoelectron spectroscopy to electronic structure measurements for various functional materials. *J. Electron. Spectrosc. Relat. Phenom.*, 190:235, 2013.

[184] S. Ouardi, C. Shekhar, G.H. Fecher, X. Kozina, G. Stryganyuk, C. Felser, S. Ueda, and K. Kobayashi. Electronic structure of Pt based topological Heusler compounds with $C1_b$ structure and ”zero band gap”. *Appl. Phys. Lett.*, 98:211901, 2011.

[185] S. Ouardi, G.H. Fecher, X. Kozina, G. Stryganyuk, B. Balke, C. Felser, E. Ikenaga, T. Sugiyama, N. Kawamura, M. Suzuki, and K. Kobayashi. Symmetry of valence states of Heusler compounds explored by linear dichroism in hard X-ray photoelectron spectroscopy. *Phys. Rev. Lett.*, 107:036402, 2011.

[186] S. Ouardi, G.H. Fecher, and C. Felser. Bulk electronic structure studied by hard X-ray photoelectron spectroscopy of the valence band: The case of intermetallic compounds. *J. Electron Specrosc. Relat. Phenom.*, 190:249, 2013.

[187] R. Hesse, T. Chassé, and R. Szargan. Peak shape analysis of core level photoelectron spectra using UNIFIT for WINDOWS. *Fresenius J. Anal. Chem.*, 365:48, 1999.

[188] G.H. Fecher and C. Felser. *Hard X-Ray Photoelectron Spectroscopy of New Materials for Spintronics*, chapter 11, page 243. Springer Verlag, Dordrecht Heidelberg New York London, 2013.

[189] Y.M. Yarmoshenko, M.I. Katsnelson, E.I. Shreder, E.Z. Kurmaev, A. Slebarski, S. Plogmann, T. Schlathölter, J. Braun, and M. Neumann. Observation of magnetic splitting in XPS MnL-spectra of Co_2MnSn and Pd_2MnSn Heusler alloys. *Eur. Phys. J. B*, 2(1):1, 1998.

[190] S. Ouardi, A. Gloskovskii, B. Balke, C.A. Jenkins, J. Barth, G.H. Fecher, C. Felser, M. Gorgoi, M. Mertin, F. Schäfers, E. Ikenaga, K. Yang, K. Kobayashi, T. Kubota, M. Oogane, and Y. Ando. Electronic properties of Co_2MnSi thin films studied by hard x-ray photoelectron spectroscopy. *J. Phys. D: Appl. Phys.*, 42:084011, 2009.

[191] S. Ouardi, G.H. Fecher, B. Balke, A. Beleanu, X. Kozina, G. Stryganyuk, C. Felser, W. Kloss, H. Schrader, F. Bernardi, J. Morais, E. Ikenaga, Y. Yamashita, S. Ueda, and K. Kobayashi. Electronic and crystallographic structure, hard x-ray photoemission, and mechanical and transport properties of the half-metallic Heusler compound Co_2MnGe. *Phys. Rev. B*, 84:155122, 2011.

[192] F. de Groot and A. Kotani. *Core level spectroscopy of solids.* CRC Press, 2008.

[193] J. Fujii and B.R. Salles and M. Sperl and S. Ueda and M. Kobata and K. Kobayashi and Y. Yamashita and P. Torelli and M. Utz and C.S. Fadley and A.X. Gray and J. Braun and H. Ebert and I. Di Marco and O. Eriksson and P. Thunström and G.H. Fecher and H. Stryhanyuk and E. Ikenaga abd J. Minár and C.H. Back and G. van der Laan and G. Panaccione. Identifying the electronic character and role of the Mn states in the valence band of (Ga, Mn) As. *Phys. Rev. Lett.*, 111:097201, 2013.

[194] H. Pandey and R.C. Budhani. Structural ordering driven anisotropic magnetoresistance, anomalous Hall resistance, and its topological overtones in full-Heusler Co_2MnSi thin films. *J. Appl. Phys.*, 113(20):203918, 2013.

[195] I.-M. Imort, P. Thomas, G. Reiss, and A. Thomas. Anomalous Hall effect in the Co-based Heusler compounds Co_2FeSi and Co_2FeAI. *J. Appl. Phys.*, 111(7):07D313, 2012.

[196] M.P. Raphael, B. Ravel, Q. Huang, M.A. Willard, S.F. Cheng, B.N. Das, R.M. Stroud, K.M. Bussmann, J.H. Claassen, and V.G. Harris. Presence of antisite disorder and its characterization in the predicted half-metal Co_2MnSi. *Phys. Rev. B*, 66:104429, 2002.

[197] U. Geiersbach, A. Bergmann, and K. Westerholt. Structural, magnetic and magnetotransport properties of thin films of the Heusler alloys Cu_2MnAl, Co_2MnSi, Co_2MnGe and Co_2MnSn. *J. Magn. Magn. Mater.*, 240:546, 2002.

[198] F. Bloch. Zum elektrischen widerstandsgesetz bei tiefen temperaturen. *Z. Phys.*, 59:208, 1930.

[199] E. Grüneisen. Die Abhängigkeit des elektrischen Widerstandes reiner Metalle von der Temperatur. *Ann. Phys.*, 408:530, 1933.

[200] C. Suürgers and G. Fischer and P. Winkel and H. v. Löhneysen. Large topological hall effect in the non-collinear phase of an antiferromagnet. *Nat. Commun.*, 5, 2014.

[201] A. Neubauer, C. Pfleiderer, B. Binz, A. Rosch, R. Ritz, P. G. Niklowitz, and P. Böni. Topological hall effect in the a phase of mnsi. *Phys. Rev. Lett.*, 102:186602, 2009.

[202] Yufan Li, N. Kanazawa, X. Z. Yu, A. Tsukazaki, M. Kawasaki, M. Ichikawa, X. F. Jin, F. Kagawa, and Y. Tokura. Robust formation of skyrmions and topological hall effect in epitaxial thin films of mnsi. *arXiv:1209.4480.*

[203] M. Stampanoni, A. Vaterlaus, M. Aeschlimann, and F. Meier. Magnetism of epitaxial bcc Iron on Ag(001) observed by Spin-Polarized Photoemission. *Phys. Rev. Lett.*, 59:2483, 1987.

[204] S.A. Gusev, A.A. Fraerman, D.B. Rozenstein, and M.G. Teitelman. Thermally induced reversible spin reorientation transition in Co/Pd multilayers. *Phys. Lett. A*, 198:437, 1995.

[205] X. Hu and Y. Kawazoe. Surface anisotropy and spin-reorientation transitions in ultrathin magnetic films. *IEEE Trans. Magn.*, 32:4561, 1996.

[206] M. Farle. Ferromagnetic resonance of ultrathin metallic layers. *Reports in Progress in Physics*, 61:755, 1998.

[207] B. Heinrich and J.A.C. Bland, editors. *Ultrathin Magnetic Structures II.* Springer-Verlag Berlin Heidelberg, 1994.

[208] B. Schulz and K. Baberschke. Crossover from in-plane to perpendicular magnetization in ultrathin Ni/Cu(001) films. *Phys. Rev. B*, 50:13467, 1994.

[209] B. Heinrich, J.F. Cochran, A.S. Arrott, S.T. Purcell, K.B. Urquhart, J.R. Dutcher, and W.F. Egeihoff. Development of magnetic anisotropies in ultrathin epitaxial films of Fe(001) and Ni(001). *Appl. Phys. A*, 49:473, 1989.

[210] C. Kittel. On the theory of ferromagnetic resonance absorption. *Phys. Rev.*, 73:155, 1948.

[211] A.K. Srivastava, M.J. Hurben, M.A. Wittenauer, P. Kabos, C.E. Patton, R. Ramesh, P.C. Dorsey, and D.B. Chrisey. Angle dependence of the ferromagnetic resonance linewidth and two magnon losses in pulsed laser deposited films of yttrium iron garnet, MnZn ferrite, and NiZn ferrite. *J. Appl. Phys.*, 85:7838, 1999.

[212] D.L. Mills and S.M. Rezende. Spin damping in ultrathin magnetic films. In *Spin Dynamics in Confined Magnetic Structures II*, volume 87 of *Topics in Applied Physics*, page 27. Springer Berlin Heidelberg, 2003.

[213] S. Mizukami, Y. Ando, and T. Miyazaki. Effect of spin diffusion on Gilbert damping for a very thin permalloy layer in Cu/permalloy/Cu/Pt films. *Phys. Rev. B*, 66:104413, 2002.

[214] M.T. Johnson, P.J.H. Bloemen, F.J.A. den Broeder, and J.J. de Vries. Magnetic anisotropy in metallic multilayers. *Rep. Prog. Phys.*, 59:1409, 1996.

[215] I. Neudecker, G. Woltersdorf, B. Heinrich, T. Okuno, G. Gubbiotti, and C.H. Back. Comparison of frequency, field, and time domain ferromagnetic resonance methods. *J. Magn. Magn. Mater.*, 307:148, 2006.

[216] S.S. Kalarickal, P. Krivosik, M. Wu, C.E. Patton, M.L. Schneider, P. Kabos, T.J. Silva, and J.P. Nibarger. Ferromagnetic resonance linewidth in metallic thin films: Comparison of measurement methods. *J. Appl. Phys.*, 99:093909, 2006.

[217] T.L. Gilbert. A phenomenological theory of damping in ferromagnetic materials. *IEEE Transactions on Magnetics*, 40:3443, 2004.

[218] C. Bilder, T. Devolder, P. Crozat, C. Chappert, S. Cardoso, and P.P. Freitas. Vector network analyzer ferromagnetic resonance of thin films on coplanar waveguides: Comparison of different evaluation methods. *J. Appl. Phys.*, 101:074505, 2007.

[219] S. Trudel, O. Gaier, J. Hamrle, and B. Hillerbrands. Magnetic anisotropy, exchange and damping in cobalt-based full-Heusler compounds: an experimental review. *J. Phys. D*, 43:193001, 2010.

[220] C.E. Patton. *Dynamic processes in magnetic thin films. Domain wall motion and ferromagntic resonance.* PhD thesis, California Institute of Technology, 1967.

List of Figures

List of Tables